

# Dissertation

## Antenna design for future multi-standard and multi-frequency RFID systems

ausgeführt zum Zwecke der Erlangung des akademischen Grades eines  
Doktors der technischen Wissenschaften unter der Leitung von

Ao.Univ.Prof. Univ.Prof. Dipl.-Ing. Dr.techn. Arpad L. Scholtz  
Technische Universität Wien  
Institut für Nachrichtentechnik und Hochfrequenztechnik (E389)

zweiter Begutachter

Prof. Dr.-Ing. Dr.-Ing. habil. Robert Weigel  
Friedrich-Alexander-Universität Erlangen-Nürnberg  
Lehrstuhl für Technische Elektronik

eingereicht an der

Technischen Universität Wien  
Fakultät für Elektrotechnik und Informationstechnik

von

**Lukas W. Mayer, 9927042**  
Hahngasse 12/17  
1090 Wien

Wien, Juni 2009

---



# Abstract

In this work I investigate radio propagation and antennas used in radio frequency identification (RFID) systems operating in the high frequency (HF) band at 13.56 MHz and in the ultra-high frequency (UHF) band between 860 MHz and 960 MHz. Where at 13.56 MHz, the transmission between an interrogator (or reader) and a transponder (or tag) are well known and can be determined analytically, modeling of the radio transmission in the UHF band is a far more challenging task. Instead of modeling the UHF channel, I decided to pursue a rather empirical approach by performing and discussing measurements in RFID typical environments. The results show that the region where transponders are reliably recognized might be quite small. However, with some modifications to the scenario and with appropriate choice and placement of reader and tag antennas, it is shown how reliability can be significantly improved.

In a further chapter I focus on the interaction between a transponder antenna and a transponder chip at UHF. In particular, the mechanism of backscattering that is utilized to achieve a data transmission from the transponder to the interrogator (the return-link) is theoretically analyzed. It is found that for a given transponder chip, there exists two distinct optimum antenna impedances, one maximizes the power available for the chip's internal circuitry and one maximizes the signal that is reradiated towards the interrogator. To draw conclusions for the link budget of an RFID system, a numerical example is presented that relies on measured characteristics of state-of-the-art transponder chips. This new measurement method for thoroughly characterizing the input impedances and the sensitivity of transponder chips is also presented in this work.

For exploiting the benefits of both the HF and the UHF band, a dual-band transponder antenna was designed. The antenna consists of a shorted loop-slot antenna serving the UHF band and a printed spiral operating as an air coil in the HF band. Both structures were merged into one single-input dual-band antenna. Therefore, the UHF antenna structure was modified to additionally function as two turns of the HF coil. With this arrangement the performance at HF remains at the level of single-band antenna solutions. To determine the characteristics at UHF, a new and highly accurate measurement method was developed to characterize both input impedance and gain of electrically-small and autonomous antennas. By comparing

the dual-band antenna with a manufactured single-band antenna occupying the same amount of area, it was shown by measurement that the performance of the dual-band design at UHF is only impaired by some few decibel.

In return-link limited UHF RFID systems, the read range is determined by the capability of the interrogator's radio frequency (RF) frontend to separate the strong transmitted signal leaking into the receiver from the weak backscattered signal reradiated by the transponder. To avoid costly carrier compensation circuitry in the RF frontend, I designed a microstrip patch antenna that uses a tunable directional coupler to provide high transmit to receive separation. By continuously tuning this coupler, a separation of more than 52 dB was achieved in time variant scenarios.

# Contents

<b>1</b>	<b>Introduction</b>	<b>1</b>
1.1	Primarily deployed RFID systems today . . . . .	1
1.2	Magnetic coupling in HF RFID systems . . . . .	3
1.2.1	Antennas for HF systems . . . . .	3
1.3	Radio transmission in UHF RFID systems . . . . .	7
1.3.1	Measurements of UHF RFID channels . . . . .	10
1.3.2	Reciprocity . . . . .	14
1.3.3	Antennas for UHF RFID systems . . . . .	16
1.4	Radio transmission at UHF versus inductive coupling at HF . . . . .	18
<b>2</b>	<b>Antenna / chip interaction</b>	<b>21</b>
2.1	Matching antenna and chip impedances . . . . .	21
2.2	Scattering properties of antennas . . . . .	22
2.3	Backscatter modulation . . . . .	24
2.4	Effects on a system shown with a numerical example . . . . .	31
2.4.1	Link budget . . . . .	33
2.4.2	Forward link . . . . .	35
2.4.3	Return link . . . . .	37
2.5	Consequences for an RFID system . . . . .	37
<b>3</b>	<b>A dual-band HF / UHF transponder antenna for RFID tags</b>	<b>39</b>
3.1	Dual-band transponder antenna requirements . . . . .	40
3.1.1	Electrical definition . . . . .	40
3.1.2	Environmental definition . . . . .	42
3.2	Antenna design . . . . .	44
3.2.1	HF antenna . . . . .	44
3.2.2	UHF antenna . . . . .	45
3.2.3	Combining the antennas . . . . .	45
3.2.4	Antenna tuning . . . . .	48
3.2.5	Dual-band antenna with HF coil on the inside . . . . .	49
3.3	Antenna simulation . . . . .	50
3.3.1	Full model . . . . .	51
3.3.2	Simplified planar model . . . . .	51
3.4	Measurements . . . . .	53

3.4.1	HF measurements . . . . .	53
3.4.2	UHF impedance measurements . . . . .	54
3.4.3	UHF gain measurements . . . . .	56
3.5	Summary . . . . .	65
<b>4</b>	<b>An interrogator antenna with high transmit to receive separation</b>	<b>67</b>
4.1	Motivation . . . . .	67
4.2	Antenna principle . . . . .	69
4.3	Tunable hybrid . . . . .	70
4.3.1	Simulation . . . . .	70
4.3.2	Measurement . . . . .	75
4.4	Square patch antenna . . . . .	76
4.4.1	Simulation . . . . .	78
4.5	Automatic tuning hardware . . . . .	79
4.6	Performance testing . . . . .	79
4.7	Considerations for automatic tuning . . . . .	82
4.8	Summary . . . . .	84
<b>5</b>	<b>Gain and impedance measurement method for transponder antennas</b>	<b>85</b>
5.1	Motivation . . . . .	85
5.2	Directional pattern and antenna efficiency measurement . . . . .	87
5.3	Rotation unit . . . . .	88
5.4	Small battery driven oscillator . . . . .	89
5.5	Antenna impedance measurement . . . . .	92
5.6	Test measurement . . . . .	94
5.7	Summary . . . . .	97
<b>6</b>	<b>Impedance measurement method for transponder chips</b>	<b>99</b>
6.1	Motivation . . . . .	99
6.2	Chip test setup . . . . .	101
6.3	Chip test fixture . . . . .	102
6.4	Wake-up sequence . . . . .	105
6.5	Impedance measurement . . . . .	107
6.6	Power sweep . . . . .	108
6.7	Efficiency of backscattering . . . . .	109
6.8	Comparison of the results with manufacturer's data sheets . . . . .	112
6.9	Parameter sweeps . . . . .	113
6.10	Summary . . . . .	114
<b>7</b>	<b>Conclusion</b>	<b>115</b>

# 1 Introduction

This work relates to practical antennas for the economically most relevant radio frequency identification systems that are in use or under development today. RFID is a method that allows to remotely retrieve, store, and manipulate data contained in a transponder unit that is permanently attached to an object. This introduction focuses on these systems and explains their mode of operation as well as the physical basics that can be exploited to achieve energy and data transmission between an interrogating device (or reader) and a passive transponder (or tag). Antenna requirements for RFID systems are rendered and today's most frequently used antenna solutions are explained. To obtain the characteristics of the radio channel, some results of a measurement campaign that was conducted with RFID typical antennas in prevalent scenarios are presented. The chapter concludes with a comparison of two systems, one of them utilizes magnetic coupling at 13.56 MHz and the other one uses radio transmission in a frequency band between 860 MHz and 960 MHz.

## Original publications related to this chapter

L. W. Mayer, M. Wrulich, and S. Caban, "Measurements and channel modelling for short range indoor UHF applications," in *Proc. The First European Conference on Antennas and Propagation*, (Nice, France), Oct. 2006.

L. W. Mayer and A. L. Scholtz, "Antennas and radio transmission in RFID systems." Talk: EEEfCOM - Workshop, Ulm, Germany, May 2008.

L. W. Mayer and A. L. Scholtz, "Antennen und Freiraumausbreitung für UHF RFID Systeme." Talk: Tutorial on "Radio Frequency Identification Systems (RFID)", Forschungszentrum Telekommunikation Wien, Austria, Oct. 2007.

## 1.1 Primarily deployed RFID systems today

Object identification for managing a supply chain is probably the most relevant field for RFID technology. This task requires cheap, compact, reliable, and often

long-lasting transponder units that contain a non-volatile random access memory for storing and updating data. Storing data directly with the object saves costs and allows to quickly process or pass on the object without the need for an inquiry at a remote database in real-time. Low-cost transponder units are passive, which means that they do not have a dedicated power source, but draw the energy needed for operation from the electromagnetic field that is produced by an interrogating device.

In recent years, two system concepts have evolved that utilize the electromagnetic field for data and energy transmission between the transponders and the interrogators. Apart from an affinity in the principle operation these two systems operate at very different carrier frequencies and thus require separate consideration, especially concerning the antennas and RF<sup>1</sup> frontends. These systems are

- RFID systems that operate in the HF<sup>2</sup> band at 13.56 MHz and
- RFID systems that operate in the UHF<sup>3</sup> band between 860 MHz and 960 MHz.

Both systems are available at a quite advanced stage today. Some different standards treating the air interface have been released for HF [1, 2] and UHF [3, 4]. The latter have very recently been consolidated and published by the ISO<sup>4</sup> as “Amendment 1” to the existing ISO18000-6 standard [5]. However, there is great potential in optimizing the functionality and reliability of RFID systems beyond the standardized—especially in the UHF domain. Many techniques like beam-forming, active carrier cancelation, advanced RF frontend designs, and extensive use of digital signal processing hardware to manage e.g. collisions of multiple transponders are not yet provided by most commercially available RFID systems. In 2004, Infineon Technologies Austria AG started the research project *Comprehensive Transponder System* (CTS) to determine whether a system can be set up that is able to switch between the HF and the UHF band, thus exploiting the benefits of both frequency bands.

In the CTS project I was assigned to investigate the radio transmission in both the HF and the UHF band and to do research on practical antennas that enable dual-band operation. At the interrogator side a dual-band antenna design was not considered because separate HF and UHF antennas can be used. Designing dual-band antennas for RFID transponders on the other hand is very challenging. The characteristics of the transponder antenna have a direct impact on the system performance that can hardly be regained by relaxing other system constraints. The transponder antenna thus has to compete with the performance of

---

<sup>1</sup>RF: radio frequency

<sup>2</sup>The high frequency (HF) band ranges from 3 MHz to 30 MHz.

<sup>3</sup>The ultra-high frequency (UHF) band ranges from 300 MHz to 3 GHz.

<sup>4</sup>ISO: International Organization for Standardization

single band variants and is subject to the same tight constraints regarding size and costs.

## 1.2 Magnetic coupling in HF RFID systems

At 13.56 MHz, magnetic coupling is used to transfer energy between two coils, one is the interrogator coil and one is the transponder coil. The interrogator coil is loaded with an alternating current and produces a dominantly magnetic field. The transponder coil that is pervaded by this field produces an induced voltage at its output. Figure 1.1 shows the principle of the transformer-like coupling between the two windings. The magnetic field around the interrogator coil can be calculated by adding the contributions of a segmented version of the current carrying conductors [6, 7] and it can be shown that the field strength  $H$  decays inversely proportional with the distance  $r$  from the coil taken to the power of three ( $|H| \sim 1/r^3$ ).

This loosely-coupled transformer-like arrangement can be used to transfer energy from the interrogator to the transponder. The power transmission loss between the interrogator coil input and the transponder coil output is related to the mutual inductance [8, 9, 10, 11] and decays with the transmission distance to the power of six ( $P_{\text{Tag}} \sim 1/r^6$ ). This shows that a long read range can not be achieved with two electrically-small coils at a frequency of 13.56 MHz.

As a representative example the power transmission coefficient

$$|h_{\text{HF}}|^2 = P_{\text{RX,Tag}}/P_{\text{TX,Reader}} \quad (1.1)$$

between two circular windings that are aligned coaxially in free space is given by Equation 1.2 [12]. A description of the symbols is given in Table 1.1. In Section 1.4 a plot of an exemplary HF transmission coefficient versus distance will be shown (Figure 1.6).

$$|h_{\text{HF}}|^2 = \frac{1}{4R_1R_2} \frac{(\mu_0\omega\pi N_1N_2a^2b^2)^2}{(r^2 + a^2)^3} \quad (1.2)$$

### 1.2.1 Antennas for HF systems

For low-cost applications in the HF band, wound and printed coils are used at the interrogator and the transponder, respectively. Since there is almost no power radiated because the coils are very small compared to the free space wavelength, the power transmission loss mainly depends on the characteristics of the windings and their position and orientation in space [8, 13].

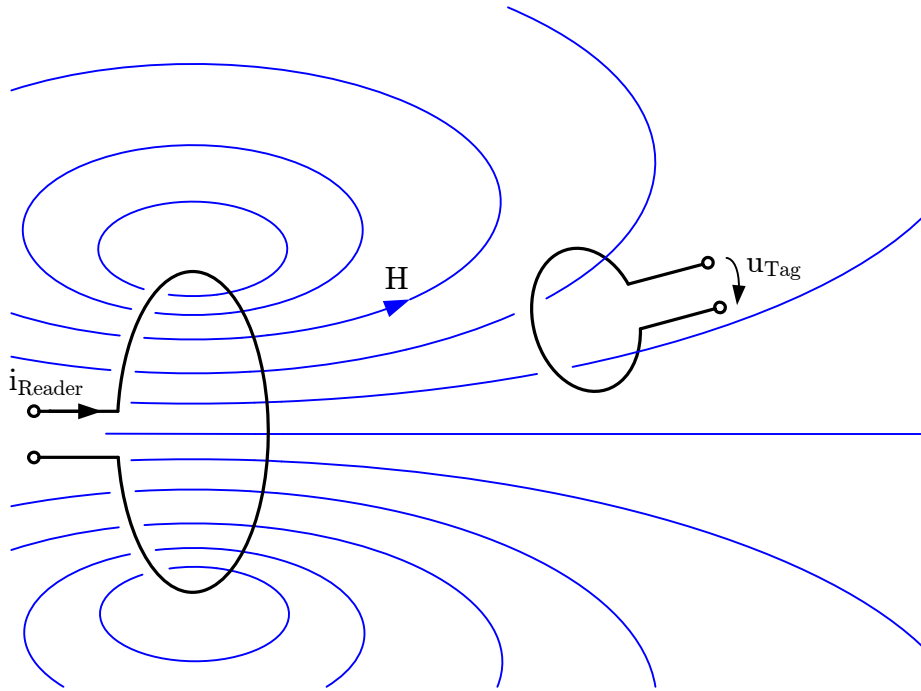


Figure 1.1: Principle of coupling between reader and tag at 13.56 MHz.

### HF interrogator coils

To power a transponder the interrogator coil has to provide a minimum required magnetic field strength  $H_{\text{Min}}$  at the transponder's position. Practical and efficient interrogator coils achieve that with a minimum number of turns  $N$  that conduct a minimum current  $I$ . When optimizing the coil radius  $a$  of a circular coil that provides  $H_{\text{Min}}$  at the transponder's position with respect to a minimum number of ampere-turns  $NI$ , an optimum coil radius can be determined. According to [12], the optimum coil radius  $a_{\text{Opt}}$  that requires the minimum number of ampere-turns for a particular read range  $r$  is  $a_{\text{Opt}} = \sqrt{2} \cdot r$ . The read range of an HF system is thus closely related to the size of the interrogator antenna. Coils with a radius smaller than  $a_{\text{Opt}}$  will either require more turns, or more current. Both measures lead to higher losses in the coil and—more importantly—to a higher magnetic field strength in the coil center. This relation implicates that the compact long-range reader for an HF RFID system is not feasible—at least not when the limits for the emitted magnetic field strength enacted by local authorities have to be met.

Efficient interrogator coils usually consist of a wire or a band made from a well conducting material like copper or silvered metal. Depending on the application the coil might fit in a hand-held reader device, surround a conveyor belt, or might

Table 1.1: List of symbols for Equation 1.2.

symbol	description	value (Figure 1.6)
$ h_{\text{HF}} ^2$	magnitude of power transmission coefficient	
$R_1$	loss resistance of reader antenna	$2 \Omega$
$R_2$	input resistance of tag chip	$10 \text{ k}\Omega$
$\mu_0$	permittivity constant	$4\pi 10^{-7} \text{ Vs/Am}$
$\omega$	angular frequency $\omega = 2\pi f$	$2\pi \cdot 13.56 \text{ MHz}$
$N_1$	number of turns at the reader antenna	10 Turns
$N_2$	number of turns at the tag antenna	5 Turns
$a$	radius of the reader antenna	0.2 m
$b$	radius of the tag antenna	25 mm
$r$	transmission distance	

frame a whole gate. To achieve an increase of the magnetic field strength, the reader coil is connected to a high-quality capacitor to form a parallel resonant circuit. When brought to resonance at 13.56 MHz, a current step-up in the coil that can be expressed by the quality factor  $Q$ , is obtained. The  $Q$ -factor of a circuit is defined as the ratio between its center frequency and bandwidth. With a high  $Q$ -factor the parallel resonant circuit will show an undesired bandpass filter characteristic which damps the response received from transponders. It is thus important to take control of the  $Q$ -factor. Typically, a  $Q$ -factor of 10 to 30 is chosen for interrogator antennas which offers a good trade-off between current step-up and frequency response [14].

### HF transponder coils

Printed or wound spiral coils are commonly used as transponder antennas in the HF band. Most transponder coils consist of a metallization on plastic or paper. There are also coil variants that feature a wire that is molded into plastic or glued onto an adhesive film.

The alternating magnetic field produced by the interrogator penetrates the transponder spiral. The fraction of the magnetic field that is aligned perpendicular to the spiral plane induces a voltage in the winding. The voltage observed at the coil output strongly depends on the alignment of the two antenna windings with respect to each other. If the magnetic field is in parallel to the spiral plane no voltage is observed at the coil output. Often, additional interrogator coils that produce orthogonal fields are deployed in HF systems to gain independence from transponder orientation. With a time domain multiplexing scheme each coil can then be used separately to detect transponders.

According to the law of induction the open-circuit voltage of the transponder coil can be increased by the following:

**Magnetic field increase** Exposing the transponder to a stronger magnetic field which can be achieved by more transmit power at the transmitter. This method is limited by the maximum field strength allowed by the authorities and might depend on the global region.

**Distance decrease** Reducing the distance between the coils which increases the coupling factor is basically not an option because the read range is defined by the application.

**Coil diameter increase** Enlarging the diameter of the windings in order to collect more magnetic flux is possible but limited to the maximum allowed size of the transponder.

**Number of turns increase** A higher number of turns is the most effective way of increasing the open-circuit voltage of a coil. Each additional turn of the winding contributes its amount of voltage to the output. However, in planar spiral-shaped antenna coils the contribution of the inner coil turns is smaller because they cover a smaller area and thus collect less magnetic flux. Also, when the coil is loaded with the chip impedance, additional turns cause losses in the antenna that are related to the total resistance of the spiral conductor. It is obvious that when the antenna dimensions are fixed and the number of turns is increased, the conductor width of the winding has to be smaller. This causes dissipative losses and decreases the amount of available power at the antenna terminals. The most efficient antenna can be found by optimizing the number of turns and the width of the conductor, given fixed dimensions.

The optimization criterion for the antenna in the HF domain is to deliver maximum voltage to the transponder chip input. The internal rectifier of the chip then converts the 13.56 MHz signal into the supply voltage that powers the chip's digital circuits. At HF, the input resistance of such a rectifier is typically some  $10\text{ k}\Omega$ , and the input capacitance is very low. For maximum chip input voltage it is advantageous to create a parallel resonant circuit that consists of the transponder coil, the input impedance of the chip's rectifier and an additional capacitance that tunes the resonant frequency to 13.56 MHz. The voltage step-up of this circuit allows to significantly improve the read range of HF transponders. In modern transponders the capacitance is built into the transponder chip. The capacitor in conjunction

with the coil defines the resonant frequency of the circuit. The equivalent parallel loss resistance and thus the bandwidth is determined by the quality of the on-chip capacitor, the ohmic losses in the coil, and the input impedance of the rectifier. In principle,  $Q$ -factors of more than 100 could be realized with state-of-the-art technology. On the one hand this leads to a good voltage step-up and consequently high sensitivity of the transponder, but on the other hand a very narrow-band resonant circuit is created. For most applications this is not desired because such transponders are very prone to detuning effects when put close to conducting or ferromagnetic materials [15]. More robust transponders are achieved by optimizing the inductance and resistance of the coil to achieve a wide-band voltage step-up. A typical  $Q$ -factor that is desired for RFID tag antennas is about 40. This leads to a bandwidth of 340 kHz. It is also common practice to start a tag antenna design with a higher-than-needed efficiency and resonant frequency, expecting it to be lowered when the antenna is operated in its environment. Also, if multiple transponders are placed close to each other a reduction of center frequency can be expected.

## 1.3 Radio transmission in UHF RFID systems

Unlike at 13.56 MHz where RFID tag antennas are tiny compared to the free space wavelength ( $\lambda_{13.56\text{ MHz}} = 22.1\text{ m}$ ), it is possible to use antennas that are comparable in size with the free space wavelength at 866 MHz ( $\lambda_{866\text{ MHz}} = 346\text{ mm}$ ).

Heinrich Hertz used Maxwells equations to calculate the field produced by an infinitesimal dipole—the Hertzian dipole—in free space and found that there exist one electric and one magnetic field component that decreases inversely proportional with the distance from the antenna [16]. These field components are called the far field of an antenna and can overcome large distances. Equation 1.3 can be used to calculate the electric and the magnetic field vectors that are produced by a Hertzian dipole in free space. The formulas relate to a spherical coordinate system where a point  $P$  is identified by a polar angle  $\vartheta$ , an azimuth angle  $\varphi$  and a radial distance  $r$  (Figure 1.2). The field terms assigned to the reactive near field of the dipole that decrease faster than the far field terms are written in gray. A description of the symbols is found in Table 1.2.

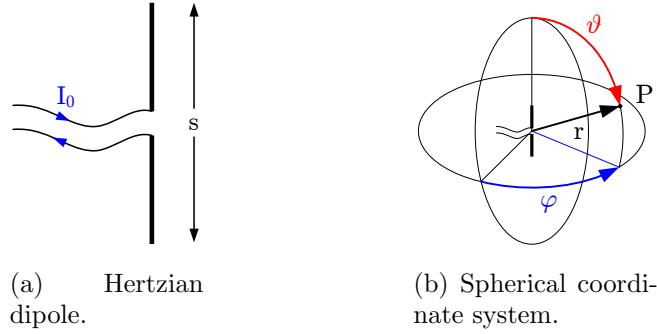


Figure 1.2: Hertzian dipole and its orientation in a spherical coordinate system.

$$\begin{aligned}
 E_{\vartheta} &= \frac{I_0 s \sin(\vartheta)}{4\pi\epsilon_0\omega} \left( \frac{-j}{r^3} + \frac{k}{r^2} + \frac{jk^2}{r} \right) e^{j(\omega t - kr)} \\
 E_r &= \frac{I_0 s \cos(\vartheta)}{2\pi\epsilon_0\omega} \left( \frac{-j}{r^3} + \frac{k}{r^2} \right) e^{j(\omega t - kr)} \\
 H_{\varphi} &= \frac{I_0 s \sin(\vartheta)}{4\pi} \left( \frac{1}{r^2} + \frac{jk}{r} \right) e^{j(\omega t - kr)}
 \end{aligned} \tag{1.3}$$

Table 1.2: List of symbols for Equation 1.3.

symbol	description
$I_0$	amplitude of the electrical current along dipole
$s$	dipole length ( $s \ll \lambda_0$ )
$\lambda_0$	free space wavelength
$r$	transmission distance (radial)
$\vartheta$	polar angle of the spherical coordinate system (Figure 1.2)
$k$	free space wave number ( $k = \frac{2\pi}{\lambda_0}$ )
$\omega$	angular frequency ( $\omega = 2\pi f$ )
$t$	time
$\epsilon_0$	dielectric constant of free space
$j$	$\sqrt{-1}$

Figure 1.3 sketches a radio transmission between a reader and a tag antenna. The power that is fed into the reader antenna input  $P_{\text{TX,Reader}}$  is radiated into space according to the directional pattern of the reader antenna. The gain of commercially available reader antennas is typically some 5 dBi<sup>5</sup> to 12 dBi. The transponder antenna picks up some power that comes directly from the reader antenna (commonly

<sup>5</sup>dBi denotes the antenna gain with respect to the isotropic radiator.

referred to as line-of-sight component) as well as signals that have been reflected at objects (multipath components). Weighted by the gain pattern of the transponder antenna, these components are then available at the transponder antenna port. Since low-cost RFID tags are small compared to the free space wavelength they have low gain and efficiency [17]. A gain below 0 dBi is typical for transponder antennas. With multipath components being present, the power available at the transponder antenna port  $P_{RX,Tag}$  also depends on the properties of the environment in which the antennas are operated. The power transmission coefficient  $|h|^2 = P_{RX,Tag}/P_{TX,Reader}$  thus depends on the

- transmission distance, the
- properties of the environment in which the antennas are operated in, the
- position and alignment of the antennas within the environment, and the
- gain patterns of the antennas.

The power transmission coefficient  $|h|^2$  contains a large number of parameters of the scenario and, in most cases, can not be analytically determined. However, for indoor radio transmission  $|h|$  can be described with stochastic models [18, 19]. These models are designed to render the effects of multipath propagation that occur in indoor transmission scenarios. They consider propagation in the far field of transmit and receive antennas. Since RFID transponders are often positioned in the transition region between near field and far field of the interrogator antenna, such models are inadequate. Furthermore, measurements have shown that because of the small transmission distance in RFID applications, only a few rather unpredictable multipath components are present [20]. In contrast to mobile communications where a large number of multipath components allows quite accurate statistical modeling, prediction of RFID channels is much more difficult. Usually, the antennas

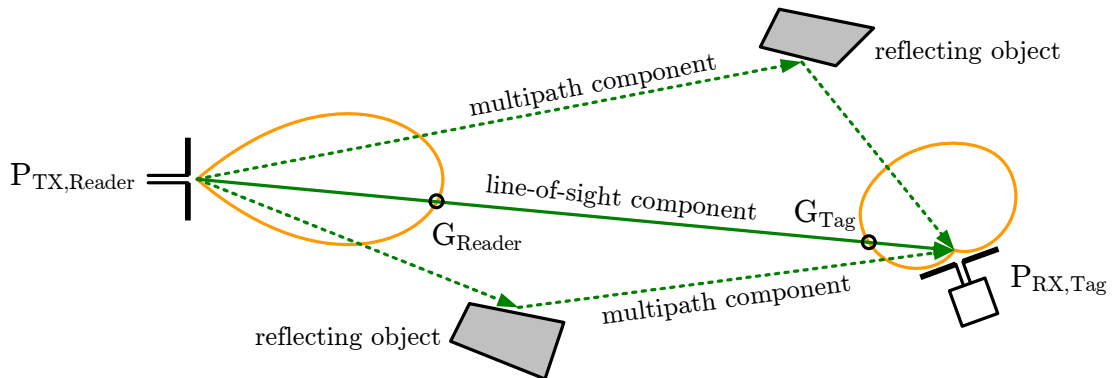


Figure 1.3: Schematic of a radio transmission between reader and tag antenna.

and radio components for a specific RFID application have to be optimized by conducting experiments on-site.

### 1.3.1 Measurements of UHF RFID channels

In this section two exemplary measurements of RFID channels conducted in a laboratory and in a metal machining workshop are presented and discussed. The transmission coefficient between a fixed reader antenna and a flexible low-profile transponder antenna is determined while the transponder antenna is moving in space.

#### Antennas

A microstrip patch antenna with a resonant frequency of 868 MHz and a measured gain of 7.1 dBi was chosen for the reader antenna. The half-power beamwidth of this antenna is  $70^\circ$ . The reader antenna radiates vertically polarized waves. A shorted loop-slot antenna was used as a tag antenna. It can be fed by a coaxial wire and is vertically polarized as well. The measured gain of the tag antenna is 0.5 dBi.

Since both antennas are low-profile, a minimum distance of 5 cm was chosen for the measurement which means that the antennas were placed within the near field of each other. Thus, direct capacitive and inductive coupling effects between the antennas as well as the radio transmission loss at higher distance are obtained. For the measurement both linearly polarized antennas were aligned to achieve the best transmission.

#### Measurement results

A series of measurements was carried out in four different indoor scenarios. The results and a detailed discussion of the entire measurement campaign can be found in [20]. In this work, two representative samples were chosen to illustrate the wave propagation for RFID. The first measurement site was a  $14 \times 8 \text{ m}^2$  room with heavy metal machining equipment. I will refer to this room as the *metal machining workshop*. The second environment presented is a  $8 \times 6 \text{ m}^2$  office with four workplaces and some laboratory equipment referred to as *laboratory area*.

Common for both measurement setups, a transmission coefficient of approximately  $-10 \text{ dB}$  is measured at an antenna distance of  $d = 5 \text{ cm}$ . Here, direct inductive and capacitive coupling effects between the antennas are observed. When the antennas

are moved apart, the transmission coefficient decreases rapidly. At a distance of approximately 40 cm ( $\approx \lambda_0$ ) the steep decrease ends and turns into a more temperate decay. At this point, the transmission coefficient has dropped to approximately -25 dB.

Since the measurements were carried out indoors, signal components that result from reflections at objects and walls are received by the tag antenna as well. Close to the transmit antenna, the direct signal component dominates. Other signals are weaker because of reflection losses at interacting objects and increased path lengths. Further away from the antenna the direct component decays and consequently the superposition with reflected signals leads to standing waves in space. Particularly, this happens if the amplitude of the direct signal and the superposed reflected signals are in the same order of magnitude. The measurements show that the mean signal strength of the reflected signal components in the area far off the transmit antenna ( $d > 2$  m) is fairly constant versus transmission distance. The mean signal strength of the reflected components depends primarily on the properties of the scenario.

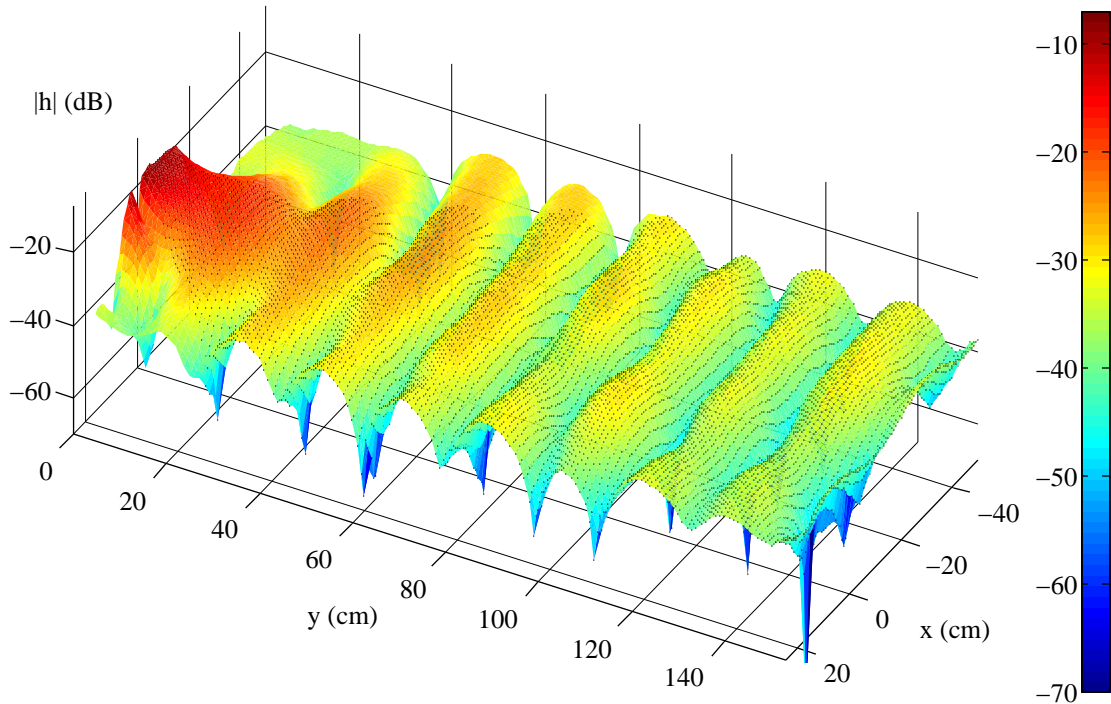


Figure 1.4: Transmission coefficient versus receive antenna position in the metal machining workshop. The transmit antenna is located at the origin (0,0) and aims at positive y-direction. Measurements within the half-power beamwidth cone of the transmit antenna are marked with dots.

**Metal machining workshop** Figure 1.4 shows the transmission coefficient measured in the metal machining workshop. In this figure, the origin (0,0) represents the position of the transmit antenna that was aimed at positive y-direction. Samples inside the half-power beamwidth cone of the transmit antenna are marked with dots to illustrate the reasonable area of operation. The area in front of the antenna is covered well but shows a steep decrease of the transmission coefficient versus distance. At a distance of 1 m and more, deep fading makes the channel loss hard to predict and thus influences the reliability of energy and data transfer necessary for communication with an RFID tag. Areas not directly irradiated by the transmit antenna show deep fades of more than 40 dB. In further measurements also performed in the metal machining workshop, deep fades start to occur from 25 cm transmission distance on. This clarifies that in such an environment special care has to be taken when choosing and positioning the transmit antenna. RFID tags that are placed outside the half-power beamwidth cone of the transmit antenna will not be recognized reliably—even when placed close to the transmit antenna.

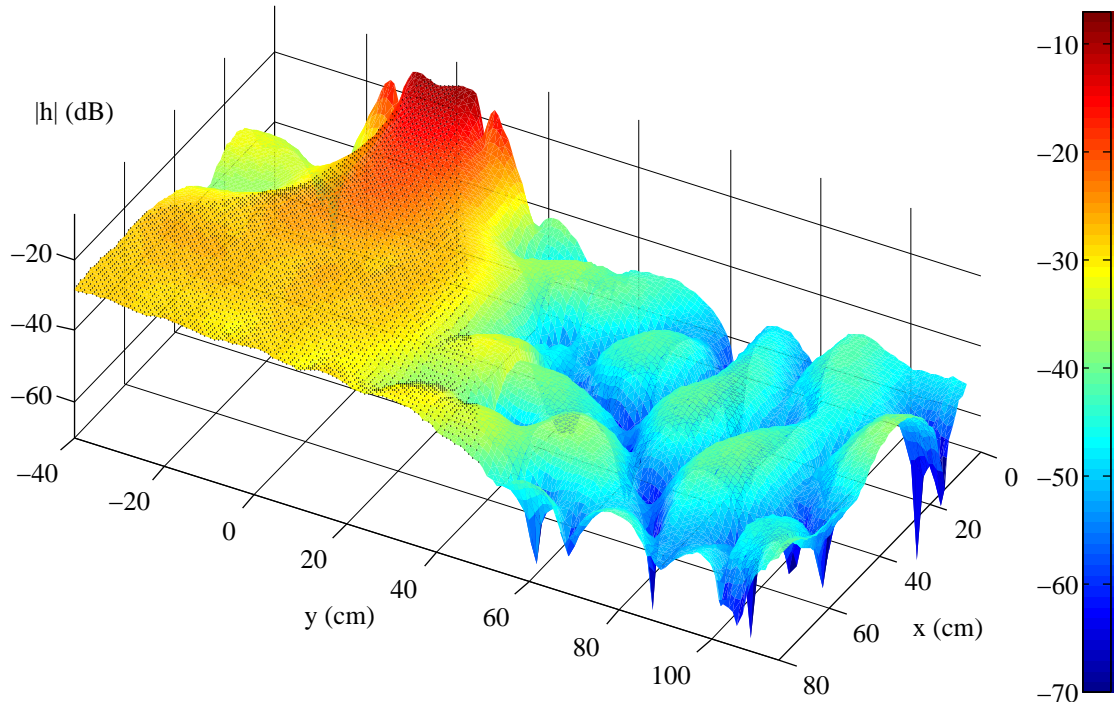


Figure 1.5: Transmission coefficient versus receive antenna position in the laboratory room. The transmit antenna is located at the origin (0,0) and aims at positive x-direction. Measurements within the half-power beamwidth cone of the transmit antenna are marked with dots.

**Laboratory area** Figure 1.5 depicts the transmission coefficient measured in a laboratory room. It can be seen that the direct signal component dominates reflected signals for a quite long transmission distance. This clearly distinguishes the laboratory scenario from the metal machining workshop scenario.

### Consequences for operation of RFID systems

In Figure 1.6 the UHF transmission coefficient at 866 MHz measured between the microstrip patch antenna and the shorted loop-slot antenna is plotted. The graph was taken from the channel measurement performed in the metal machining workshop.

Furthermore, a theoretical transmission coefficient in free space is plotted. It is as a scaled version of the electrical field strength  $E_\theta$  produced by a Hertzian dipole (Equation 1.3). For RFID systems radio transmission like in free space is a very theoretical and unlikely case because there are always objects present that scatter

or reflect radio waves. However, also with the presence of fading, this theoretical transmission coefficient can be used to estimate the maximum read range of an RFID system. Often a maximum read range of 10 m or even 20 m are found in literature. These numbers have to be reviewed with great caution because they rarely represent a read range at which transponders are reliably detected in a fading scenario. They rather denote a maximum read range that was achieved under laboratory conditions—either with the absence of fading in open space or an anechoic chamber, or by finding a local field maximum in a fading environment.

Just like in designing a mobile communication system, the presence of fading has to be considered when setting up an RFID system. In mobile communication systems, error-correcting codes are used to mitigate variations of the channel. For RFID applications however, the lack of computing power at the transponder only allows simple error detection for transmitted or received data sequences. Furthermore, transponders are powered by the electromagnetic field that is produced by the interrogator and thus will not respond at all if they rest at a faded position. When setting up a UHF RFID system a lot of effort has to be put into optimizing the propagation characteristics of the particular environment.

### 1.3.2 Reciprocity

In RFID systems a bidirectional radio link is established between an interrogator and a transponder. The transmission from the interrogator to the transponder is called the *forward link* whereas the transmission from the transponder back to the interrogator is called the *return link*. According to the theorem of reciprocity the transmission coefficients  $|h_{\text{Forward}}|$  and  $|h_{\text{Return}}|$  are equal only if the signals transmitted in both directions are identical.

But, since modulation is introduced at the transponder, the returned signal is different from the signal sent and thus—strictly speaking—the theorem of reciprocity can not be applied. However, if the channel is sufficiently stable versus frequency and time, reciprocity can be assumed. In the following paragraphs the effects of Doppler and delay spread are analyzed for RFID typical transmission signals and scenarios.

**Effect of delay spread** In current standardization maximum data rates of 640 kbit/s are allowed [4] which implies a signal bandwidth of  $B_S = 2.56 \text{ MHz}$ <sup>6</sup>. Since RFID is a short-range application that utilizes a strong line-of-sight signal

---

<sup>6</sup>The most bandwidth consuming modulation scheme used for the return link is similar to a Manchester code.

component for communication, the expected delay spread is in the order of magnitude of the delay along one read range  $r_{\text{Max}}$ . Signals traveling by more than one read range further than the line-of-sight component will be too weak to significantly disturb the channel. The maximum delay spread  $\tau_{\text{Max}}$  can thus be approximated as

$$\tau_{\text{Max}} \approx \frac{r_{\text{Max}}}{c_0} \quad (1.4)$$

where  $c_0$  denotes the speed of light. With a maximum read range of  $r_{\text{Max}} = 10$  m the coherence bandwidth  $B_c$  which describes the spectral region where the channel can be considered as flat, results in [21]

$$B_C = \frac{1}{\tau_{\text{RMS}}} > \frac{1}{\tau_{\text{Max}}} = 30 \text{ MHz}. \quad (1.5)$$

Here, the mean delay spread  $\tau_{\text{RMS}}$  is bounded by the maximum delay spread. Since the coherence bandwidth  $B_C$  is by far greater than the signal bandwidth  $B_S$ , reciprocity is not constrained by the delay spread of the channel. This was also confirmed by evaluating the frequency response of the measured channels. The variation of the channel response  $|h|$  within a 2.56 MHz bandwidth is below 1 dB.

**Effect of Doppler spread** A channel that is changing fast versus time can also constrain reciprocity. Time variant channels are characteristic for RFID applications because tagged objects are to be identified while moving. The period where the channel must not significantly change is given by the propagation delay in which a signal is returned by the transponder  $T_{\text{Prop}} = 2r_{\text{Max}}/c_0$ . A measure for how fast a channel changes is given by the coherence time  $T_C$ . Within one coherence time the channel coefficient can be considered as constant.  $T_C$  is given by

$$T_C = \frac{1}{\nu_{\text{RMS}}} > \frac{1}{\nu_{\text{Max}}} \quad (1.6)$$

where the mean Doppler spread  $\nu_{\text{RMS}}$  is bounded by the maximum Doppler spread  $\nu_{\text{Max}}$ .  $\nu_{\text{Max}}$  is related to the operating frequency  $f$  and the maximum velocity of movement  $v_{\text{Max}}$  occurring in the scenario according to  $\nu_{\text{Max}} = 2fv_{\text{Max}}/c_0$ . When equating  $T_{\text{Prop}}$  and  $T_C$ , the maximum velocity that still preserves reciprocity can be calculated. For a read range of  $r_{\text{Max}} = 10$  m and a frequency of  $f = 866$  MHz the maximum velocity that still preserves reciprocity is  $v_{\text{Max}} = 2.6 \cdot 10^6$  m/s. In RFID applications goods move much slower and thus

$$\frac{2r_{\text{Max}}}{c_0} = T_{\text{Prop}} \ll T_C \approx \frac{c_0}{2fv_{\text{Max}}} \quad (1.7)$$

is satisfied. Consequently, Doppler spread can be disregarded for the radio transmission in RFID systems as well.

### 1.3.3 Antennas for UHF RFID systems

#### UHF transponder antennas

Transponder antennas can be considered the weak point in the radio transmission chain of an RFID system. They are favored to be small which inevitably comes at the cost of low bandwidth and poor radiation efficiency. Furthermore, they are attached to objects that might contain fluids, metal, dielectric materials, or materials with high dielectric losses. Such objects often require specialized antenna designs or might even need boxing to generate some space around the transponder. The reason for this is that electrically-small antennas are very prone to proximity effects. Materials in the proximity of the transponder antenna cause a shift in center frequency and input impedance—often referred to as detuning [22]. This effect impairs the matching between the transponder antenna and the transponder chip which consequently reduces the power available to operate the chip's digital circuits. Lossy materials in the proximity of the antenna will moreover absorb power. In [23] for instance, transponders were placed on empty corrugated fiberboard shipping containers. Measurements were taken with the boxes empty, filled with rice jars, and filled with polyethylen (PET) water bottles. The read rate of a palette of such containers was then evaluated. Where over 99% of the empty boxes were recognized, only 81% of the boxes with rice filled jars and 25% of the boxes filled with water bottles were read. Also keep in mind that objects carrying the transponder antenna range from pharmaceuticals to railroad engines, so there is no one-fits-all antenna solution.

Transponder antennas used for most applications in UHF RFID systems consist of a printed or etched metallization on top of a thin and flexible sheet of plastic or paper. Often transponders are equipped with an adhesive film and can be attached to flat surfaces. Many fancy shapes of such antennas are found but technically most of them are dipole antennas having meandered conductors and a widened metallization at the dipole ends functioning as an end capacitance [24]. Both measures allow to size down the antenna compared to the half-wavelength dipole [25]. To match the impedance of such electrically-small dipole antennas with the input impedance of transponder chips, a matching structure in form of a little loop or slit is implemented in the center of the dipole. The length of such antennas ranges between 5 cm and 15 cm. For even smaller transponders a metallization in the form of a loop is used. They are commonly referred to as near field or loop antennas. Those antennas are also equipped with a similar matching structure.

The radiation pattern of an electrically-small dipole antenna approaches that of a Hertzian dipole. Radiation of small loop antennas on the other hand is similar to

that of a magnetic dipole. Both antenna structures—and thus most transponder antennas—radiate linear polarization and are omnidirectional in one plane.

The antenna described in Chapter 3 uses a folded up resonator structure to produce radiation that is linearly polarized. The gain pattern of this credit card sized antenna is similar to that of a Hertzian dipole. In addition to the functionality at 866 MHz it can also be used in the HF band at 13.56 MHz.

### **UHF interrogator antennas**

While the transponder antenna is optimized to cope with the radio frequency characteristics of the objects that are to be tagged, the interrogator antenna has to deal with the scenario. The choice and the installation of the interrogator antenna in its environment has to be carefully considered. A setup has to be found where fading is avoided as much as possible—especially in the region where the transponders are situated. This is best achieved by an antenna that on the one hand uniformly illuminates the region where the tagged objects are expected. On the other hand the gain pattern of the antenna should mask potential reflectors that would enhance multipath propagation. Some reflectors might also be hidden by using absorbing material. If even higher reliability is desired, more interrogator antennas can be deployed and used in a time division multiplex scheme.

It was explained above that most transponder antennas radiate linear polarization. When an interrogator antenna is used that radiates a linear polarized wave as well, the alignment between the two antennas is important. In applications where the orientation of the transponders is undetermined, the received power at the transponder antenna output can be dramatically reduced if the antennas are misaligned. It is therefore good practice to use interrogator antennas that emit circular polarization. The employment of antennas radiating circular polarized waves comes with an additional transmission loss of 3 dB when communicating with linearly polarized transponder antennas because of polarization mismatch.

For many RFID systems microstrip patch antennas are a good choice because of their wide main lobe and well suppressed side lobes. Also, they are low-profile which allows to mount them in confined spaces like gates or doors. With minor modifications patch antennas also radiate circular polarization. The antenna described in Chapter 4 fulfills all of the above mentioned requirements and also features separate well-isolated ports for transmitting and receiving signals.

## 1.4 Radio transmission at UHF versus inductive coupling at HF

Figure 1.6 compares the transmission coefficient between two UHF antennas and two HF coils versus distance. At UHF, transmission between a square patch antenna with overall dimensions of 40 cm × 40 cm and a loop slot antenna with dimensions of 7 cm × 4 cm is depicted. A representative measurement result obtained in a fading environment as well as the theoretical curve for free space transmission is shown. Furthermore, the power transmission between two loosely coupled HF coils that have roughly the same dimensions as the UHF antennas is shown. Even if the HF transmission coefficient might shift up and down depending on the  $Q$ -factors chosen for the interrogator and the transponder (see Section 1.2.1) the principal difference between the HF and the UHF transmission becomes clear.

**Free space loss** At UHF, power received by the transponder decreases inversely proportional to the transmission distance squared  $P_{\text{Transponder,UHF}} \sim 1/r^2$ . Conversely, at HF, received power is related to the transmission distance according to  $P_{\text{Transponder,HF}} \sim 1/r^6$ . This shows that in principle, UHF systems outperform HF systems in terms of read range. For many applications read range might be essential, but if low costs and high reliability for low-range reading are important, HF systems are often preferred. For applications like personal admission control where a smart-card<sup>7</sup> has to be placed on top of the interrogator antenna, inductive coupling is often favored. Furthermore, in HF systems the quick decay of received power is often exploited to restrict the read range to a defined region. Interrogator coil arrangements can be optimized to produce a uniformly distributed magnetic field which allows to achieve reliable transponder recognition within a defined area of operation.

**Fading** From Figure 1.6 it can be seen that the measured path loss of an exemplary UHF scenario strongly deviates from the idealized transmission in free space. This fading is a characteristic of UHF radio transmission and does not appear in HF RFID systems. Fading relativizes the advantage of high read range—it comes at the cost of reliability. Whether or not read range can be compromised certainly depends on the application. Some measures for taking control of fading were described in Section 1.3.3. An experimental study on the impact of fading in a typical reading gate application can be found in [26]. The authors perform a detailed analysis of the field strength within the gate area where a pallet loaded with various goods is

---

<sup>7</sup>Smart-cards are credit card sized plastic cards containing an HF transponder.

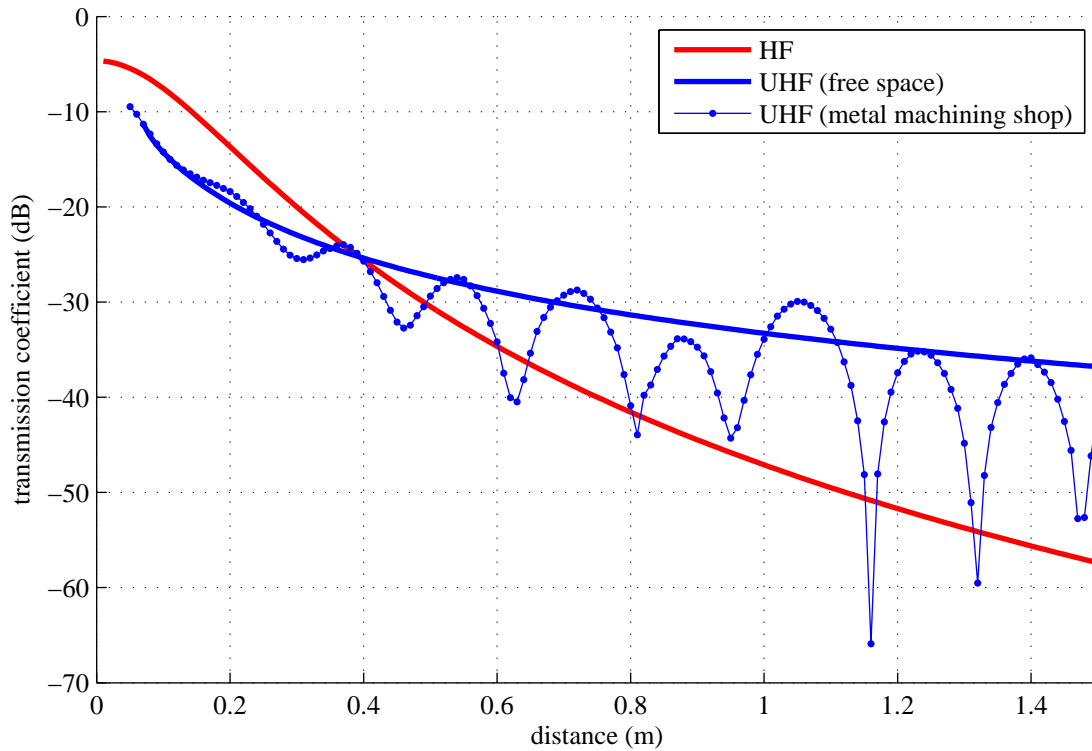


Figure 1.6: HF and UHF transmission coefficient versus transmission distance.

placed. It is argued that, even with state-of-the-art technology, a highly reliable system could not be obtained.

**Detuning** Once a transponder is put together with an object, the behavior of the antenna or coil will change because of the proximity of materials. At HF, conductors and materials that have ferromagnetic properties will alter the characteristics of a transponder coil. The proximity of such objects leads to a drop in a transponder's resonant frequency which reduces the voltage step-up at 13.56 MHz. Consequently, the read range is reduced. Often, such effects can be countered by designing transponders that have a higher-than-needed resonant frequency to make them more robust against detuning.

With UHF transponders on the other hand conducting, ferromagnetic, and in addition to those also dielectric materials degrade the antenna performance. Detuning of an antenna that was optimized to best operate in free space causes a change of its input impedance which results in a mismatch between antenna and transponder chip. Water which has a relative dielectric constant of  $\epsilon_r \approx 80$  at 915 MHz [27] can severely detune an RFID transponder. In [28] a reduction of read range by

85% and more was measured for some commercially available transponders near water. Similar conclusions are drawn for the proximity to metal or food products [29, 30].

To counter detuning, a frequency hopping technique is provided in UHF RFID standards. The interrogator is supposed to switch between a set of frequencies to improve the transponder recognition rate. Depending on local radio regulations the bandwidth allocated for this technique is between 3 MHz (Europe) and 26 MHz (USA). However, from the practical measurement results presented in [28], it can not be concluded that the frequency hopping technique brings a significant improvement when reading detuned transponders.

If—in spite of these considerations—a UHF system has to be used for tagging such objects, a specialized transponder antenna design is necessary that takes the involved materials and their appearance into account. Examples of such antenna designs can be found in [31, 32, 33, 34].

**Absorption** Many materials also absorb electromagnetic energy and convert it into heat. This is much more pronounced at UHF compared to HF because losses in good conductors increase with frequency according to  $\alpha_{\text{cond}} \sim \sqrt{f}$  and losses in dielectric materials increase linearly with frequency  $\alpha_{\text{diel}} \sim f$  [35, 36]. The electric loss tangent of hair shampoo for instance might be as high as  $\tan(\delta) = 1.2$  [27]. Waves propagating through such lossy media will certainly undergo strong attenuation.

**Shielding** A conductor that is exposed to an alternating electromagnetic field will cause a reflection of energy and thus shield the area behind it. Although the physical principles are identical for both frequency bands, shielding in the HF domain is often explained by the generation of eddy-currents that cause an opposed field which cancels out the original magnetic field.

Metals can be considered as good shields if they are much thicker than the skin depths  $\delta = 1/\sqrt{\pi f \mu \sigma}$ <sup>8</sup>. A good conductor like copper has a skin depth of approximately  $\delta_{\text{UHF}} \approx 2.2 \mu\text{m}$  at 866 MHz and  $\delta_{\text{HF}} \approx 18 \mu\text{m}$  at 13.56 MHz. This shows that most metallic objects can be considered as good reflectors. However, very thin metal foils might be the exception for the HF band.

At UHF, dielectric materials can cause shielding as well. In [27] for instance, it is found that the reflection on an air / water-surface introduces even more attenuation than the absorption when propagating through some 10 cm of water. which impair the transmission.

---

<sup>8</sup> $f$  denotes the frequency,  $\mu$  the permeability, and  $\sigma$  the bulk conductivity of the metal.

## 2 Antenna / chip interaction

In this section the interaction between the transponder antenna and the transponder chip is described. For UHF, the mechanism of forward and return link is explained considering a simple Thévenin equivalent circuit that represents the antenna as a source, and the chip as a load (Figure 2.1). While this equivalent circuit can be promptly applied for the forward link where power matching between the antenna and the chip has to be achieved, its use for the return link is not that trivial. However, by establishing a well thought-out power budget for the Thévenin source, valid results are obtained for the scattered power.

The progression illustrated in the following starts out with known transponder chip impedances and describes the finding of an optimum antenna impedance based on a power optimization for the forward link. By the use of the equivalent circuit, the antenna current for the two transponder chip states is derived. An analysis of the results yields a second optimum antenna impedance that maximizes the power contained in the modulated backscattered signal and thus improves the transmission back to the interrogator—the return link. The overall system performance is then investigated and the effects on the link budget are examined. With that, it is shown how a deviation from either of the two optimum antenna impedances, that might be a result of detuning or production tolerances, affects the power available to the chip or for the return link.

### 2.1 Matching antenna and chip impedances

To get the most power from the electromagnetic field into the chip, antenna and chip have to be matched. Figure 2.1 shows the Thévenin equivalent circuit of the tag antenna and the tag chip impedance. Since the input impedance of the chip  $Z_{\text{Chip}}$  can not be chosen arbitrarily due to technological limits, the antenna has to be designed to match the chip as good as possible. The power matching condition is  $Z_{\text{Ant}} = Z_{\text{Chip}}^*$ . Theoretically, in case of perfect matching, the entire power available at the tag antenna output  $P_{\text{RX,Tag}}$  can be used by the chip. Here, it has to be mentioned that transponder chips are highly non-linear loads. Apart from a principal change of input impedance versus power determined by measurements in

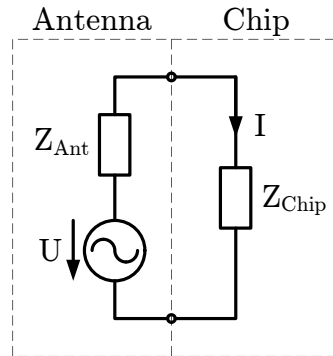


Figure 2.1: Equivalent circuit of tag antenna and chip.

Section 6.6, the impedance itself is nonlinear meaning that voltage  $u$  and current  $i$  are not related according to  $u = Z_{\text{Chip}}i$ . However, when considering operation at the fundamental frequency and at a certain power level only, an input impedance can be defined that linearly relates current and voltage. Due to the nonlinear nature of the load, a fraction of the incident power will be transferred to harmonic frequencies. Whether this power is retransmitted or remains in the transponder chip depends on the matching between antenna and chip at each harmonic frequency. Thus—strictly speaking—not the entire available power can be used by the transponder chip. The exception would be an antenna that presents lossless termination at all harmonic frequencies. However, since many antennas have periodic resonances, some power will indeed be reradiated at harmonic frequencies also.

In Figure 2.2 the power reflection coefficient at the chip’s input versus the chip impedance is plotted for a given antenna impedance. The curves were computed from Equation 2.13. Indeed, best power matching is achieved when the chip impedance equals the complex conjugate of the antenna impedance. A Smith diagram normalized to  $50\ \Omega$  was chosen to highlight that an antenna impedance of  $Z_{\text{Ant}} = (28 + 179j)\ \Omega$  is highly reactive. This is quite typical for RFID transponder antennas and antenna designers have to deal with such impedances. Apart from difficulties in the design process, advanced measurement methods like the one described in Chapter 5 are necessary to characterize RFID transponder antennas in terms of input impedance and gain.

## 2.2 Scattering properties of antennas

Before going into details with the mechanism of the return link it seems important to explain how an antenna scatters power when exposed to an electromagnetic field.

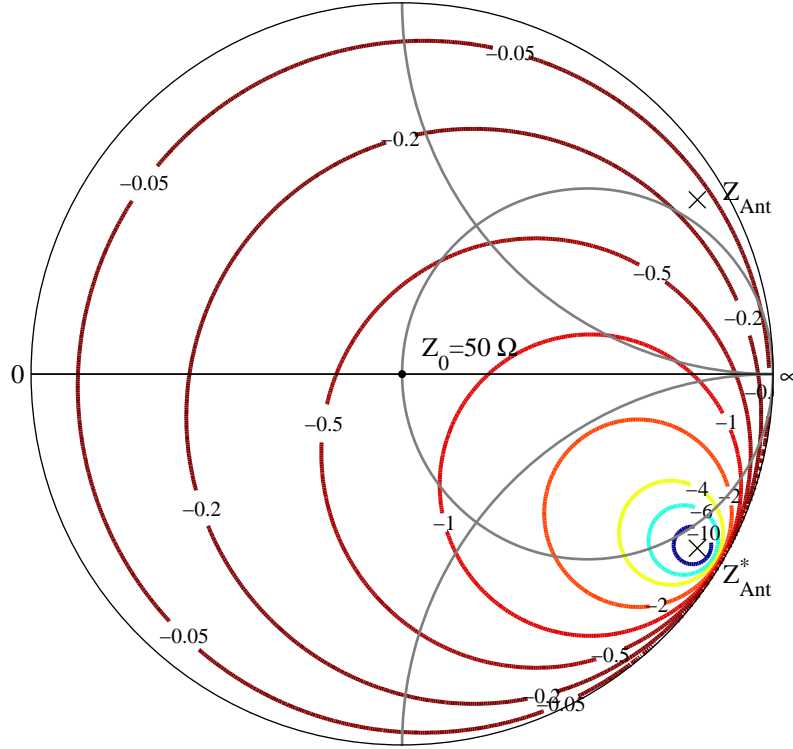


Figure 2.2: The Smith diagram ( $Z_0 = 50 \Omega$ ) shows lines of constant power reflection coefficient at the chip input in dB versus chip input impedance. The antenna impedance is  $Z_{\text{Ant}} = (28 + 179j) \Omega$ .

First, every antenna scatters a part of the incident electromagnetic energy in its structural mode [37]. This scattering is caused by induced currents in the antenna structure and is often normalized to the antenna's short circuit current. Scattering in the structural mode can thus not be used for a return link data transmission because it is not influenced by a change of the chip impedance. The structural scattering component is thus not relevant in RFID applications. It is similar to a reflected signal that is caused by an interacting object in space. However, there exist a certain class of *minimum-scattering antennas* [38] that indeed may scatter zero power in their structural mode. Although many simple RFID transponder antennas are such antennas when operated in free space, this property is in general not fulfilled when the antenna interacts with its environment and is subject to proximity effects. Thus, an analysis of scattering from RFID transponder antennas must not be limited to minimum-scattering antennas.

Second, there is the scattered field component that is produced by the antenna mode [37]. The antenna mode converts an electromagnetic field that is incident upon the antenna into an electric current at the antenna port. Conversely, for

transmitting, the antenna mode generates radiation that is caused by the current fed into the antenna port. When antennas are used to transmit and receive signals one utilizes the antenna mode. An incident wave impinging on a receive antenna will excite a distribution of currents and charges in the antenna structure which will give rise to a wave that proceeds out of the antenna port. If an antenna is perfectly matched, this wave is entirely dissipated in the load. However, there is still current flowing upon the antenna port which causes a radiation by the receiving antenna. This is a fundamental theorem in antenna scattering that has been derived by a number of authors in the 1940s [39, 40, 41].

I found the more recent derivation provided by Collin in the Appendix of [42] very helpful. In particular he states that the total scattered field of both, the structural and the antenna mode of a receiving antenna  $\mathbf{E}_s(Z_{\text{Chip}})$  for an arbitrary load impedance  $Z_{\text{Chip}}$  can be written as

$$\mathbf{E}_s(Z_{\text{Chip}}) = \mathbf{E}_s(Z_{\text{Chip}} = \infty) - \underbrace{\frac{U}{Z_{\text{Chip}} + Z_{\text{Ant}}}}_I \mathbf{E}_r. \quad (2.1)$$

This total scattered field consists of the

- structural mode component  $\mathbf{E}_s(Z_{\text{Chip}} = \infty)$  which describes the scattering of a wave incident upon the open circuited antenna, and of the
- antenna mode component  $I\mathbf{E}_r$  which describes the reradiation caused by the antenna current  $I$ . The antenna current  $I$  is influenced by the load  $Z_{\text{Chip}}$  that is connected to the antenna port and can be modulated by changing  $Z_{\text{Chip}}$ .

In general, the radiation pattern of the antenna mode (specified in  $\mathbf{E}_r$ ) is not equivalent to the radiation pattern of the structural mode that is contained in  $\mathbf{E}_s$  [38, 42].

Please note that the levels of scattered power in the structural mode and the reradiated power in the antenna mode might differ significantly and depend on the particular structure of the antenna and on the antenna's load situation, respectively. In general the scattered power can be greater than, equal to, or smaller than the absorbed power [43].

## 2.3 Backscatter modulation

The return link is achieved by a substantial impedance change of the chip. This is done with a shunt transistor that is implemented in the input circuitry of the transponder chip. Switching on this transistor destroys matching between chip and antenna which results in power reflection at the chip. The reflected power is

retransmitted by the transponder antenna. To retransmit the entire received power, the magnitude of the chip's input reflection coefficient has to be 1 ( $|\rho_{\text{Chip}}| = 1$ ). Since this ideal condition can not be achieved by a shunt transistor, an imperfect reflection at the tag chip is observed. Furthermore, when the shunt transistor is off, matching might not be perfect because of production tolerances or detuning of the antenna. In the following section the mechanism of the return link will be analytically derived for a periodic switching between the two input impedance states of the transponder chip.

In this calculation the power available at the antenna output  $P_{\text{RX,Tag}}$  that relates to the antenna mode is assumed constant. This is reasonable because the antenna is put into a static radiation field which is produced by an interrogator. The power that is available at the antenna port is thus defined by the radiant flux density  $T$  of the incident field and the effective antenna area  $A_e$  according to

$$P_{\text{RX,Tag}} = T A_e. \quad (2.2)$$

Of course this power is only delivered to the chip impedance if antenna and chip are matched according to  $Z_{\text{Ant}} = Z_{\text{Chip}}^*$ . If this is the case then the amplitude of the equivalent Thévenin open source voltage  $U$  from Figure 2.1 can be determined with

$$U = \sqrt{8P_{\text{RX,Tag}}\text{Re}(Z_{\text{Ant}})}. \quad (2.3)$$

This is a property of the antenna and the impinging field only. The amplitude of the antenna current  $I$ , that is obtained for an arbitrary chip impedance  $Z_{\text{Chip}}$  that is connected to the antenna port can be calculated with

$$I = \frac{U}{Z_{\text{Ant}} + Z_{\text{Chip}}}. \quad (2.4)$$

For the case of perfect matching the antenna current solves to

$$I_{\text{Matched}} = \frac{U}{2\text{Re}(Z_{\text{Ant}})}. \quad (2.5)$$

This current together with the antenna impedance represents the available power that the antenna draws from the incident electromagnetic field and that can be delivered to a load. If a current different from  $I_{\text{Matched}}$  is observed at the antenna port then a part of the available power picked up by the antenna is not delivered into the load.

The applicability of the Thévenin equivalent circuit for scattering of antennas has been heavily discussed in recent literature [44, 43, 45, 46, 47, 48, 49]. The main concern of the authors is that the power scattered by an antenna is equated with the

power dissipated in the antenna impedance  $Z_{\text{Ant}}$ , which is incorrect. Simple examples can be constructed to confirm this [43]. Furthermore, the Thévenin equivalent circuit does not implicate at all the presence of scattering which is caused by the structural mode of an antenna [42]. The reradiated power can in fact only be computed by integration of the Poynting vector over a closed surface surrounding the antenna. There, the electromagnetic field around the antenna from which the Poynting vector is calculated is a superposition of the original impinging field, the field scattered in the structural mode of the antenna, and the field reradiated by the antenna which is caused by the current  $I$  [39]. A calculation of the power reradiated by an RFID transponder has been published very recently in [50]. Although the results are the same, the derivation presented here is simpler and more intuitive. Additionally, I give an analytical expression for the optimum antenna impedance.

In the following the interaction between a transponder antenna and an RFID chip is analyzed in detail. According to Equation 2.4, the switching between the two input impedance states  $Z_{\text{Chip1}}$  and  $Z_{\text{Chip2}}$  causes two different currents at the antenna port:

$$\begin{aligned} I_1 &= U \left( \frac{1}{Z_{\text{Ant}} + Z_{\text{Chip1}}} \right) \\ I_2 &= U \left( \frac{1}{Z_{\text{Ant}} + Z_{\text{Chip2}}} \right) \end{aligned} \quad (2.6)$$

For further consideration of the return link it has to be understood that the antenna current is composed from the currents  $I_1$  and  $I_2$ . According to the pattern of switching between the chip's impedance states, either  $I_1$  or  $I_2$  is present at the antenna port at a point of time. The antenna current can thus be considered as a vector modulated signal for which the modulation signal switches between two complex states.

In general, this vector modulated signal  $I(t)$  will consist of one spectral component at the carrier frequency  $\omega_c$  of the incident wave, and an infinite number of spectral components that were originally contained in the baseband modulation signal. After modulation these signals are located around the carrier frequency. The latter signal components, which are usually called the sidebands, are the ones that can be used to transmit information back to the interrogator. For prompt switching between  $I_1$  and  $I_2$ , the sidebands spread over a theoretically infinite frequency range. In practice however, the impedance of the antenna strongly depends on the frequency which entails a narrowband frequency response of the antenna-chip system. Thus, harmonic signal components outside of the resulting bandwidth are damped.

To simplify matters, a rectangular modulation signal with a duty cycle of 50% and a frequency of  $\omega_m$  for switching between the two chip impedance states is assumed. This simple modulation is very similar to the modulation schemes proposed in the standards and thus considered adequate for a principal study of backscattering. With such a modulation at the chip input, the antenna current  $I(t)$  looks like shown in Figure 2.3. For better illustration an antenna impedance of  $Z_{\text{Ant}} = (40 + 160j) \Omega$  was chosen. This represents the general case where neither perfect power matching nor optimal modulation efficiency is obtained. In the case of perfect power matching ( $Z_{\text{Ant}} = Z_{\text{Chip1}}^*$ ),  $I_1$  would be equal to  $I_{\text{Matched}}$ . Here, it is essential to remind that the power dissipation in the Thévenin antenna impedance can in general not be equated with the power reradiated by the antenna. In fact, from Figure 2.3, this is obvious because a current  $I_2$  that is smaller than  $I_{\text{Matched}}$  would in this case violate the power budget for the antenna. Namely, such an  $I_2$  causes less power dissipation in the load  $P_{Z_{\text{Chip}}}$ , and simultaneously, less power dissipation in the antenna impedance  $P_{Z_{\text{Ant}}}$ . If one would falsely interpret the power dissipated in  $Z_{\text{Ant}}$  as reradiated power, then the power budget can not be satisfied. For a given available power  $P_{\text{RX,Tag}}$  a decrease of the power delivered to the load must on the other hand lead to an appropriate increase of reradiated power. Similar conclusions can be drawn for the current  $I_1$  which is higher than  $I_{\text{Matched}}$ . It should be noted that for the particular case of a *perfectly matched minimum-scattering antenna* the dissipated power in the antenna impedance  $P_{Z_{\text{Ant}}}$  is equal to the power reradiated by the antenna. However, this does not represent the general case as often assumed in literature.

The current  $I(t)$  shown in Figure 2.3 is not yet band limited to demonstrate that an amplitude modulation as well as a phase modulation of the carrier is present. The latter is identified by the discontinuous phase when switching between the states. Figure 2.4 shows the spectral components of  $I(t)$ .

For the calculation of the reradiated power, the modulated signal has to be decomposed into two terms. The first term represents a continuous wave at the carrier frequency  $\omega_c$  that can not be used to transmit information. It adds up with the scattered power produced by the structural mode of the antenna and is lost in space. In the spectrum this first term is seen at  $\omega_c$ .

The second term on the other hand represents a purely phase modulated signal with a phase offset of  $180^\circ$  between the two switching states. This signal holds all information that is contained in the baseband modulation signal and can be demodulated at the interrogator. In the spectrum it consists of all signal components to the left and right of  $\omega_c$  but—and this is essential—does not contain a continuous carrier signal at  $\omega_c$ . This new signal is a result of the periodically switched reflection at the transponder chip input. Since it only contains frequency components

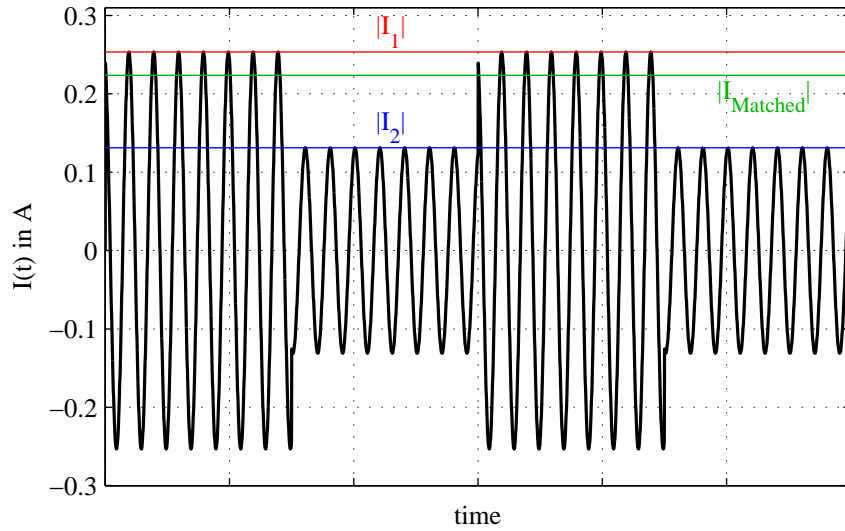


Figure 2.3: Antenna current versus time during modulation of the chip input impedance. The antenna impedance was chosen  $Z_{\text{Ant}} = (40 + 160j) \Omega$  and the chip impedances were taken from Table 2.1. The current shown in this figure is normalized to a received power of  $P_{\text{RX,Tag}} = 1 \text{ W}$ .

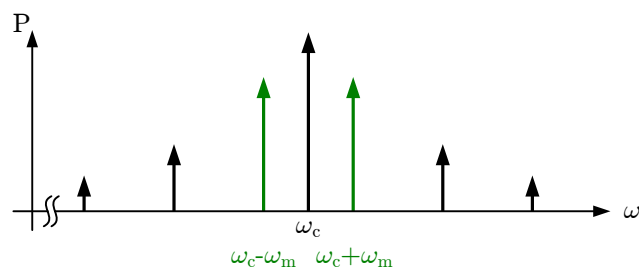


Figure 2.4: Spectrum of the backscattered signal for periodic hard switching of the chip input impedance with a 50 % duty cycle. The power of the spectral components that are relevant for the return link (green) is  $P_{\text{DSB}}$ .

other than the carrier frequency, it does neither interfere with the continuous sinusoidal antenna current at  $\omega_c$ , nor does it influence the reradiated power at  $\omega_c$ . It is but a signal that is rather *normally radiated* and not scattered by the receiving antenna.

The amplitude of the purely phase modulated portion of  $I(t)$  can be calculated from the currents  $I_1$  and  $I_2$  according to

$$\hat{I}_{\text{PM}} = \frac{|I_1 - I_2|}{2}. \quad (2.7)$$

$I_{\text{PM}}(t)$  is a signal with constant envelope so it is very simple to calculate the power that is delivered into the antenna by this portion of the signal. In contrast to calculating the reradiated power at the carrier frequency by solving the surface integral, here the power delivered into the antenna can be directly computed from the current  $\hat{I}_{\text{PM}}$  and the real part of the antenna impedance  $\text{Re}(Z_{\text{Ant}})$  with

$$P_{\text{PM}} = \frac{\hat{I}_{\text{PM}}^2}{2} \text{Re}(Z_{\text{Ant}}). \quad (2.8)$$

With the filter characteristic of the antenna-chip system, harmonic signals may be cut off. The spectral components that have to be preserved for data transmission are located at  $\omega_c + \omega_m$  and  $\omega_c - \omega_m$ . Since in RFID standardization a modulation frequency as high as 640 kHz can be chosen for highest data rate, the filter characteristic of the antenna will indeed be relevant and might in fact cut off harmonic signals. It is thus reasonable to define the power that is reradiated towards the interrogator by the power that is contained in the two very first side signals (shown in green in Figure 2.4). Let us call this power  $P_{\text{DSB}}$  according to the term *double sideband*.

A decomposition of  $I_{\text{PM}}(t)$  into its Fourier coefficients yields that a fraction of 81% ( $8/\pi^2$ ) of the total power  $P_{\text{PM}}$  is contained in the first side signals. Thus the power of the filtered reradiated signal that contains all information about the chip input impedance switching can be written as

$$P_{\text{DSB}} = \frac{8}{\pi^2} P_{\text{PM}} = \frac{4 \hat{I}_{\text{PM}}^2}{\pi^2} \text{Re}(Z_{\text{Ant}}), \quad (2.9)$$

or in terms of antenna and chip impedances by using Equation 2.7 and Equation 2.6 as

$$P_{\text{DSB}} = \frac{8}{\pi^2} P_{\text{RX,Tag}} \frac{\text{Re}(Z_{\text{Ant}})^2 \cdot |Z_{\text{Chip1}} - Z_{\text{Chip2}}|^2}{|Z_{\text{Ant}} + Z_{\text{Chip1}}|^2 \cdot |Z_{\text{Ant}} + Z_{\text{Chip2}}|^2}. \quad (2.10)$$

From the expression in the numerator it can immediately be seen that the power contained in the first side signals is directly affected by the difference between the

two chip input impedances measured in the complex plane. This makes sense because if the antenna is perfectly matched to one of the impedances—let us make it  $Z_{\text{Chip1}}$  for now—no power will be reflected in this state. When switching to the other state, a strong reflected signal is favored and only achieved if the second impedance  $Z_{\text{Chip2}}$  coarsely violates the matching condition. Chip designers often provide the *delta gamma value*  $\Delta\Gamma$  in their datasheets which relates to the difference between the two impedance values measured in the Smith chart (also see Section 6.7). Furthermore, when looking at the denominator, it is seen that complex conjugate matching of the antenna impedance with either of the two chip impedances reduces the corresponding term to the square of two times the real part of the antenna impedance  $|2\text{Re}(Z_{\text{Ant}})|^2$ . The signal strength for the return link is thus improved when choosing the antenna impedance close to the complex conjugate of the chip impedances.

From Equation 2.10, a particular antenna impedance can be found that optimizes the power contained in the sidebands. Therefore,  $P_{\text{DSB}}$  has to be partially derived for the real part  $R_{\text{Ant}}$  and the imaginary part  $X_{\text{Ant}}$  of the antenna impedance. Setting the derivatives zero and solving for  $R_{\text{Ant}}$  and  $X_{\text{Ant}}$  yields a global maximum for  $P_{\text{DSB}}$  at:

$$\begin{aligned} R_{\text{Ant,Mod}} &= \sqrt{R_{\text{Chip1}}R_{\text{Chip2}} \frac{(R_{\text{Chip1}} + R_{\text{Chip2}})^2 + (X_{\text{Chip1}} - X_{\text{Chip2}})^2}{(R_{\text{Chip1}} + R_{\text{Chip2}})^2}} \\ X_{\text{Ant,Mod}} &= -\frac{R_{\text{Chip2}}X_{\text{Chip1}} + R_{\text{Chip1}}X_{\text{Chip2}}}{R_{\text{Chip1}} + R_{\text{Chip2}}} \end{aligned} \quad (2.11)$$

This very interesting result shows that for maximum power in the side signals the antenna must not be matched to either of the chip input impedance states. Consequently, matching antenna and chip according to

$$\begin{aligned} R_{\text{Ant,Pwr}} &= R_{\text{Chip1}} \\ X_{\text{Ant,Pwr}} &= -X_{\text{Chip1}} \end{aligned} \quad (2.12)$$

may transfer the most power into the chip, but will not achieve the optimum return link. That said, it is clear that one has to decide which optimization criterion to choose. An obvious thought is to select power matching in forward link limited systems and optimum modulation efficiency in return link limited systems. Whichever is chosen, with the Equations 2.11 and 2.12, the antenna designer can immediately find the optimum antenna impedance by only knowing the two impedance states of the transponder chip for which the antenna has to be designed.

## 2.4 Effects on a system shown with a numerical example

In the following, the findings from Section 2.3 are used to determine an antenna impedance for a given transponder chip. The chip's input impedance values used in this example were determined by measurement. Some transponder chips from different manufacturers were selected and the impedances in the absorbing state with the internal shunt transistor switched off ( $Z_{\text{Chip1}}$ ) and in the reflecting state with the shunt transistor switched on ( $Z_{\text{Chip2}}$ ) were characterized. Details on the measurement campaign can be found in Chapter 6. The chosen chip impedance values match the principal properties of state-of-the-art transponder chips. Table 2.1 summarizes the values used in this example, and also gives the two optimal antenna impedances determined in Section 2.3 and Section 2.1.

Table 2.1: Chip impedances and possible antenna impedance.

symbol	value	description
$Z_{\text{Chip1}}$	$= (28 - 179j) \Omega$	absorbing state (shunt transistor off)
$Z_{\text{Chip2}}$	$= (88 - 113j) \Omega$	reflecting state (shunt transistor on)
$Z_{\text{Ant,Pwr}}$	$= (28 + 179j) \Omega = Z_{\text{Chip1}}^*$	maximum power put into the chip
$Z_{\text{Ant,Mod}}$	$= (57 + 163j) \Omega$	maximum power put into the sidebands

This page was intentionally left blank.

### 2.4.1 Link budget

The link budget presented in Figure 2.5 gives an overview of the radio transmission of an RFID system. The power levels and attenuation factors are explained in Table 2.2.

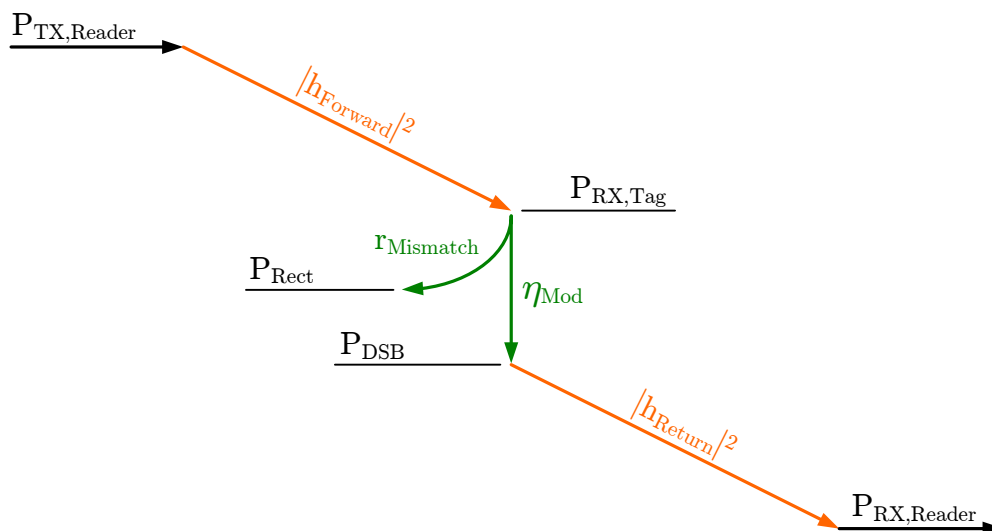


Figure 2.5: Link budget of the entire radio transmission.

Table 2.2: Summary of variables used for the link budget in Figure 2.5.

symbol	description
$P_{TX,Reader}$	power fed into the reader antenna
$ h_{Forward} ^2$	forward link transmission coefficient
$P_{RX,Tag}$	power available at the tag antenna output
$r_{Mismatch}$	loss factor caused by imperfect matching between antenna and chip
$P_{Rect}$	power available for rectification in the RFID chip
$\eta_{Mod}$	modulation efficiency
$P_{DSB}$	sideband power fed back into the tag antenna
$ h_{Return} ^2$	return link transmission coefficient
$P_{RX,Reader}$	sideband power available at the reader

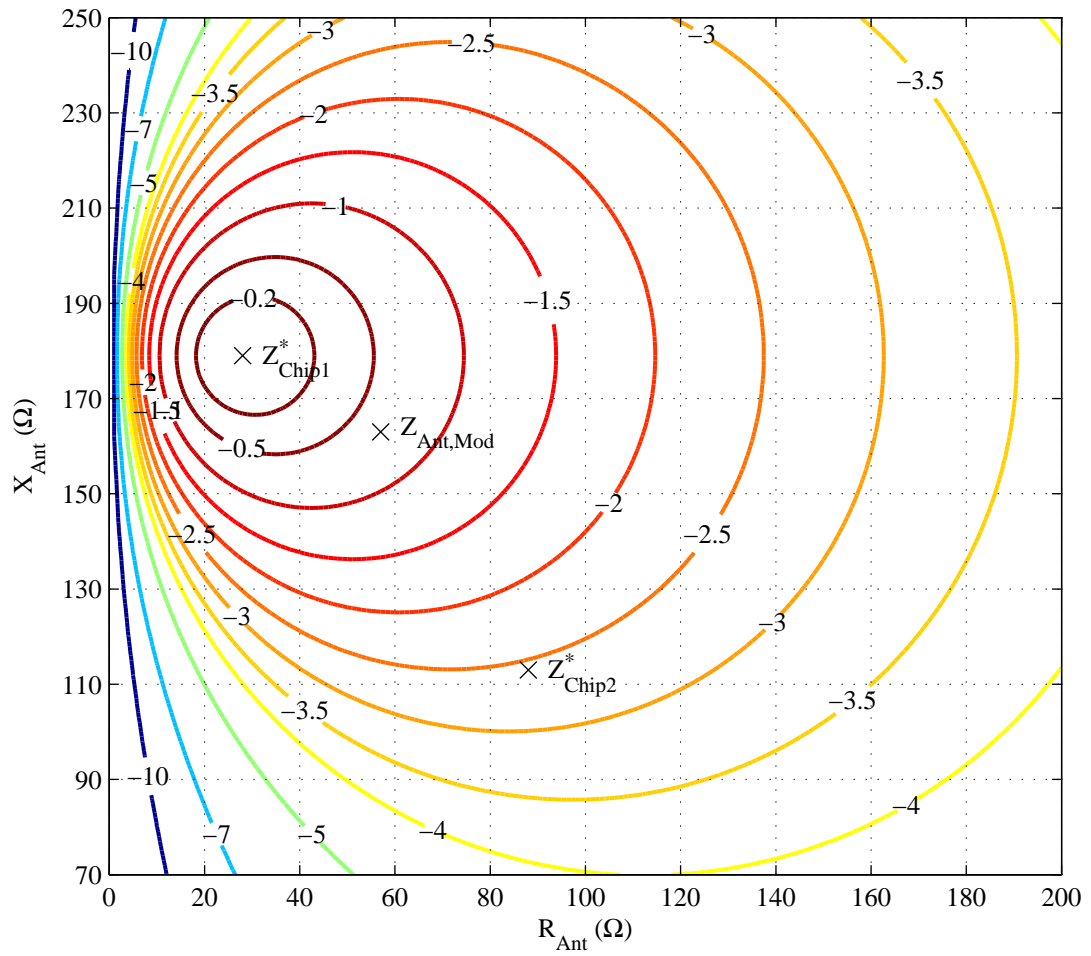


Figure 2.6: Matching loss factor  $r_{\text{Mismatch}}$  in dB versus antenna impedance.

### 2.4.2 Forward link

The transmitted continuous wave signal  $P_{\text{TX,Reader}}$  is fed into the interrogator antenna. The forward link transmission coefficient  $|h_{\text{Forward}}|^2$  that includes the channel coefficient and the actual gain of the antennas leads to the power  $P_{\text{RX,Tag}}$  that is available at the transponder antenna port.

The loss factor  $r_{\text{Mismatch}}$  describes the ratio of the the power accepted by the transponder chip and the available power at the antenna port. If matching is perfect ( $Z_{\text{Ant}} = Z_{\text{Chip1}}^*$ ) the entire power received by the antenna is available to the chip and consequently at its rectifier when in absorbing mode ( $r_{\text{Mismatch}} = 1$ ). If  $Z_{\text{Ant}}$  deviates from  $Z_{\text{Chip1}}^*$  some power is reflected at the chip input and thus not available for supplying the transponder chip's circuitry ( $r_{\text{Mismatch}} < 1$ ). This means that rather than the entire available power, only a part of it, namely  $P_{\text{Rect}}$ , can be used by the chip. From Equation 2.4 and Equation 2.5 the loss factor  $r_{\text{Mismatch}}$  that is caused by mismatching can be written as

$$r_{\text{Mismatch}} = \frac{P_{\text{Rect}}}{P_{\text{RX,Tag}}} = \frac{|I_1|^2 \text{Re}(Z_{\text{Chip1}})/2}{|I_{\text{Matched}}|^2 \text{Re}(Z_{\text{Chip1}})/2} = \frac{4\text{Re}(Z_{\text{Ant}})\text{Re}(Z_{\text{Chip1}})}{|Z_{\text{Ant}} + Z_{\text{Chip1}}|^2}. \quad (2.13)$$

In Figure 2.6,  $r_{\text{Mismatch}}$  of this numeric example is drawn as a function of the antenna impedance. It is seen that the contour loops for constant  $r_{\text{Mismatch}}$  center around the complex conjugate chip impedance  $Z_{\text{Chip1}}^*$  where the matching condition is perfectly satisfied.

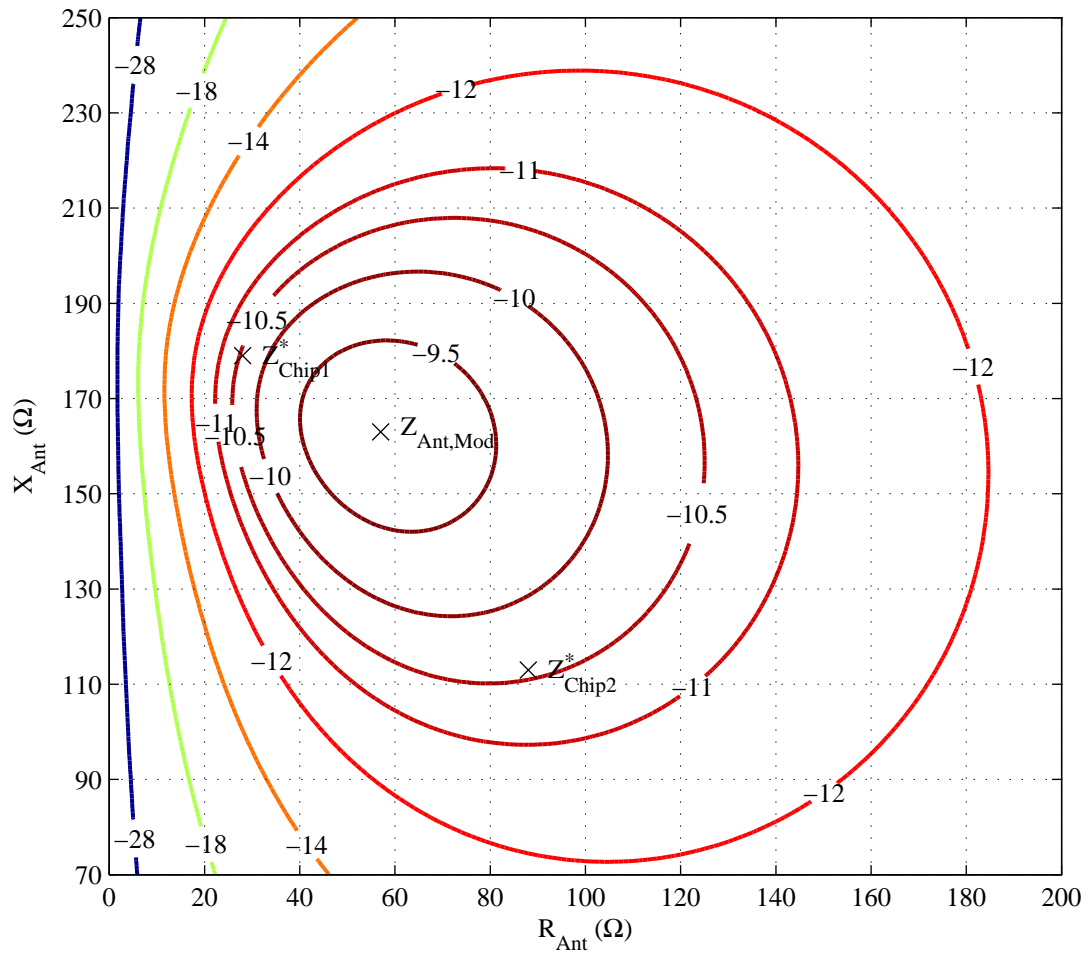


Figure 2.7: Modulation efficiency in dB versus antenna impedance.

### 2.4.3 Return link

When the transponder chip continuously switches between its impedance states a modulated signal is generated that is radiated by the transponder antenna. The power contained in the significant sidebands that are fed back into the antenna is  $P_{\text{DSB}}$  (Equation 2.10). It makes sense to define a modulation efficiency  $\eta_{\text{Mod}}$  that relates the available continuous wave power at the antenna output with  $P_{\text{DSB}}$  according to

$$\eta_{\text{Mod}} = \frac{P_{\text{DSB}}}{P_{\text{RX,Tag}}} = \frac{8}{\pi^2} \frac{\text{Re}(Z_{\text{Ant}})^2 \cdot |Z_{\text{Chip1}} - Z_{\text{Chip2}}|^2}{|Z_{\text{Ant}} + Z_{\text{Chip1}}|^2 \cdot |Z_{\text{Ant}} + Z_{\text{Chip2}}|^2}. \quad (2.14)$$

It is a measure for the total losses that are caused by modulation and relates two power levels that are contained in different frequencies.

For this example a plot of the modulation efficiency versus the antenna impedance is shown in Figure 2.7. It can be seen that best modulation efficiency is indeed achieved when the optimum antenna impedance  $Z_{\text{Ant,Mod}}$  is chosen ( $\eta_{\text{Mod,Max}} = -9.2$  dB). With this optimization criterion there comes a matching loss factor of  $r_{\text{Mismatch}} = 0.7$  dB at the rectifier input. If one would have chosen to go with power matching ( $Z_{\text{Ant,Pwr}} = Z_{\text{Chip1}}^*$ ) then the returned modulated signal would have been weaker by 1.2 dB ( $\eta_{\text{Mod}} = -10.4$  dB).

This does not seem very relevant in this particular example, and one would probably decide to build an antenna with an impedance somewhere between  $Z_{\text{Ant,Mod}}$  and  $Z_{\text{Chip1}}^*$ . However, I expect from future RFID chip developments that the two chip impedance states differ by far more than today. In particular, with a better shunt transistor that provides a resistance of  $10 \Omega$  when switched on,  $Z_{\text{Chip2}}$  is approaching a short circuit which will also entail a lower optimum antenna impedance  $Z_{\text{Ant,Mod}}$ . With such a shunt transistor an impedance in reflecting mode of  $Z_{\text{Chip2}} = (10 - 1j) \Omega$  could be achieved. Operation at any of the two optimum antenna impedances then entails a loss of some 4 dB in either modulation efficiency or matching. Furthermore, for such a transponder chip the maximum modulation efficiency is  $-2.6$  dB which would be an improvement of 6.6 dB compared with today's transponder chips.

## 2.5 Consequences for an RFID system

In the link budget  $\eta_{\text{Mod}}$  can be used to determine the total transmission coefficient  $a_{\text{Transm}}$  that includes the transmission coefficients  $|h_{\text{Forward}}|$  and  $|h_{\text{Return}}|$  for forward

and return link as well as the modulation efficiency  $\eta_{\text{Mod}}$  encountered at the transponder. The total transmission coefficient can be written as

$$a_{\text{Transm}} = |h_{\text{Forward}}|^2 \cdot \eta_{\text{Mod}} \cdot |h_{\text{Return}}|^2. \quad (2.15)$$

As described in Section 1.3.2 the transmission coefficients of the forward link and the return link can be considered equal.

The power transmission coefficient between the reader antenna input and the chip's rectifier (when in absorbing mode) is found as

$$a_{\text{Forward}} = |h_{\text{Forward}}|^2 \cdot r_{\text{Mismatch}}. \quad (2.16)$$

With the minimum operating power of the transponder chip  $P_{\text{Rect,Min}}$ , the transmit power  $P_{\text{TX,Reader}}$  necessary to operate the chip can be determined with  $a_{\text{Forward}}$ . On the other hand, with the interrogator's dynamic range  $d_{\text{Reader}}$  which denotes the ability to separate the returned sidebands from the transmitted continuous wave signal that is unintentionally leaking into the receiver,  $a_{\text{Transm}}$  can be used to calculate the maximum transmission loss allowed. Equivalently, the maximum read range for a return link limited system can be estimated.

Equations 2.15 and 2.16 are particularly interesting when designing an RFID system because they express whether the system will be forward link limited or return link limited. A sound forward link is thus provided if

$$P_{\text{Rect,Min}} \leq P_{\text{TX,Reader}} \cdot a_{\text{Forward}} \quad (2.17)$$

holds, and a sound return link is obtained if

$$d_{\text{Reader}} \geq \frac{1}{a_{\text{Transm}}} \quad (2.18)$$

is satisfied.

A very important finding contained in these considerations is, that waking up the transponder does not necessarily lead to its recognition. This is sometimes assumed in literature (e.g. [51]) but requires sufficient sensitivity of the interrogator device. Also, power returned by the transponder is often equated with the total reflected power at the chip input when in reflecting mode. This vastly overestimates the actual signal power returned in the relevant sidebands. As a consequence, a widely held belief is that RFID systems are mostly forward link limited. This is not true as was recently shown by measurement with commercially available equipment in [28]. Similar conclusions are drawn in [26]. I am convinced that with the dynamic range provided in today's interrogator units, passive RFID systems can be both forward or return link limited if the transponder antenna is subject to a proximity effect. The reason for this is that detuning of the transponder antenna has an impact on the antenna gain but also on the modulation efficiency. Both factors degrade the received power at the interrogator and require a higher dynamic range for detection.

# 3 A dual-band HF / UHF transponder antenna for RFID tags

Conventional RFID systems operating at one single carrier frequency can hardly handle the great variety of shapes and materials that occur in products and packaging. The project *Comprehensive Transponder System* accomplished by Infineon Technologies Austria AG tackles this problem by adding dual-band functionality to an RFID system. Operation in the HF band as well as in the UHF band provides two options to establish a data or energy link to each object equipped with a dual-band RFID tag. The project goal was to exploit the preferences of transmission at either of the two frequencies and to determine what the penalties of a dual-band system are in terms of performance in either band.

In this chapter the design of the dual-band transponder antenna is described. Section 3.1 gives an overview of the requirements for the antenna design that were defined with the project partners. In Section 3.2 the chosen antenna structures for the HF band and the UHF band are presented. Based on these structures a low-profile, electrically-small, and flexible antenna that operates at both frequency bands is developed. Section 3.2.4 discusses how the input impedance of the antenna can be adjusted to match a dual-band RFID chip at both frequencies. Simulation models for the antenna structure are presented and discussed in Section 3.3. In Section 3.4, the antenna performance in either band is verified by measurements on antenna prototypes that are matched to a dual-band RFID chip [52] developed by Infineon Technologies Austria AG. A summary of the achievements is given in Section 3.5.

## Original publications related to this chapter

L. W. Mayer and A. L. Scholtz, “A dual-band HF/UHF antenna for RFID tags,” in *Proc. 68th Vehicular Technology Conference*, (Calgary, Canada), Sep. 2008.

L. W. Mayer, “Dual-band antenna.” U.S. patent E0196.0139. applicant: Infineon Technologies Austria AG, filed May 7th, 2007.

## 3.1 Dual-band transponder antenna requirements

The general requirements for dual-band transponder antennas that are to be deployed in RFID systems were already discussed in Section 1.2.1 and Section 1.3.3. When designing a dual-band transponder antenna, some requirements desired at one frequency band may have a strong impact in the other band. One example is the large on-chip shunt capacitor that is used to tune an HF transponder coil to its resonant frequency. Such a capacitor will short circuit any currents at UHF and inhibit operation. It must not be implemented in a dual-band chip. Also the presence of the HF antenna coil which manifests itself similar to a closed loop at UHF rules out many antenna structures that are often found in conventional UHF transponders. In the following, some requirements that are a result of discussions with the project partners are given.

### 3.1.1 Electrical definition

The dual-band RFID system will conform to the ISO/IEC 15693 standard [1] at the HF band and to the ISO/IEC 18000-6-AMD1 standard [5] at the UHF band. These are the most economically relevant and also most established systems today. The center frequencies of the radio transmission modes are 866 MHz (UHF, European) and 13.56 MHz (HF). Functionality at both frequencies should be provided to a transponder chip that has one single port (two pins) serving both frequencies. This requirement is necessary to compete with existing systems in terms of cost. The antenna will be optimized to deliver the maximum power into the chip at both frequencies.

**UHF** At 866 MHz, antenna and chip can be matched by tuning and optimizing geometric parameters of the chosen antenna structure. Due to the on-chip bonding pad capacitance the input impedance of the chip is highly capacitive (see Section 2.1). Matching will thus be achieved by operating the antenna below its natural resonant frequency where it shows sufficiently inductive behavior. Furthermore, also the transponder chip will have dual-band capabilities which comes at the cost of performance—especially in the UHF band. This dual-band system will thus be forward link limited because of the increased operating power necessary to supply the chip. Consequently, in coherence with Section 2, complex conjugate matching of antenna and chip will be used instead of optimizing the antenna impedance for maximum modulation efficiency. For the proof-of-concept stage of this dual-band RFID system a transponder that fathoms the performance limits when operated in free space is of interest. As a consequence, the transponder antenna will be optimized for high antenna efficiency. It is well understood that

Table 3.1: Electrical specification of the UHF antenna.

parameter	specification
operating frequency	$f_{\text{UHF}} = 866 \text{ MHz}$
radiation pattern	approximately omnidirectional in one plane
gain and efficiency	to be optimized
bandwidth	robustness to proximity effects is not yet considered
polarization	linear
input impedance	matched to the transponder chip port impedance $Z_{\text{Chip1}}$

for electrically-small antennas there is a trade-off between antenna efficiency and bandwidth [17, 53, 54, 55]. Optimizing the antenna for maximum efficiency thus comes at the cost of bandwidth which would grant better robustness to detuning effects. However, once an efficient antenna is found, the trade-off can be readjusted to obtain more bandwidth by damping. Table 3.1 summarizes the electrical UHF antenna parameters.

**HF** Transponder antennas for RFID systems operating at 13.56 MHz are spiral antennas. These inductors are tuned to the desired resonant frequency by either an on-chip or an external capacitor. In conventional HF transponder coil designs some 4 to 6 coil turns that are located at the outermost of the available space are connected to a shunt capacitance of some 10 to 30 pF to set the resonant frequency. This meets a practical trade-off between open circuit voltage at the chip input on the one hand and robustness to proximity effects on the other hand. Further robustness to proximity effects is gained by selecting a higher-than-needed resonant frequency.

For tuning this dual-band antenna a shunt capacitor can not be applied because it would short circuit signals at UHF. As a consequence the HF antenna has to be resonant on its own. This might be achieved by thoughtfully arranged concentrated capacitors or by a distributed capacitance that is caused by very closely spaced turns of the HF coil. The latter will entail a very narrow isolation gap between the coil turns and thus lead to difficulties in production—especially if a low-cost production process is used. The use of lumped circuit elements like tuning capacitors or inductors are ruled out because of cost constraints also. A possible solution is the use of substrate capacitors that consist of metallizations on a very thin dielectric layer. Finding a way to utilize such capacitors for making the coil resonant on its own while not inhibiting UHF performance will need some thought. Table 3.2 shows the required parameters of the HF coil antenna.

Table 3.2: Electrical specification of the HF antenna.

parameter	specification
resonant frequency	$f_{\text{HF}} = 13.56 \text{ MHz} \dots 14 \text{ MHz}$ when connected to the chip
quality factor	$Q_{\text{HF}} \approx 40$
bandwidth	$B = f_{\text{HF}}/Q_{\text{HF}} \approx 340 \text{ kHz}$

### 3.1.2 Environmental definition

In product identification the diversity of materials that may be present in the proximity of the transponder antenna is not seizable. There might be very lossy materials like fruit juice but also perfectly conducting materials like an aluminum beverage can. For the proof of concept these issues are considered important but can not be treated in detail. The chosen approach is to design an antenna that perfectly interacts with the transponder chip when positioned in free space. The influence of materials situated in the proximity of the transponder are to be investigated at a later point of time.

The size of the transponder is given by one of its intended applications as a vicinity card<sup>1</sup> according to ISO/IEC 7810, ID-1 [56]. With this standard there come some more mechanical requirements and also a thermal operating range. Substrate materials with metal structures on both sides are widely used for many HF transponders and also for some UHF transponders today. Since the usage of substrate capacitors is considered necessary the dual-band antenna design will be based on such a substrate. A preferably thin laminate is favored to achieve high capacitance per area and to maintain mechanical flexibility of the transponder antenna. This will also allow manufacturing of the transponder as sticker or reeled tape. The environmental definition parameters that were worked out together with the industrial project partners are summarized in Table 3.3. They supplement the general mechanical specifications given in the ISO/IEC 15693 [1] and the ISO/IEC 7813 [57] standard.

---

<sup>1</sup>Vicinity cards are transponders in form of a credit card sized plastic enclosure.

Table 3.3: Environmental specification of the tag antenna.

parameter	specification
size	maximum antenna size: $85.6 \times 54 \times 0.76 \text{ mm}^3$
mechanical	Production of the antenna as sticker or reeled tape should be possible. Maximum deflections about the long and short cards axes are $h_w A = 20 \text{ mm}$ and $h_w B = 10 \text{ mm}$ , maximum torsion angle is $\alpha = 15^\circ$ .
thermal operating range	0 to $50^\circ\text{C}$
conducting material	Double sided etched copper for prototype design and possibly printed conductive ink for mass production.
substrate material	dielectric film
proximity of antenna	Antenna design for operation in free space.

## 3.2 Antenna design

This section describes the two antenna structures serving the HF and the UHF frequency bands. Furthermore, it is explained how the two antennas are combined into one dual-band antenna.

### 3.2.1 HF antenna

In the 13.56 MHz band, a printed spiral antenna is used. The alternating magnetic field excited by the reader penetrates the spiral in an arbitrary angle. The part of the magnetic flux that is aligned perpendicular to the spiral plane induces a voltage in the winding. According to the law of induction, the voltage can be increased by enlarging the diameter of the winding in order to collect more magnetic flux. It is therefore important that the HF antenna coil is placed at the outermost region of the available space.

The quality factor  $Q_{\text{HF}}$  of the HF antenna is determined by the resistive losses in the antenna coil.  $Q_{\text{HF}}$  is a measure for the voltage and current step-up at the antenna output. The quality factor is related to the antenna's center frequency  $f_{0,\text{HF}}$  and 3 dB bandwidth  $B_{\text{HF}}$  according to  $Q_{\text{HF}} = f_{0,\text{HF}}/B_{\text{HF}}$ . This makes the quality factor available for measurement. The resonant frequency is determined by the total inductance and the total capacitance of the printed spiral.

It is important to point out that conventional single-band HF transponders usually feature an essentially inductive antenna that is tuned to the desired resonant frequency by a capacitor ( $\approx 25$  pF) that is integrated into the transponder chip. For a combined HF and UHF transponder chip with one single port, such a capacitor would present a short circuit at the chip input for UHF and thus inhibit operation. Here it is essential to minimize the input capacitance of the chip like in a pure UHF design (today, typical UHF chip input capacitances are in the range of a few 100 fF to 1 pF). As a consequence, the HF antenna coil cannot be tuned by a chip capacitance, but rather has to be resonant on its own. This is achieved by the substrate capacitors C1, C2, and C3 (see bottom drawing of Figure 3.1 and a detailed explanation in Section 3.3.2) that create a parallel resonance with the coil at approximately 13.56 MHz.

### 3.2.2 UHF antenna

The challenge of the comprehensive antenna design was to find a UHF antenna shape that

- has minimal mutual interaction with the HF coil antenna
- and can be combined with the HF coil antenna consuming as little additional space as possible.

The shorted loop slot antenna [58, 59] was found to best fit these requirements because it is electrically small and features a closed ground plane at its circumference. The closed ground plane allows to place the HF coil around the shorted loop slot antenna. Since the conducting strips of the coil run in parallel to the outer edge of the ground plane, performance of the loop slot antenna is weakly impaired. The structure (not to scale) of a shorted loop slot antenna is shown in the top drawing of Figure 3.1.

The main design parameter of the shorted loop slot antenna is the length of the slot-line resonator, which is folded into a rectangle. The length determines the self resonant frequency  $f_{0,\text{UHF}}$  of the antenna. A standing wave can be excited in the resonator by applying electric energy somewhere along the slot-line. The position of this feed with respect to the ends of the slot-line determines the feed point impedance. The highest input impedance is achieved by placing the feed point into the center of the resonator. Moving the feed point closer to either of the resonator ends (closer to the short) yields lower input impedance. The input impedance of the antenna also depends on the slot width—where a narrow slot causes smaller input impedance and also higher losses in the resonator. Radiation is mainly caused by the strong electric current present in the short.

### 3.2.3 Combining the antennas

To reduce HF eddy currents in the UHF antenna elements, the big metal area surrounded by the loop slot has to be removed. This leads to a modified version of the shorted loop slot antenna consisting of two rings. Induced HF currents in the rings push the magnetic field to the outside. This reduces the magnetic flux collected by the HF coil and consequently impairs its quality factor. To remove the closed loops a narrow gap is inserted into each of the loop slot antenna rings. This makes the UHF antenna compatible with the HF antenna. The modified antenna with the cutout and the gaps is shown in the middle drawing of Figure 3.1.

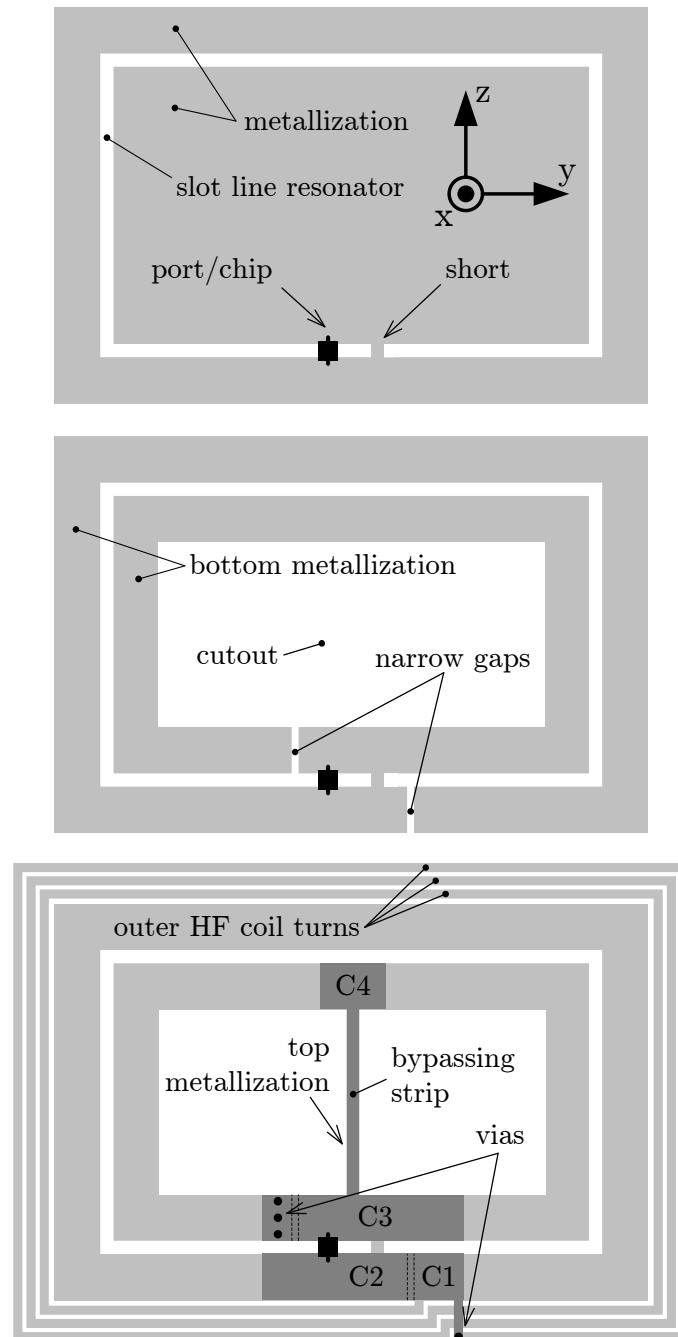


Figure 3.1: Antenna evolution

Top: Generic shorted loop slot antenna.

Middle: Modified antenna with center cutout and narrow gaps to reduce eddy currents.

Bottom: Dual-band antenna with outer HF coil, top metallization, and substrate capacitors (C1 C2 C3) bridging the gaps for UHF currents. The bypassing strip and the capacitor C4 conduct surface currents former present in the cutout area.

For UHF each gap is bypassed by a conducting strip formed by the top metallization. The substrate capacitors C1, C2, and C3 bridging the gaps are chosen to sufficiently conduct UHF currents, while only weakly conducting currents at HF. This allows a *reuse* of the UHF antenna rings as two inner turns of the HF coil antenna. Furthermore, the substrate capacitor C2 ( $\simeq 55$  pF) is used to adjust the coil antenna to its center frequency. Fine-tuning is done by proper choice of C1 and C3.

Finally, a bypassing strip is introduced to conduct the UHF surface currents former present in the cutout. This strip consists of top metallization and is connected to the inner ring by the substrate capacitors C3 and C4. Simulations with Ansoft HFSS v11 [60] showed that such an arrangement well preserves the characteristics of the shorted loop slot antenna.

The shape of the HF antenna coil differs from standard geometries treated in literature because of:

- two wider innermost turns,
- a wider gap between those two turns, and the
- substrate capacitors C1 to C4.

With the procedure described in [12], the inductance of the coil at HF was determined. Based on this result, the capacitors that tune the HF antenna on the one hand and conduct UHF currents on the other hand were calculated. The resulting capacitor values are some 10 pF to 60 pF. Given the area available for the substrate capacitors, a very thin dielectric substrate has to be used. For the prototypes presented in this work, a  $25 \mu\text{m}$  polyimide substrate (relative dielectric constant  $\epsilon_r = 3.1$ , loss-tangent  $\tan(\delta) = 0.007$ ) with double sided  $18 \mu\text{m}$  copper cladding [61] was used and processed in house by a standard PCB manufacturing process.

The final antenna structure can be seen in the bottom drawing of Figure 3.1. Please note that for UHF the metallizations on top and bottom of the substrate are well connected by substrate capacitors. Except for the outer HF coil turns and the cutout that is replaced by the bypassing strip, there is no significant electrical difference to the generic shorted loop slot antenna shown in the top drawing of Figure 3.1. Conversely, at HF, currents between top and bottom metallizations are conducted by vias. This allows integration of the HF antenna into the shorted loop slot antenna by sharing the two inner rings. To summarize, the path of the HF current  $i_{\text{HF}}$  through the dual-band antenna is shown in Figure 3.2.

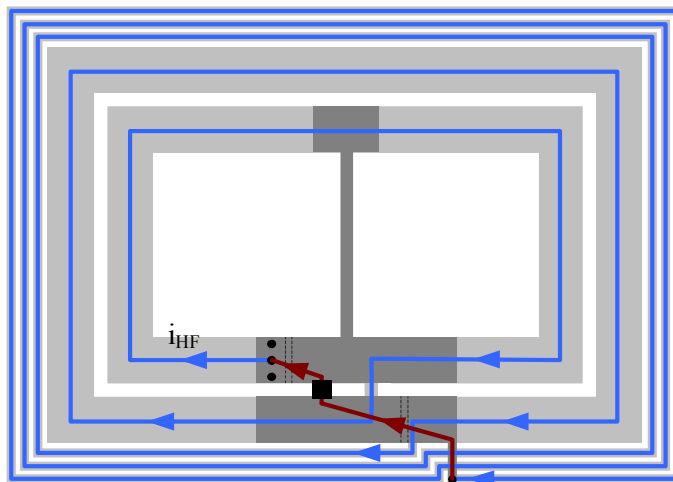


Figure 3.2: Path of the HF current  $i_{\text{HF}}$  through the dual-band antenna. Current on the top metallization is shown in red, current on the bottom metallization is shown in blue. The transponder chip is mounted on top of the substrate.

### 3.2.4 Antenna tuning

The comprehensive RFID tag antenna has to be optimized when integrated into packaging, designated to an RFID chip, and assigned to a certain field of operation. In detail, the unknowns are

- material parameters of the antenna cladding (cardboard, plastic, paper, adhesive tape, ...),
- transponder chip parameters like input resistance, input capacitance, maximum input voltage, chip size, bonding / gluing techniques, and
- required bandwidth to gain robustness to detuning effects in multiple tag scenarios and in proximity of products and materials.

The following paragraphs discuss the effects of the design parameters that are available for antenna optimization.

**HF** Detuning effects and the chip input capacitance lower the center frequency of an HF tag antenna. This impairs the performance, especially when the antenna has small bandwidth, or equivalently, high quality factor. More reliable operation of an RFID tag can be achieved by choosing a center frequency slightly above 13.56 MHz and a quality factor of  $Q_{\text{HF}} \simeq 40$ . These values provide sufficiently high output voltage and practical robustness to detuning effects.

The center frequency can be coarsely adjusted by the number of outer turns and fine tuned by the substrate capacitors. A decrease in capacitance is achieved by shortening the top metallizations along the UHF antenna rings. This reduces the capacitance of C2, C1 and C3 and consequently increases the center frequency of the HF antenna. The quality factor of the HF antenna can be deliberately decreased by choosing smaller conductor width of the outer turns. A reduction of the quality factor leads to a wider frequency bandwidth.

**UHF** Matching to RFID chips, that typically show small input resistance and strongly capacitive behavior, can be achieved by choosing the self resonant frequency  $f_{0,\text{UHF}}$  of the antenna higher than the desired operating frequency. The antenna then shows inductive behavior and small input resistance. The ratio of input reactance and input resistance is set by the frequency offset. For transponder chips, typical ratios of  $-\text{Im}\{Z_{\text{Chip1}}\}/\text{Re}\{Z_{\text{Chip1}}\}$  range from 4 (packaged chip prototypes supplied by Infineon) to 34 (Atmel ATA5590 [62]). For testing with currently developed Infineon chips, a ratio of 4 was chosen for the first antenna prototypes. Scaling the real and imaginary part of the input impedance can be done by choosing the distance between the feeding point (or equivalently speaking the chip position) and the short circuit.

Addressing most general results, the comprehensive antenna was optimized to best operate in free space. Prototypes with a resonator circumference of 171.8 mm and a distance of 10 mm between the feed point and the short were built. The dimensions of the final antenna are  $71 \times 46 \text{ mm}^2$ . Compared to the dual-frequency RFID antenna described in [63] an area reduction by a factor of 4 is achieved.

### 3.2.5 Dual-band antenna with HF coil on the inside

The dual-band antenna described in Section 3.2 was optimized for best performance in the HF band. This Section describes modifications that may improve the antenna performance in the UHF band. It was argued in Section 3.2.3 that when combining the two antenna structures, UHF performance is degraded by the additional coil turns along the dual-band antenna's circumference. It is expected that losses that come with induced currents in the HF coil conductors reduce the efficiency of the UHF antenna. For this new prototype, the HF coil winding is put to the inside of the loop slot antenna. It is hypothesized that the HF coil turns will interfere less with the electromagnetic field produced by the loop slot antenna when put inside the cutout area. Figure 3.3 depicts the two antenna variants. The original variant with the HF coil on the outside is labeled CTS28, the new antenna is called CTS35. Please note that this modification reduces the required area by 28%.

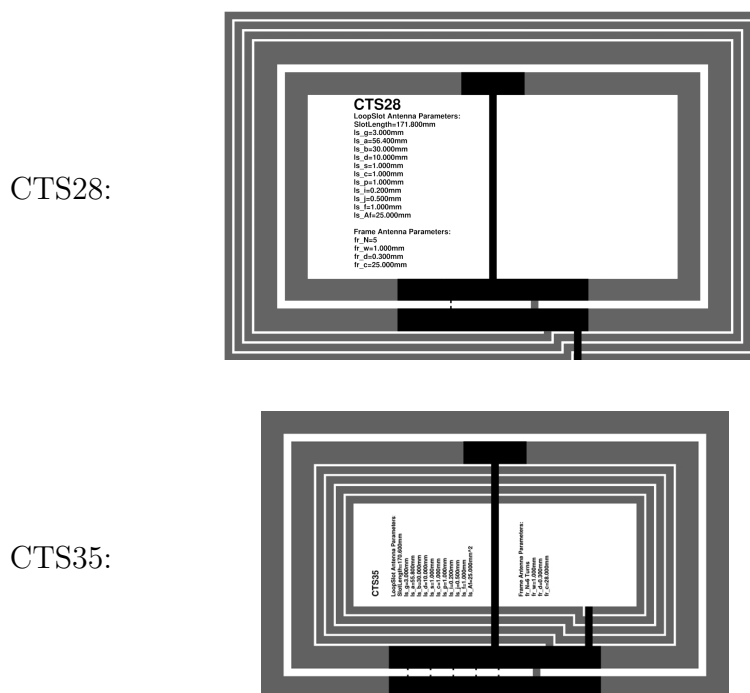


Figure 3.3: Layouts of the prototype antenna variants (actual size). The top and bottom metallization are shown in black and gray, respectively.

It is obvious that the area surrounded by the HF coil winding is significantly smaller when the outer coil turns are moved to the inside of the loop slot antenna. This causes a lower inductance for the entire winding. To compensate for that, one more turn was added to the HF coil. The new prototype now has four turns in the inner winding plus two turns which result from re-using the loop slot antenna. Like in the original prototype, adjustment of the HF coil resonant frequency can be done by tuning the substrate capacitors C1, C2, and C3.

### 3.3 Antenna simulation

This section deals with the simulation of the dual-band antenna in the UHF band. Simulations were used to determine the effects of some structural parameters on the input impedance and radiation behavior of the antenna. Especially the characteristics of the folded loop slot resonator are hard to determine analytically but are fathomed relatively easy by simulation. Therefore, a field simulation software (HFSS v11 [60]) using a full-wave finite element method (FEM) was chosen.

### 3.3.1 Full model

The dual-band antenna consists of the very thin ( $25\ \mu\text{m}$ ) polyimide substrate which represents the smallest dimension of the structure. The overall antenna size is in the range of 70 mm. To investigate radiation from the antenna, a field solution has to be obtained on a surface surrounding the antenna at a distance of approximately a quarter wavelength. The diameter of that airbox is thus some 250 mm. The ratio of the biggest and smallest dimension that is contained in the structure that is to be simulated is directly related to the complexity of the mesh and thus affects the complexity of the numeric solution finding in terms of memory and computing power. For this antenna problem, a ratio of approximately  $10^4$  is obtained. Some test runs showed that the amount of computing power and memory of an up-to-date workstation was not sufficient at the time of writing. Therefore, a simplified planar model of the antenna not containing the thin substrate was developed and is presented in Section 3.3.2.

### 3.3.2 Simplified planar model

To enable simulation with reasonable amount of computing power, a planar model of the dual-band antenna was developed that accounts for the effects of the thin substrate. In fact, since the substrate thickness is very small compared to the free space wavelength, surface currents—no matter if flowing on top or bottom metallization—will have the same effect on the radiation caused by the antenna.

The first effect that is necessary to consider for simulation is the transition of currents between the top and bottom metallization through electric displacement currents in the substrate capacitors. In this approach the distributed substrate capacitors (C1 to C4) are modeled as equivalent lumped capacitors. Since the lateral dimensions of the substrate capacitors are still small compared to the wavelength, this approach is reasonable. Figure 3.4 shows the simulation model with the equivalent capacitors that are included in the computation.

For simulation the top metallizations that are bridging the narrow gaps are omitted. The remaining gaps that cut across the inner and outer ring of the loop slot antenna are replaced with lumped capacitor boundary elements that account for the missing substrate capacitors. The value for the inner gap capacitor is equivalent to that of C3. For the outer gap capacitor the capacitance of the series connection of C1 and C2 is chosen. The value of the bypassing strip capacitor is set equal to C4. The HF bridge that connects the outermost turn of the HF coil is modeled as a conducting band that runs 1 mm above the antenna plane. The substrate capacitors that were originally formed by the intersections of the HF bridge with the HF coil turns are also modeled and called bridge capacitors. Table 3.4 gives

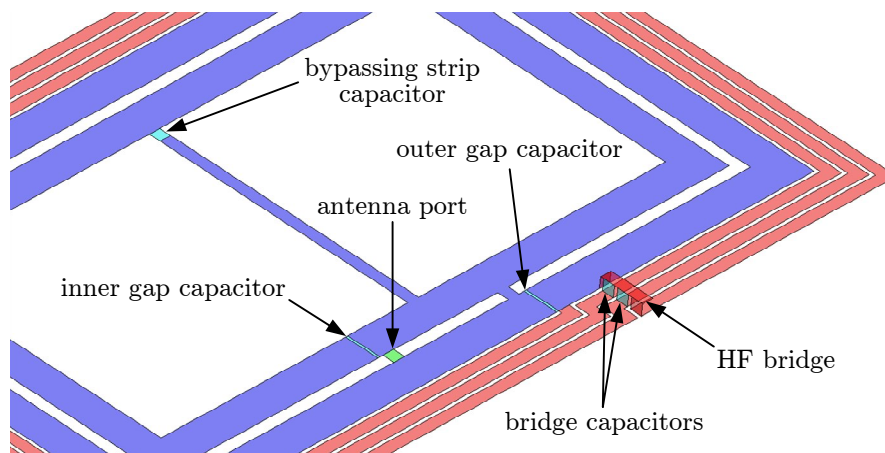


Figure 3.4: Planar simulation model showing the lumped capacitors.

Table 3.4: Lumped capacitors used to model the effects of the distributed substrate capacitors in the CTS28 antenna variant.

modeled capacitor	equivalent to	value
inner gap capacitor	C3	58.97 pF
outer gap capacitor	C1 in series to C2	14.98 pF
bypassing strip capacitor	C4	26.56 pF
bridge capacitors	HF bridge intersections	1.06 pF

an overview of the capacitors used in the simulation model for the CTS28 antenna variant.

Second, the antenna metal is modeled as a finite conductivity boundary. This boundary can be used if the thickness of the conductors is much larger than the skin depth. With a copper layer thickness of  $18 \mu\text{m}$  and a skin depth of  $2.2 \mu\text{m}$  this is considered satisfied. Therewith, a surface boundary condition can be used in HFSS v11 and fields do not have to be solved inside the conductor. Furthermore, the thin copper cladding can be modeled as a two dimensional structure instead of a volume which again simplifies the model.

Table 3.5: Simulated and measured input impedance values for CTS28.

obtained by	accuracy level	value
simulation	low	$Z_{\text{Ant,Sim}} = (32.2 + 158.6j) \Omega$
direct reflection measurement	low	$Z_{\text{Ant,Refl}} = (58.8 + 211.4j) \Omega$
source-pull measurement	high	$Z_{\text{Ant,LoadPull}} = (66.4 + 176.4j) \Omega$

The third aspect of the planar model is the missing substrate in the resonator slot. It is hypothesized that if

- the thickness of the antenna substrate is very small compared to the slot width ( $1 \text{ mm}/25 \mu\text{m} = 40$ ) and if
- the permittivity of the substrate is relatively low ( $\epsilon_r = 3.1$ )

the influence of the dielectric layer can be neglected. If this hypothesis does not hold, then the speed of wave propagation is overestimated which leads to a higher simulation result for the natural resonant frequency of the loop slot antenna.

Exemplary simulation results for the CTS28 antenna variant are presented with the measurement results in Section 3.4.2. Indeed, it is seen in Figure 3.6 that the measured natural resonant frequency of the antenna is lower by approximately 0.5% in comparison to the simulated result. This disproves the hypothesis and shows that the simulations will only reveal approximate results when optimizing the input impedance of the antenna. Table 3.5 summarizes the simulated and measured results for the input impedance at 866 MHz. However, the gain figures obtained by simulation agree very well with the measurement results discussed in Section 3.4.3. A comparison is shown in Figure 3.10. Please note that for both, the simulation and the measurement perfect matching of the antenna is provided. The actual input impedance of the antenna thus does not affect the gain and efficiency figures of the antenna.

## 3.4 Measurements

### 3.4.1 HF measurements

Antenna characteristics in the HF band were determined in a transmission experiment. The dual-band antenna was positioned coaxially to a wide-band test antenna

(16 turns, coil diameter 67.5 mm) at a distance of 30 mm. The open circuit voltage at the tag antenna terminal was measured to determine the self resonant frequency  $f_{0,\text{HF}}$  and the quality factor  $Q_{\text{HF}}$ . A 3.3 pF capacitor was inserted between the antenna and the measurement cable to minimize influence of cable capacitance and measurement equipment. A self resonant frequency of  $f_{0,\text{HF}} = 13.49$  MHz and a maximum quality factor of  $Q_{\text{HF}} = 54.1$  was determined. This shows that an HF performance as good as that of single-band HF antennas can be achieved. Tuning the quality factor to the optimum of  $Q_{\text{HF}} = 40$  can be achieved by reducing the conductor width of the outer HF antenna coil turns. The resonant frequency can be adjusted by changing the length of the conducting strips formed by the top metallization or—equivalently speaking—changing the capacitance of C1, C2, and C3. An input impedance measurement with a vector network analyzer was additionally performed to verify the results from the quality factor measurement (Figure 3.5). Also, from that measurement the equivalent parallel resonant circuit elements  $R_{\text{Par}}$ ,  $L_{\text{Par}}$ , and  $C_{\text{Par}}$  of the antenna coil were determined by curve fitting. The results are summarized in Table 3.6.

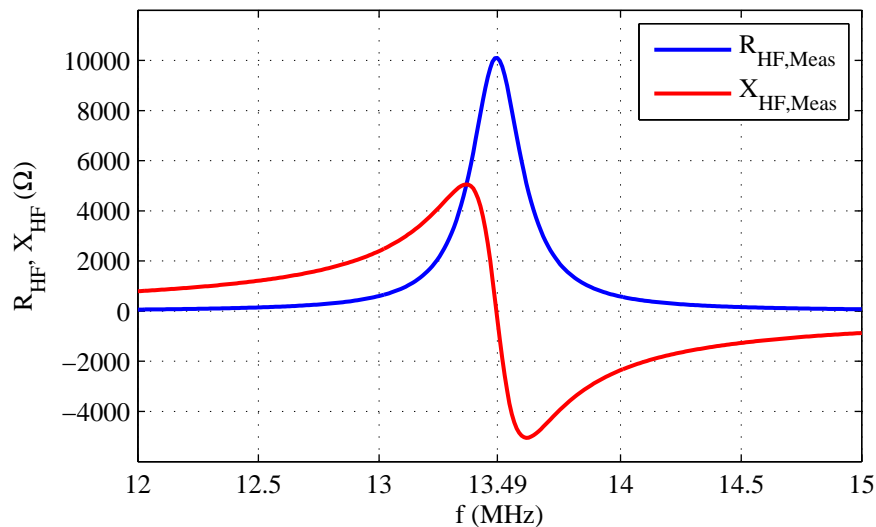


Figure 3.5: HF: Real and imaginary part of measured antenna input impedance versus frequency.

### 3.4.2 UHF impedance measurements

A preliminary impedance measurement in the UHF band was performed by means of a vector network analyzer. The antenna was therefore directly connected to the

Table 3.6: Characteristics of the HF coil winding.

coil property	symbol	value
equivalent parallel resistance	$R_{\text{Par}}$	$= 10.1 \text{ k}\Omega$
equivalent parallel inductance	$L_{\text{Par}}$	$= 2.2 \mu\text{H}$
equivalent parallel capacitance	$C_{\text{Par}}$	$= 63.1 \text{ pF}$
center frequency	$f_{0,\text{HF}}$	$= 13.49 \text{ MHz}$
quality factor	$Q_{\text{HF}}$	$= 54.1$

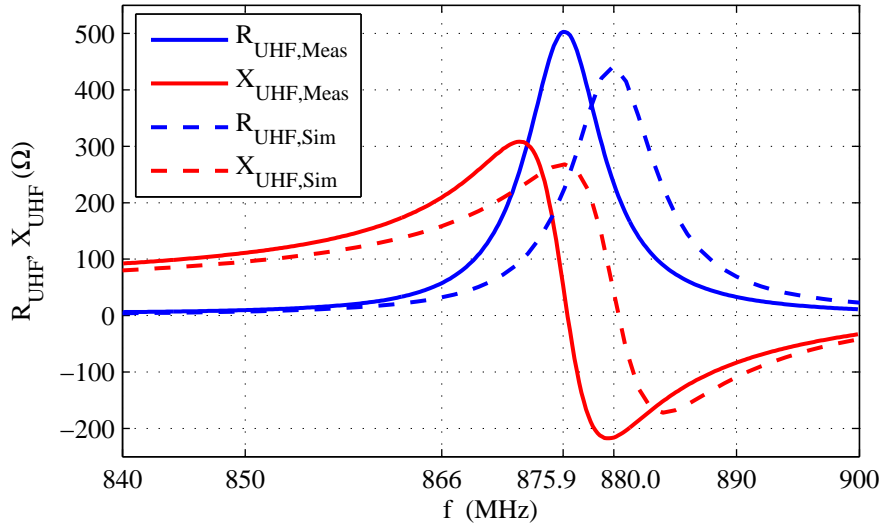


Figure 3.6: UHF: Real and imaginary part of measured and simulated antenna input impedance versus frequency.

measurement device via a thin coaxial cable. The author is aware that such a measurement will not give accurate measurement results because of interference of the radiating field with the measurement cable. However, the results show the principal characteristics of the input impedance versus frequency.

For this impedance measurement, the shield and the center conductor of the coaxial measurement cable were soldered to the outer and inner ring of the antenna, respectively. The measurement cable extends along the antenna plane to minimize proximity effects. The electrical length of the measurement cable is deembedded during the calibration process. Figure 3.6 shows real and imaginary part of the input impedance  $Z_{\text{UHF}}$  versus frequency.

For the CTS28 antenna variant a self resonant frequency of  $f_{0,\text{UHF}} = 875.9 \text{ MHz}$  was achieved by a resonator circumference of 171.8 mm. It is also seen from Fig-

ure 3.6 that for frequencies below  $f_{0,\text{UHF}}$ , the input reactance  $\text{Im}(Z_{\text{UHF}})$  shows inductive behavior and the input resistance  $\text{Re}(Z_{\text{UHF}})$  decreases as discussed in Section 3.2.4.

A more accurate input impedance measurement at a single frequency was performed in the course of the gain measurement procedure [64]. The impedance is obtained by a load-pull measurement with a small, battery-powered oscillator that is equipped with a tunable matching network. A detailed description of this new method can be found in Section 5. The input impedance of the CTS28 dual-band antenna determined in this way is  $Z_{\text{Ant}} = (66 + 176j) \Omega$ . It was shown by experiments that this antenna matches its designated transponder chip prototype that was produced and packaged by Infineon very well. An improvement of power delivered into the chip could neither be achieved by moving the transponder chip away from its optimum position along the slot-line resonator, nor by readjusting the frequency—which is equivalent to resizing the slot-line resonator length.

### 3.4.3 UHF gain measurements

In this section, measurement results for three versions of the dual-band antenna are presented and compared to a generic single-band loop slot antenna (CTS29) that uses up a comparable amount of space. A precision dipole antenna is used as a reference in the measurement procedure. From the measurement results conclusions are drawn for the performance penalties of the dual-band design. The characterized prototypes are a

- loop slot antenna with all modifications done for the dual-band antenna, but without the HF coil winding (CTS27), a
- dual-band antenna variant with the HF coil at the circumference of the available space (CTS28), and a
- dual-band antenna variant with the HF coil inside the cutout of the loop slot antenna (CTS35).

All antennas are characterized with a new gain measurement procedure that was specifically developed for the measurement of small and low gain antennas (Chapter 5). With this method gain can be measured as a function of the polar and the azimuth angle. From the results the antenna efficiency is computed by integration of the measured gain with respect to the surface of a sphere (see Section 5.1).

A cable that connects the antenna with the measurement equipment introduces the following disadvantages when characterizing an RFID tag antenna:



Figure 3.7: Dual-band tag antenna prototype with battery driven oscillator (actual size).

- Currents induced along the shield of the measurement cable will corrupt the measurement of directional pattern and of the input impedance. In particular, these currents will seriously impair the measurement results for small, and low-directivity antennas.
- A measurement cable complicates antenna pointing when 3D radiation patterns are to be determined.

To avoid these drawbacks, gain measurements were performed with a miniaturized, battery-driven, crystal-stabilized oscillator that generates a sinusoidal transmit signal directly at the antenna. A tunable matching network built into the oscillator unit provides a source impedance equal to the complex conjugate input impedance of the antenna. Prior to the characterization of each antenna variant, this matching network was tuned to deliver all the available oscillator power to the antenna. This was done by adjusting two capacitors included in the oscillator's matching network with a ceramic tuning tool. Optimum matching was achieved by maximizing the radiated power that was measured with a pickup antenna. After each gain measurement the available oscillator power was determined by using the measurement procedure described in Section 5.5. Figure 3.7 shows the dual-band antenna with the battery driven oscillator. For characterization the antenna was clamped into a polystyrol foam test fixture.

A precision, low-loss half-wavelength dipole that was fed by an identical oscillator was used as a reference antenna. From the results for the dipole, the measurement setup was calibrated to obtain a dipole efficiency of 100%. Gain figures were then determined by comparing all other antenna prototypes with the results for the dipole. A more detailed description of the gain measurement method can be found in Section 5.6.

At first, the antenna version without the extra HF coil turns (CTS27) was characterized. A maximum gain of  $-1.98$  dBi (gain compared to the isotropical radiator) was determined for this variant. Compared to the well optimized single-band shorted loop slot antenna with a measured gain of  $0.02$  dBi, a gain reduction of  $2$  dB is encountered. The reason for this is that the focus of the dual-band antenna design was put on the HF antenna performance. The gain reduction is explained as follows:

- The small slot width ( $1$  mm) leads to high surface currents along the edges of the slot line resonator and thus to increased losses. A widened slot is not favored because it would increase the overall size of the antenna and decrease the area covered by the innermost winding of the HF coil antenna.
- Confinement of the ground plane ( $3$  mm for CTS27 compared to  $6.9$  mm for CTS29) reduces the directivity of the antenna and causes a more omnidirectional radiation pattern which has an impact on the maximum gain.
- Removing the metal area in the center of the bottom metallization and replacing it with a bypassing strip concentrates the surface current into a small cross-section which also increases losses.

At this point it is obvious that—in comparison to a generic shorted loop slot antenna—some of the gain reduction can be recovered at the cost of overall antenna size and HF performance by widening the slot width, increasing the ground plane size, and introducing more than one bypassing strips. Whether this is practical or not depends on the requirements that are defined by the application.

The characterization of the dual-band antenna with the HF coil turns around the loop slot antenna (CTS28) revealed a maximum tag antenna gain at UHF of  $-4.75$  dBi. Obviously, induced currents in the outer HF winding cause an additional loss of UHF performance by approximately  $2.8$  dB. The last variant of the dual-band antenna with the HF coil turns on the inside of the loop slot antenna (CTS35) shows slightly different gain figures, but identical efficiency when compared to CTS28. The hypothesis that losses in the coil can be reduced by moving the HF coil turns to the inside of the cutout is thus disproved. A possible reason is that one more HF coil turn is necessary to maintain the resonant frequency at HF, and that losses caused by induced currents in this additional turn compensate the expected improvement. However, the required area of the last antenna variant is reduced by  $24\%$  in comparison to CTS28. It is also seen that CTS35 tends to radiate a more pure vertical polarization. The cross polarization ratio of CTS35 is higher by  $6$  dB.

The measured gain patterns for horizontal and vertical polarization (compared to the isotropic radiator) of all antennas are given in Figure 3.8, Figure 3.9, Fig-

ure 3.10, and Figure 3.11. For reference, the gain pattern of the dipole is shown in Figure 3.12. Additionally, in Figure 3.10, the simulated gain of CTS28 is given.

Table 3.7 compiles the measurement results of the reference dipole and the selected antenna variants. All gain figures relate to gain compared to an ideal isotropic radiator. They are normalized to the power accepted by the antenna, which is a direct result of the perfect matching of the antenna with its test signal source. The antenna efficiency relates to the ratio between radiated and accepted power. It is also a property of the antenna only and does not consider the matching situation. The cross polarization ratio is computed as the total power radiated in vertical polarization divided by the total power radiated in horizontal polarization.

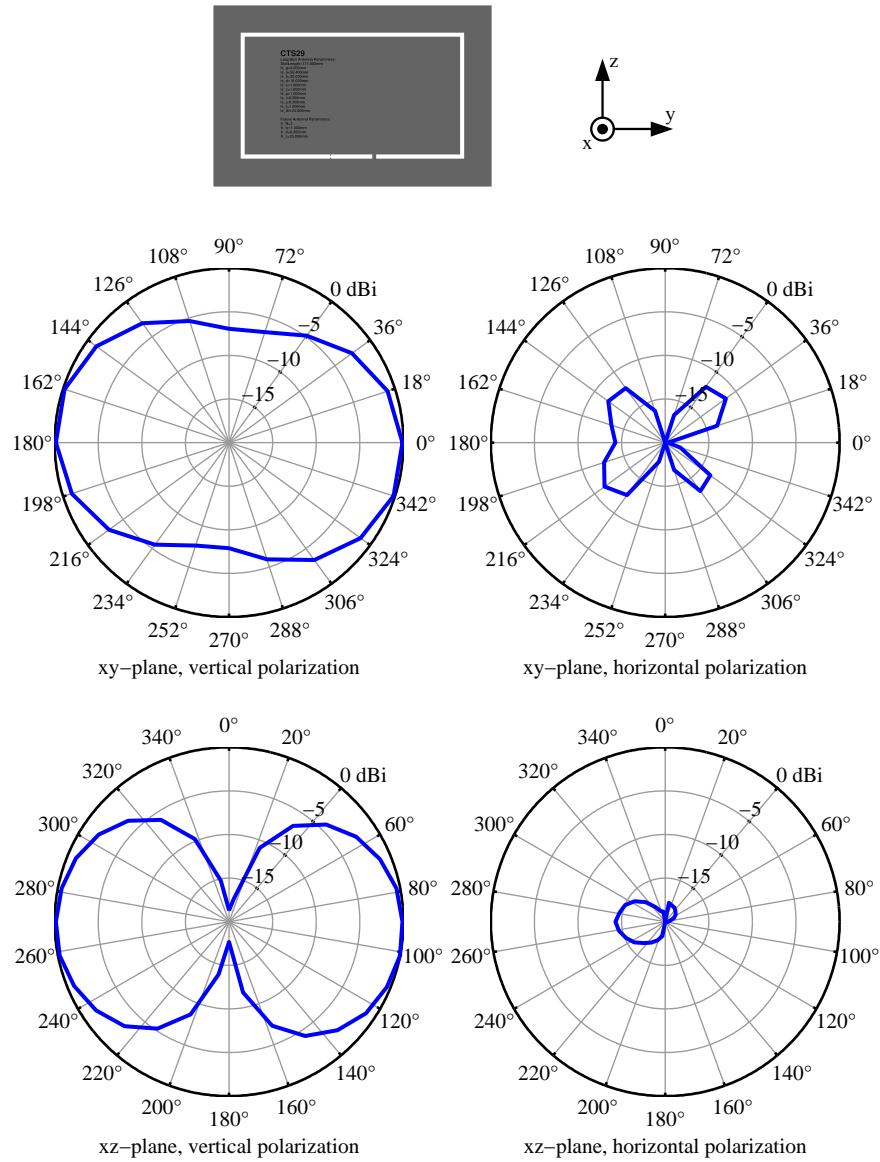


Figure 3.8: Measured gain of the single-band loop slot antenna CTS29 in horizontal and vertical polarization at UHF. The upper plots show the gain in the xy-plane with respect to the azimuth angle starting at the x-axis. The xz-plane plots are drawn versus the polar angle starting at the z-axis (see Figure 3.1).

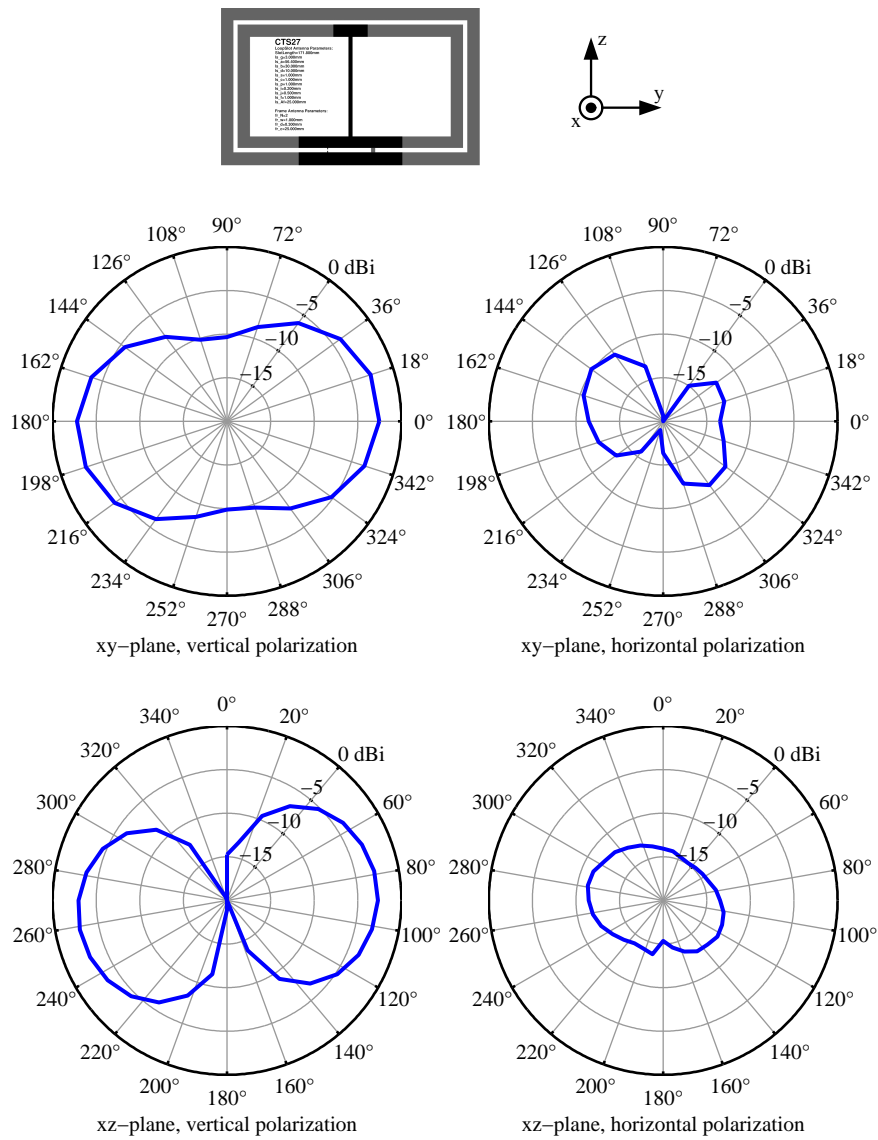


Figure 3.9: Measured gain of the dual-band antenna with HF winding removed (CTS27) in horizontal and vertical polarization.

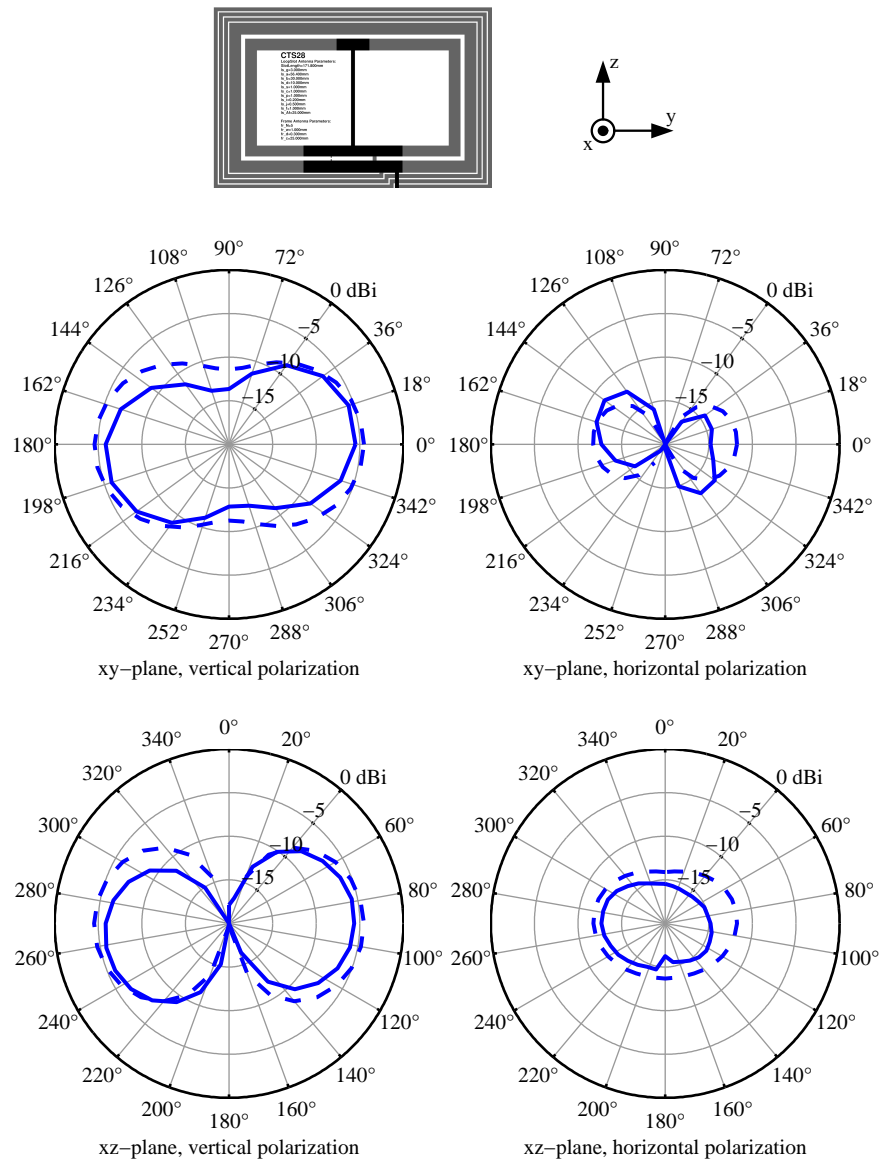


Figure 3.10: Measured and simulated gain of the dual-band antenna with HF winding outside (CTS28) in horizontal and vertical polarization. The dashed line represents the simulation result. Apart from a tilt of some few degrees that is caused by imperfect orientation of the antenna in the rotation unit, the measured and simulated results for the gain pattern agree with an accuracy of approximately 1 dB.

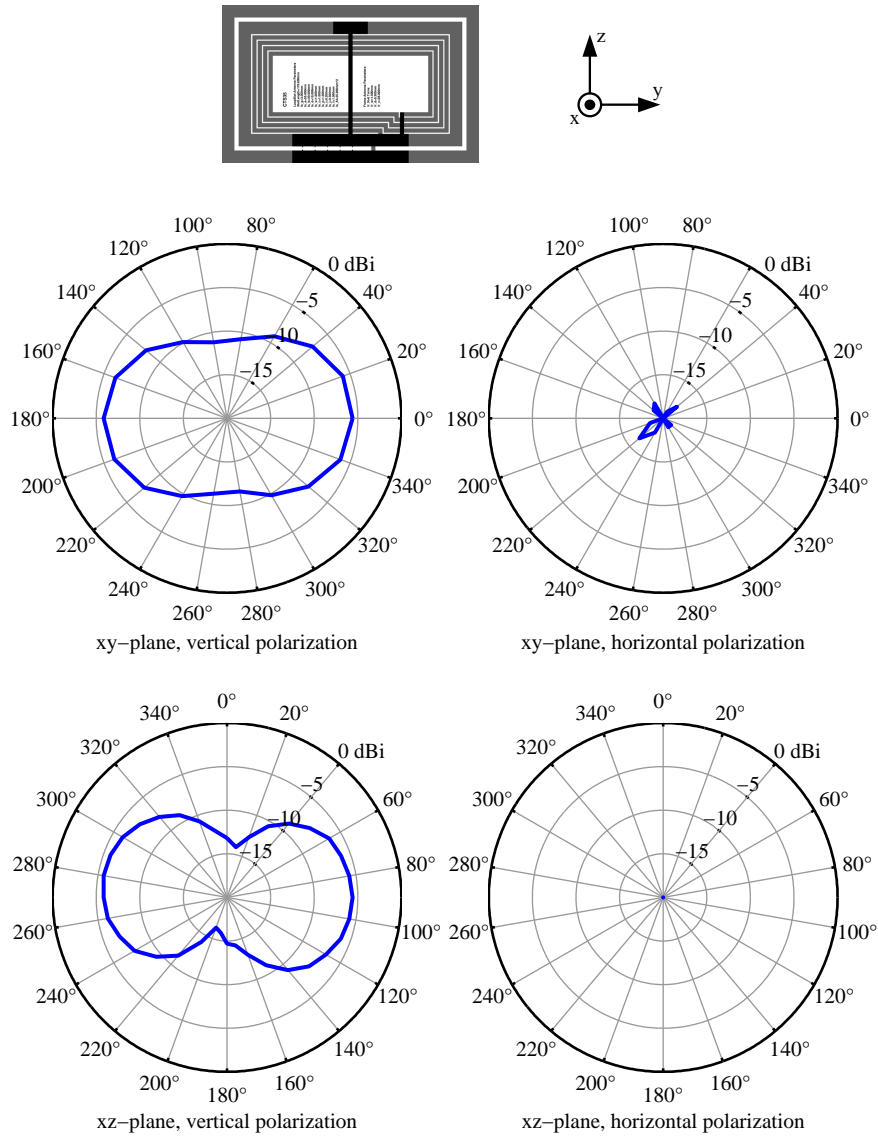


Figure 3.11: Measured gain of the dual-band antenna with HF winding inside (CTS35) in horizontal and vertical polarization.

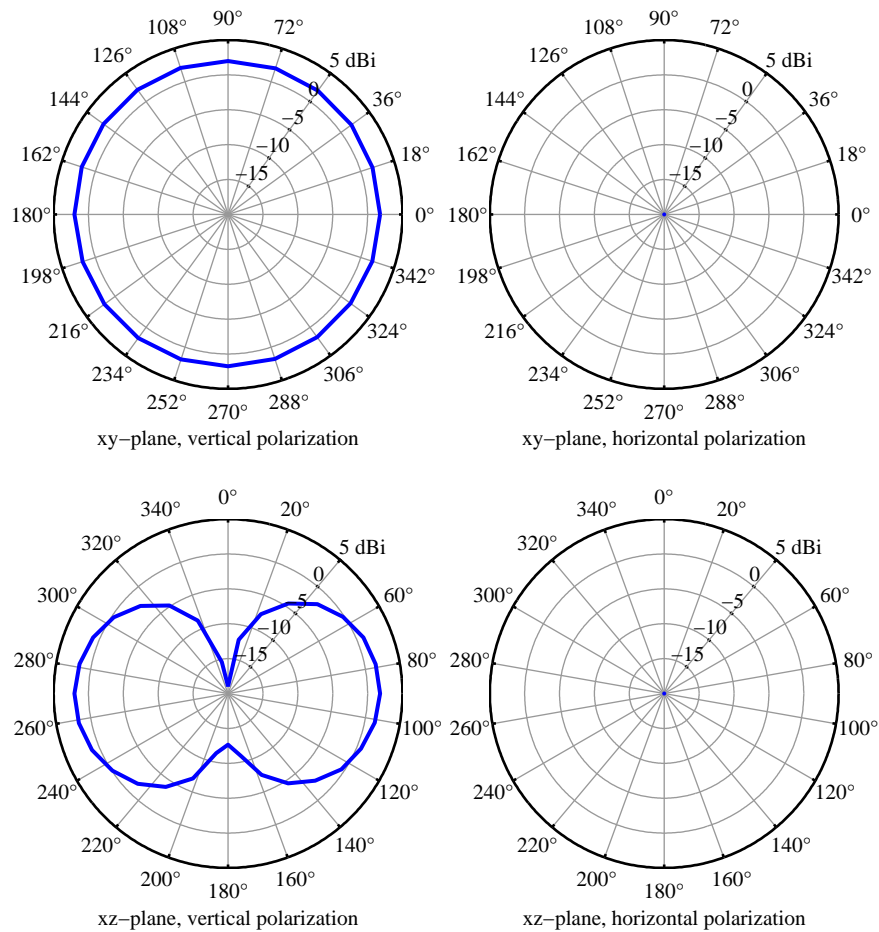
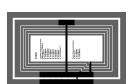


Figure 3.12: Measured gain of the reference dipole in horizontal and vertical polarization. The dipole is aligned in parallel to the z-axis.

Table 3.7: Antenna performance figures for the half-wavelength dipole, the optimized shorted loop slot antenna, and the three dual-band antenna variants.

antenna type	Dipole	CTS29	CTS27	CTS28	CTS35
					
max. total gain	2.09 dBi	0.02 dBi	-1.98 dBi	-4.75 dBi	-5.51 dBi
max. vertical gain	2.08 dBi	-0.02 dBi	-2.53 dBi	-5.50 dBi	-5.53 dBi
max. horizontal gain	-19.92 dBi	-10.48 dBi	-8.12 dBi	-9.90 dBi	-15.06 dBi
antenna efficiency	0.0 dB	-3.64 dB	-5.66 dB	-8.44 dB	-8.47 dB
cross polarization ratio	26.28 dB	11.13 dB	6.72 dB	5.57 dB	11.67 dB

### 3.5 Summary

A new antenna structure operating in both, the HF and the UHF band, was found. The antenna structure consists of a shorted loop slot antenna serving the UHF band and a coil antenna serving the HF band. It was explained how the antenna can be matched to state-of-the-art tag chips by tuning a few geometric parameters. A very thin and flexible laminate was used to allow easy integration into product packaging.

A simplified planar simulation model for the dual-band antenna was set up to determine the effects of the geometric parameters and to predict the antenna's radiation behavior. For verification, some antenna variants—two for dual-band operation and two without HF capabilities—were picked and investigated. By measurement, a comparison to conventional single-band antennas showed that performance at UHF is degraded by some few dB, while performance at HF is very well preserved. The possibilities and limits in finding a trade-off between HF and UHF performance for a given application are explained. For this dual-band antenna, a U.S. patent [65] was filed.



## 4 An interrogator antenna with high transmit to receive separation

In this chapter an antenna is described that allows simultaneous transmission and reception in the same frequency band. Circular polarization is employed for a most reliable communication with RFID transponders that typically have linearly polarized antennas. To achieve high separation between transmitted and received signals, a square patch antenna originally transmitting horizontally and vertically polarized radiation is combined with a 3 dB-hybrid circuit. With this hybrid circuit the antenna can simultaneously radiate a right-hand circularly polarized wave and receive a left-hand circularly polarized wave. Furthermore, the transmit signal that is unintentionally leaking into the receive path can be compensated by tuning the hybrid circuit with two variable capacitance diodes. At 866 MHz a maximum Tx / Rx-separation of 65 dB was achieved in a static scenario. In a time variant indoor scenario with a metal object moving on a conveyor belt a Tx / Rx-separation of more than 52 dB was achieved by continuously tuning the hybrid circuit with a minimum-search algorithm.

### Original publications related to this chapter

L. W. Mayer and A. L. Scholtz, “Circularly polarized patch antenna with high Tx / Rx-separation,” in *Proc. IEEE International Conference on RFID*, (Orlando, Florida, USA), Apr. 2009.

L. W. Mayer, “Hochfrequenz-Richtkoppler.” European patent EP09450084. Applicant: Lukas W. Mayer, filed April 22nd, 2009.

### 4.1 Motivation

Antennas that are simultaneously used for transmitting and receiving signals at one single carrier frequency are required in a variety of applications like radar or RFID. In RFID applications power and data are transmitted in the same frequency band.

Transponders have to be continuously supplied with power radiated by the reader antenna—also during data transmission from the transponder to the reader. This data transmission is achieved by a modulation of the transponder antenna load which intelligibly causes a very weak returned signal—at least in comparison to the power continuously radiated to supply the transponder. Thus, an important property of an RF-frontend or an antenna used for RFID readers is its ability to separate the received from the transmitted signal (Tx/Rx-separation  $\alpha$ ). The following options are commonly used to achieve Tx/Rx-separation:

- A directional coupler or a circulator can be used to separate the incident and the reflected wave at the antenna port. Imperfect matching—which comes along with every antenna—causes some of the transmit power to be reflected at the antenna input. Thus, with a directional coupler or a circulator the Tx/Rx-separation is limited to the antenna’s return loss. A tunable antenna [66] might bring an improvement, but a further degradation of performance can be expected from the imperfect coupler or circulator. Typically, only a Tx/Rx-separation of  $\alpha < 20$  dB can be achieved.
- Antennas that transmit and receive waves with different polarization are usually a better choice to achieve decent Tx/Rx-separation. Such antennas have more ports—one for vertical and one for horizontal polarization, for instance—and are optimized for high cross-polarization ratio. Often, hybrid circuits are used to feed such antennas which provides different polarization modes [67, 68, 69]. Tx/Rx-separation of  $\alpha \approx 30$  dB can be achieved with such antennas [70].
- If Tx/Rx-separation is to be improved beyond that, active decoupling methods are necessary. Basically, a version of the transmitted signal that can be adjusted in delay and amplitude is added to the signal returned from the antenna. If delay and amplitude are correctly set, the transmit signal that leaks into the receive output is canceled [71, 72].

For best Tx/Rx-separation as required in future RFID applications, I combined a dual-polarization antenna with an active Tx/Rx-decoupling circuit. The decoupling circuit is directly mounted on the antenna.

The operation principle of the antenna is described in Section 4.2. A modified 3dB-hybrid circuit presented in Section 4.3 is used to feed a dual-polarized microstrip patch antenna. The hybrid can be connected to the transmit output of an RFID frontend. The receive output of the hybrid then provides the received signal to the frontend. Simulations and measurement results of a first prototype of the hybrid circuit are also presented in Section 4.3. Radiation is generated by a microstrip patch antenna that has two ports for horizontal and vertical polarization. Design and simulation of the bare patch antenna are given in Section 4.4.

The control hardware that is used to adjust the tuning of the antenna is briefly described in Section 4.5. With this hardware, the performance of the antenna together with the hybrid circuit is then determined by measurement. Results for static and time variant scenarios are given in Section 4.6. Methods for optimizing the antenna for RFID systems are described in Section 4.7. Section 4.8 discusses the applicability and benefits of the antenna in future RFID systems and draws conclusions.

## 4.2 Antenna principle

Since in RFID systems circularly polarized radiation is favored to account for the unknown orientation of transponder antennas (see Section 1.3.3), an antenna was built that transmits right-hand circularly polarized waves and receives left-hand circularly polarized waves. This is achieved by a combination of a cross-polarized antenna originally radiating horizontal and vertical polarization and a 3 dB-hybrid circuit. The basic property of the hybrid is splitting the power incident at one of its ports into two equal parts with a phase difference of  $+90^\circ$  or  $-90^\circ$ —depending on which port was chosen. This can be exploited to achieve right-hand and left-hand circular polarization by using a dual-input cross-polarized antenna. Due to the theorem of reciprocity, the antenna with the hybrid can be used to either transmit or receive circularly polarized radiation. For this application a right-hand circularly polarized wave is radiated by applying power to the first port of the hybrid. The second port of the hybrid on the other hand will be used to receive a left-hand circularly polarized wave.

If the hybrid circuit and the antenna inputs are well matched and the antenna is operating in free space—ideally—no power is present at the left-hand circular port when transmitting on the right hand-circular port of the hybrid. In practice however, a Tx/Rx-decoupling of approximately 30 dB has been achieved with a generic hybrid circuit and a square patch antenna built in house. The measurement was carried out in an anechoic chamber.

In the real world, manufacturing tolerances and—more importantly—the reception of electromagnetic waves that are reflected at objects in the proximity of the antenna impair the Tx/Rx-separation. It is in the nature of RFID systems that the environment around the antenna changes versus time. Consequently, the signal power at the receive port changes as well and makes the detection of a weak signal returned by a transponder more difficult. In this case the Tx/Rx-separation can be improved by adaptively tuning the hybrid circuit.

## 4.3 Tunable hybrid

The use of variable capacitance diodes inserted into hybrid couplers has been known for long. Most recent advances are presented in [73], where the center frequency of a coupler is adjusted to allow switching between several narrow frequency bands. Varactor diodes were also used in a hybrid circuit by Ferrero [74] to reconfigure an antenna to allow different polarization modes. In this work however, the maximization of the Tx/Rx-separation of an antenna is achieved by inserting two variable capacitance diodes into a hybrid circuit. By applying two independent reverse voltages to the varactors the RF signals that are passing through them can be controlled separately. The diodes are placed across gaps in each of the two transmission lines of the hybrid that lead to the receive port (see Figure 4.1). Furthermore, the diodes are placed a quarter wavelength apart from each other (equivalent to a  $90^\circ$  phase shift) which enables to separately control the in-phase and the quadrature component of the signal that is coupled from the transmit port to the receive port of the hybrid. The control voltages are applied to the diodes by quarter wavelength transmission lines that isolate the RF signal from the control voltage source. With every diode there is also a bypass capacitor that blocks the control voltages from the ports of the hybrid.

For monitoring the power at the receive port, a power detector is placed in the corresponding corner of the hybrid. The detector provides an output voltage that is proportional to the logarithm of its input power. This output voltage can be used to optimize the Tx/Rx-separation by controlling the varactor voltages automatically by a minimum-search algorithm.

### 4.3.1 Simulation

The hybrid coupler that consists of a printed circuit board was simulated in ADS (Advanced Design System by Agilent Technologies). To allow a cancelation of signals with arbitrary phase shift and power at the antenna output, the coupler was investigated in ADS and optimized in its dimensions. Figure 4.2 shows the schematic used for simulation. The varactor diodes were modeled as ideal capacitors (C1 and C2). The coupler was then optimized to work similar to a generic hybrid with both varactors set to the middle of their tuning range. The full tuning range of the varactors allows to couple a small part of the transmit signal to the receive port with any phase shift between  $0^\circ$  and  $360^\circ$ . The maximum power of this coupled signal is approximately 20 dB below the input signal power. This allows to fully compensate a similarly weak parasitic signal that is leaking into the receive port by adjusting the two varactor voltages. With this arrangement, imperfections of

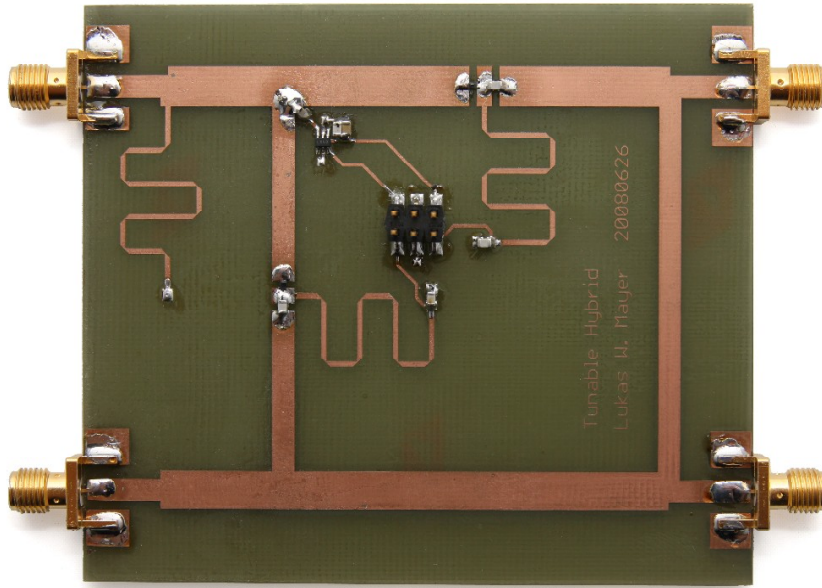


Figure 4.1: Tunable 3 dB-hybrid circuit (actual size). The Tx-input connector is on the lower left (port 1), the Rx-output connector is on the upper left (port 2). The vertical and horizontal input of the cross-polarized antenna is wired to the upper right and the lower right connector, respectively (port 3 and port 4). The power detector is seen in the upper left corner of the hybrid. Varactor diodes are placed in the middle of the upper and in the middle of the left transmission line of the hybrid. Thin meandered quarter-wave microstrip-lines are used to apply the control voltages to the varactors. The connector in the center is used to interface to an automatic tuning hardware.

the patch antenna as well as received sinusoidal signals caused by reflection of the radiated signal in space can be compensated.

Figure 4.3 shows the simulated result of the transmission coefficient  $S_{21}$  that represents the magnitude and phase of the signal that is coupled from the transmit input (port 1) to the receive output (port 2) of the hybrid.  $S_{21}$  is plotted versus a sub-range of the capacitance of the varactor diodes (C1 and C2). It is seen that tuning the two diode capacitances modulates  $S_{21}$ . The trajectories associated with the two diode capacitance values and hence with the tuning voltages applied to the diodes are quite orthogonal. This is a consequence of the diode placement within the circuit and a very important attribute of the coupler. If mutual interference between the effects of the two diode voltages is low then simple algorithms can be found to automatically tune the hybrid circuit.



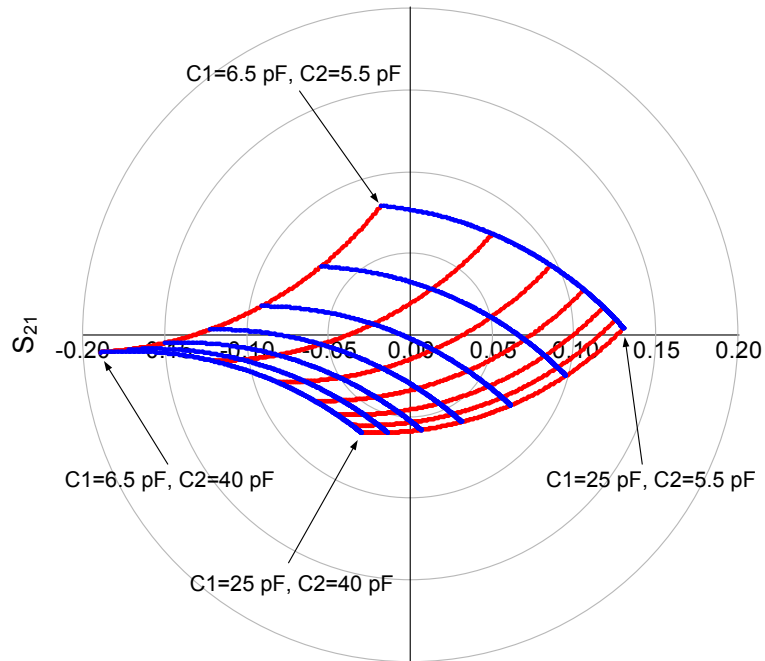


Figure 4.3: Simulation result for the transmission coefficient between input and output port ( $S_{21}$ ) versus varactor diode capacitances. Red lines indicate constant  $C1$ , blue lines indicate constant  $C2$ .

The integration of the varactor diodes into the hybrid circuit led to an aggravation of matching at the input and the output port. Sound matching could be restored by placing two low-impedance microstrip lines in front of the input and output of the hybrid circuit. In Figure 4.1 these lines extend to the left of the hybrid. In the schematic used for simulation (Figure 4.2) they are named TL7 and TL8. The effect of these additional transmission lines is shown in Figure 4.4. At 866 MHz,  $S_{11}$  is improved from  $-16$  dB to  $-25$  dB and  $S_{22}$  is improved from  $-11$  dB to  $-14$  dB. The effect on  $S_{21}$  is negligible. A comparison of simulated and measured results for the tuned hybrid circuit is given in Figure 4.5.

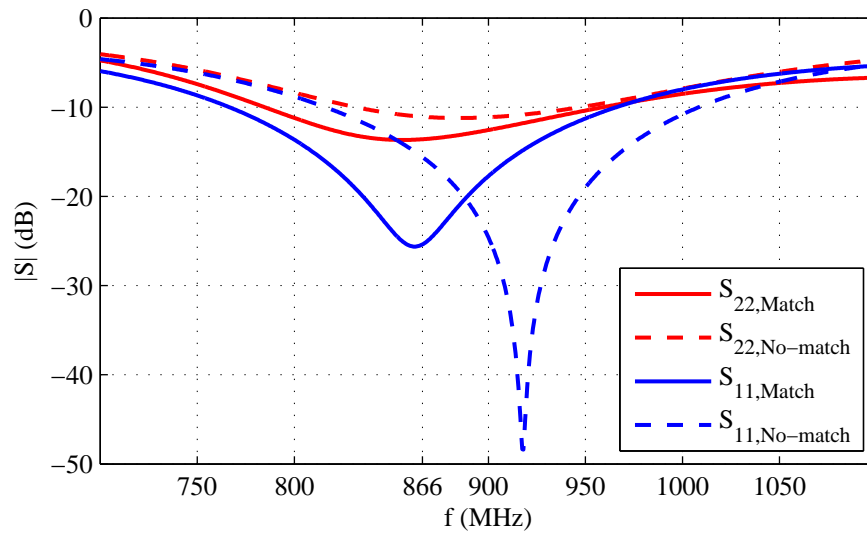


Figure 4.4: Comparison of input and output port matching with and without additional low-impedance microstrip lines.

### 4.3.2 Measurement

For testing, a version of the tunable hybrid with SMA connectors was manufactured and characterized with a 4-port vector network analyzer. Prior to the measurement, the hybrid was tuned to achieve best isolation at 866 MHz. The measured scattering parameters of the hybrid circuit at 866 MHz are

$$S = \begin{pmatrix} -38.1 \text{ dB} & -52.1 \text{ dB} & -4.0 \text{ dB} & -3.3 \text{ dB} \\ -68.8 \text{ dB} & -11.1 \text{ dB} & -4.0 \text{ dB} \angle -168.8^\circ & -4.5 \text{ dB} \angle 83.6^\circ \\ -4.0 \text{ dB} \angle 95.7^\circ & -4.0 \text{ dB} & -15.1 \text{ dB} & -27.2 \text{ dB} \\ -3.3 \text{ dB} \angle 166.1^\circ & -4.5 \text{ dB} & -28.2 \text{ dB} & -24.0 \text{ dB} \end{pmatrix}$$

where port 1 is the transmit input and port 2 is the receive output. The cross-polarized antenna is connected to port 3 and port 4. The less relevant S-parameters are shown in grey.

From the S-parameters it can be seen that the hybrid circuit introduces only losses of approximately 1 dB for the transmit and also for the receive path. This shows that a very power efficient tuning of the branch line coupler is achieved. The losses caused by the varactor diodes in the receive path are similar to the losses caused by the microstrip lines in the transmit or in the receive path. Furthermore, there is a slight deviation from the expected 90° phase shift between the two antenna ports. In practice, this will result in a not perfectly circularly polarized transmitted and received wave. However, the cross-polar discrimination is still 15 dB for transmitting and 16 dB for receiving [75]. For RFID applications where the circular polarization is only required to gain independence of the transponder's orientation, this is fairly enough.

Figure 4.5 shows the measured and simulated reflection coefficients at input ( $S_{11}$ ) and output ( $S_{22}$ ) as well as the transmission coefficient  $S_{21}$  versus frequency. At 866 MHz a high isolation between the input and the output port is achieved. The simulation result for  $S_{21}$  also agrees very well with the measurement.

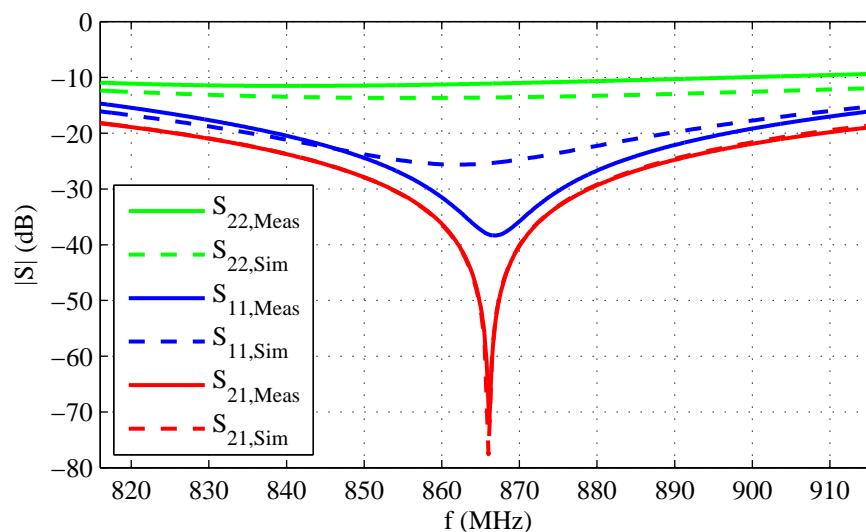


Figure 4.5: Measured and simulated S-parameters of the tuned hybrid versus frequency.

## 4.4 Square patch antenna

A microstrip square patch antenna with air dielectric that radiates horizontally and vertically polarized waves was built. The two ports of the antenna are connected to the patch by probe feeds and excite two orthogonal modes of oscillation of the patch. The positions of the feeding points were determined by simulation of the antenna in HFSS v11. To obtain a most efficient design, a new version of the hybrid coupler was developed that can be directly mounted at the back of the antenna's ground plane. Figure 4.6 shows the structure of the antenna with the circuit board mounted at its back side. With this arrangement the patch can be directly connected to the antenna ports of the hybrid by two conducting bolts that are fed through the ground plane of the antenna. The input impedance of the patch antenna was optimized to  $50\ \Omega$ . The component side of the tunable hybrid circuit was chosen as the reference plane for impedance optimization. The effects of the two bolts connecting to the patch are thus considered in the impedance optimization.

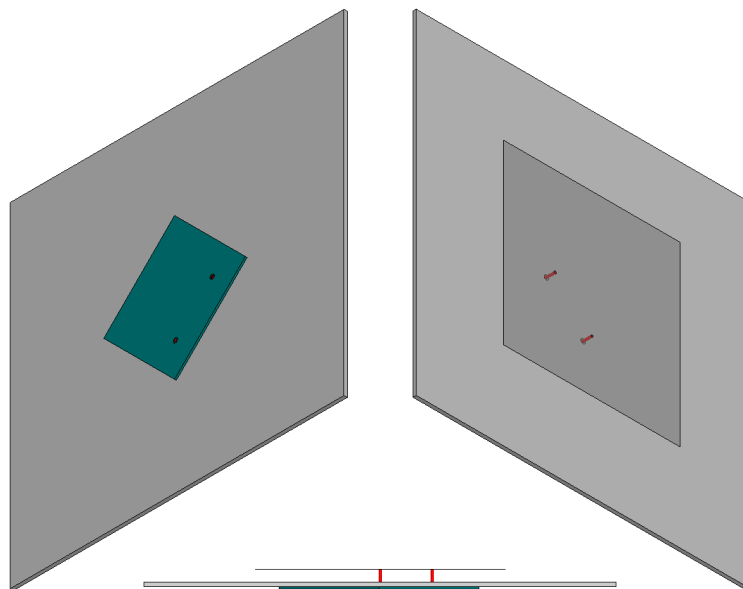


Figure 4.6: Structure of the square patch antenna with the hybrid coupler mounted directly at the back of the antenna's ground plane. The bolts connecting the patch with the hybrid circuit are shown in red. The circuit board is drawn in green. In the right drawing the patch is displayed with 50% transparency to display the feeding bolts.

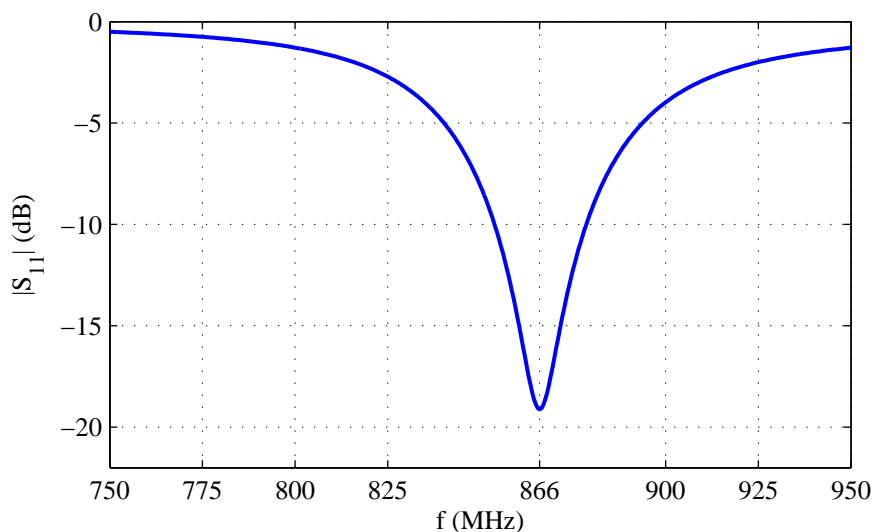


Figure 4.7: Simulated input reflection coefficient  $S_{11}$  of one input of the square patch antenna in dB.

#### 4.4.1 Simulation

Figure 4.6 shows the simulation model of the patch antenna. The patch consists of 1.5 mm aluminum sheet metal. The 30 cm by 30 cm ground plane has a thickness of 3 mm. Sufficient bandwidth was obtained with a distance of 8 mm between the ground plane and the patch [76]. By simulation, a center frequency of 866 MHz was obtained for a patch dimension of 158 mm by 158 mm. Matching to  $50 \Omega$  is best at a feed point offset of 33 mm measured from the patch center. In both polarization modes the antenna has a maximum simulated gain of 9.5 dBi and a half power beam width of  $58^\circ$  in the respective E-field direction and  $64^\circ$  in the respective H-field direction. With the aluminum conductors, its efficiency is expected to be higher than 95%. The simulated input reflection coefficient of one of the antenna inputs is presented in Figure 4.7. From the result, a bandwidth<sup>1</sup> of 24.5 MHz was computed. The simulation results were confirmed by a measurement of the port impedance with a vector network analyzer. Therefore, a flange SMA connector was mounted to the back of the manufactured antenna instead of the printed circuit board. With this, a center frequency of 864 MHz and a bandwidth of 24.3 MHz was determined for the manufactured antenna.

<sup>1</sup>Bandwidth where the reflection coefficient at the antenna input is smaller than  $-10$  dB.

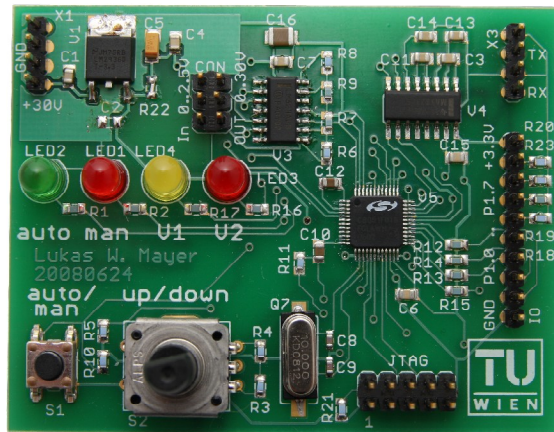


Figure 4.8: Microprocessor board for hybrid tuning control (actual size). The microprocessor is seen on the right. A quad operational amplifier (upper IC) is used to convert the DAC-output voltage into the control voltage for the variable capacitance diodes (0..30 V). An RS-232 driver IC is seen in the upper right corner. A button for switching between automatic and manual tuning mode is placed in the lower left corner. Next to the button is a dial wheel to manually adjust the diode voltages. Some LEDs show the status of the program.

## 4.5 Automatic tuning hardware

This hardware consists of a circuit featuring a microprocessor with analog to digital (AD) and digital to analog (DA) converters. The AD converter samples the output voltage of the power detector with 10 bit resolution ( $U_{\text{LSB,AD}} = 3.2 \text{ mV}$ ). Two 12 bit DA converters provide the control voltages for the diodes. An operational amplifier sets the voltage range of  $U_1$  and  $U_2$  to 0..30 V ( $U_{\text{LSB,DA}} = 7.3 \text{ mV}$ ). In software, a modified gradient algorithm that automatically tunes the hybrid circuit was implemented. Manual adjustment of the diode tuning voltages  $U_1$  and  $U_2$  is also possible with a dial wheel. A photograph of the automatic tuning hardware is shown in Figure 4.8.

## 4.6 Performance testing

By measurement in an anechoic chamber the basic behavior of the cross-polarized microstrip patch antenna with the hybrid circuit attached was determined. Therefore, the detector power—or equivalently speaking the power at the receive port—

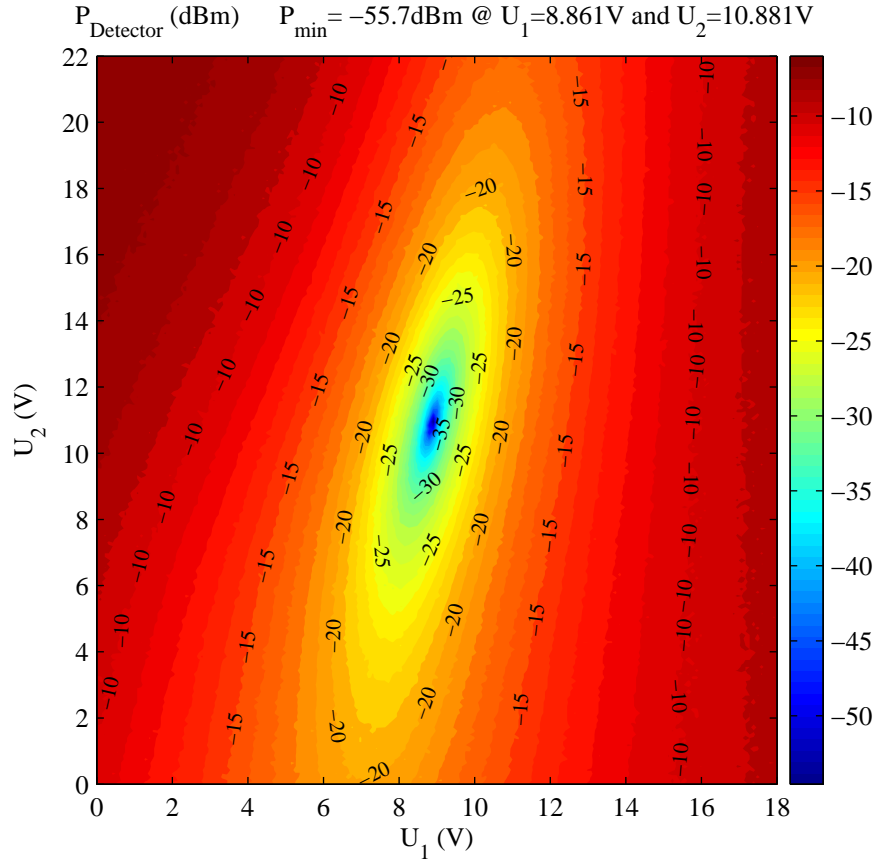


Figure 4.9: Output power versus diode tuning voltages  $U_1$  and  $U_2$ .

was measured versus the varactor tuning voltages  $U_1$  and  $U_2$ . In Figure 4.9 it is seen that a minimum detector power of  $P_{\text{Detector}} = -55.7\text{ dBm}$  is achieved at  $U_1 = 8.86\text{ V}$  and  $U_2 = 10.88\text{ V}$ . The measurement was taken with a 10 dBm sinusoidal signal at the transmit port. Thus, a maximum Tx/Rx-separation of 65.7 dB was achieved in this static scenario.

It should be noted that the minimum power at the receive port might be much smaller than the detector readout. This is due to the limited dynamic range of the detector chip which has an RF input power range between  $-60\text{ dBm}$  and  $0\text{ dBm}$ . In fact, measurements with a spectrum analyzer and manual tuning of the varactor reverse voltages led to a Tx/Rx-separation of more than 80 dB. Thus, great potential is seen in this design when equipped with a more sensitive power measuring device.

In time variant scenarios where objects moving in space introduce reflections, the varactor voltages  $U_1$  and  $U_2$  have to be continuously adjusted to keep the Tx/Rx-

separation as high as possible. In the contour plot shown in Figure 4.9, time variance will cause a movement of the minimum power position.

Digital signal processing hardware was used to implement a simple minimum-search algorithm that continuously tunes the varactor voltages  $U_1$  and  $U_2$  based on the detector power  $P_{\text{Detector}}$ . Testing the automatic tuning algorithm was done with the following measurement procedure:

- The antenna with the tunable hybrid and the automatic tuning circuit was mounted on a pole in an anechoic chamber.
- 15 cm in front of the antenna a half-wavelength copper strip mounted on a conveyor belt was placed. This metal causes a very strong reflected signal and is used to fathom the antenna performance. When the conveyor belt moves, the metal sweeps past the antenna. At  $x = 0$  m, the metal resides directly in front of the antenna.
- The transmit port of the antenna is fed with a 10 dBm sinusoidal signal.
- The power at the receive port was recorded by reading the detector voltage while the metal was swept past the antenna.
- The conveyor belt with the metal was moved from  $x = -0.5$  m to  $x = 0.5$  m twice. First with constant varactor voltages that were tuned to achieve best Tx/Rx-separation in the empty chamber. This case is equivalent to a patch antenna fed by a generic hybrid circuit that is optimized to have best Tx/Rx-separation in free space. In the second sweep, the hybrid circuit was continuously adjusted by tuning the varactor voltages with a minimum-search algorithm.

The result of the measurement is seen in Figure 4.10. For the case with constant varactor voltages, a 45 dB variation of received power is encountered while the reflecting metal is moving. Especially at  $x = 0$  m, where the reflecting metal is closest to the antenna, a strong signal is present at the receive port. Still, a Tx/Rx-separation  $\alpha$  of 20 dB is retained. This is due to the highly optimized antenna and hybrid circuit.

Secondly, during the sweep with the continuous minimum-search algorithm switched on, the detector power remains below  $-42$  dBm. With the transmit power set to 10 dBm, this corresponds to a Tx/Rx-separation  $\alpha$  well above 52 dB. This is an improvement of 32 dB compared to fixed varactor voltages (or a perfectly well built generic antenna of this kind). The ripple in the detector power is caused by the minimum-search algorithm. It will be possible to reduce this ripple to less than 1 dB by implementing a better algorithm. With this, a Tx/Rx-separation of approximately 60 dB will be achieved.

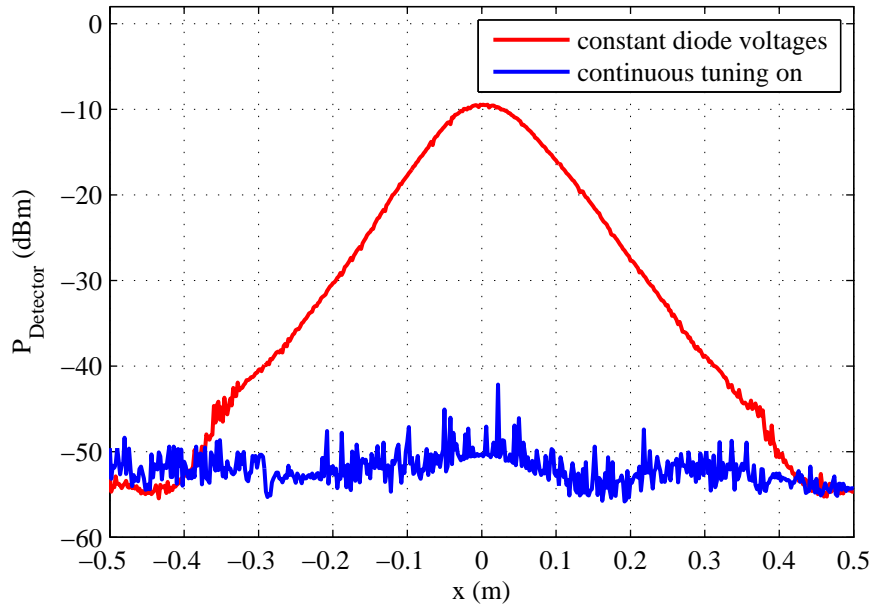


Figure 4.10: Detector power (equivalent to receive port power) versus position of a metal reflector sweeping past the antenna on a conveyor belt. At  $x = 0$  m the metal resides directly in front of the antenna.

In Figure 4.11 the varactor tuning voltages  $U_1$  and  $U_2$  are shown as a function of conveyor belt position  $x$ . Four test scenarios have been characterized. First, a metal reflector was placed on the conveyor belt. Because the reflected signal that has to be canceled by the hybrid circuit is strong, the varactor voltages vary most for this test case. Furthermore one single RFID transponder was put on the conveyor belt. Since the signal reflected by this tag is by far weaker than the signal reflected by the metal, the varactor tuning voltages vary less. A similar result is obtained with six different transponders attached to the conveyor belt with some 80 mm distance from each other. For reference, a measurement with the empty conveyor belt is also shown. During all four measurement runs, the Tx/Rx-separation remained well above 52 dB.

## 4.7 Considerations for automatic tuning

With this antenna an improvement in reading RFID transponders is achieved because imperfections of the antenna itself as well as parasitic sinusoidal signals that fade in and out versus time are suppressed. The response of a transponder on the other hand is a fastly modulated reflected signal only present for a short period of time. Of course—in theory—a very fast minimum-search algorithm could cancel

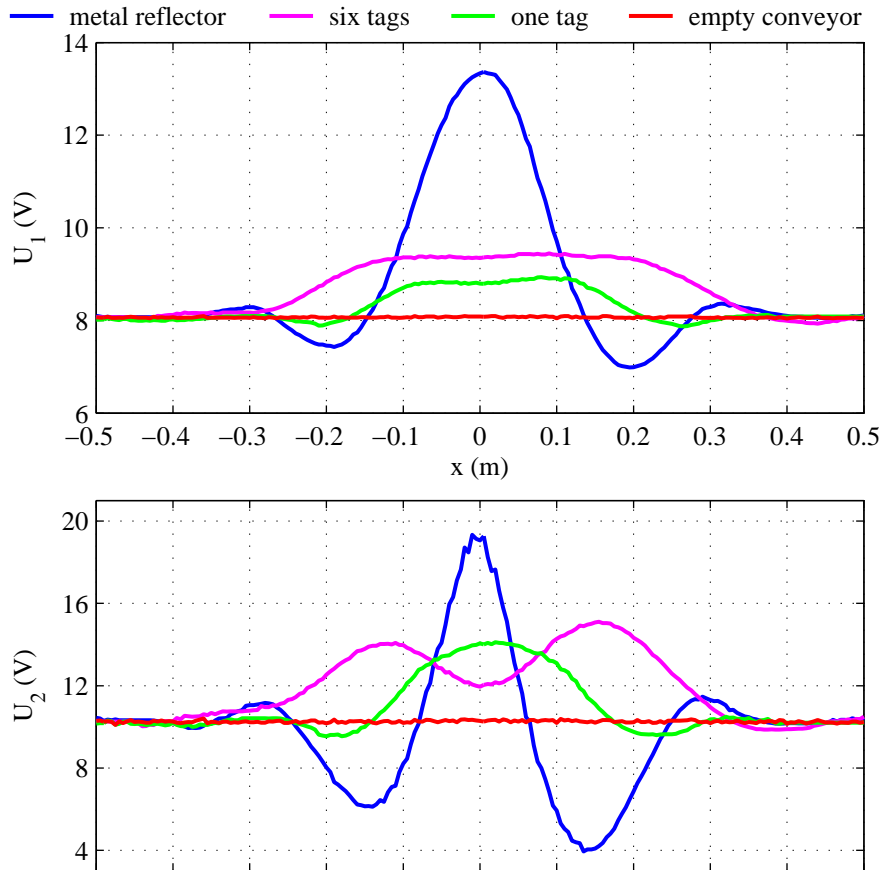


Figure 4.11: Automatically tuned varactor voltages  $U_1$  and  $U_2$  during test runs with a metal reflector, one single RFID transponder, and 6 transponders positioned next to each other on the conveyor belt passing by the antenna. For reference, a measurement with the empty conveyor belt is also shown.

the response caused by a transponder too. However, if the designer of the algorithm has good knowledge of the temporal behavior of the scenario, a minimum-search algorithm can be parameterized that levels out reflected signals that do not carry information, while letting signals returned by transponders pass directly to the receive port. Another option is of course to halt the minimum-search algorithm for the period of time where a tag's response is expected (e.g. after an inventory command) and engage it afterwards. This also eliminates possible interference of the minimum-search algorithm during a tag's response. Whichever way is preferred, the result is that the superimposed carrier signal is strongly reduced while the transponder's response passes directly to the receive port. This makes the detection of the weak returned transponder signal a lot easier.

## 4.8 Summary

The employment of this antenna with high Tx / Rx-separation in an RFID system enables to receive weak signals returned from transponders at less effort compared to conventional techniques like active carrier cancelation. This allows cheaper RF-frontends because an expensive circulator or directional coupler are not required and—as long as digital signal processing hardware is used—less dynamic range is needed at the receiver. Furthermore, the suppression of the transmitted signal is directly done at the antenna where the received signal has the best signal-to-noise ratio. With a low-noise amplifier directly connected to the receive port of the tunable hybrid circuit this signal-to-noise ratio can be well preserved, even if the antenna cable leading to the RFID reader frontend is long and lossy.

# 5 Gain and impedance measurement method for transponder antennas

It was shown by numerous authors that the characterization of RFID transponder antennas that are favored to be small, have low gain, and show a strongly reactive input impedance, is far from trivial. In this chapter a method is presented that utilizes a small, highly-stable, battery-driven signal source to generate a sinusoidal transmit signal directly at the transponder antenna. The signal source is equipped with a tunable matching network that allows to determine the antenna impedance by a source-pull measurement. Also, with this autonomous signal source it is possible to perform accurate 3D gain measurements by means of a two axis rotation apparatus. From the measurement results the directional pattern and the antenna efficiency are derived. For verification, I perform a test measurement of a half-wavelength dipole and find good agreement of measured and theoretical data.

## Original publications related to this chapter

L. W. Mayer and A. L. Scholtz, “Efficiency measurement method for UHF transponder antennas,” in *Proc. The First International EURASIP Workshop on RFID Technology*, (Vienna, Austria), pp. 17–20, Sep. 2007.

L. W. Mayer and A. L. Scholtz, “Gain and input impedance measurement for UHF transponder antennas,” in *Proc. International Symposium on Antennas and Propagation*, (Taipei, Taiwan), Oct. 2008.

## 5.1 Motivation

It has been published in numerous articles that the characterization of directional pattern and input impedance of small antennas is far from trivial [77, 78]. The main reason is that a measurement cable leading to the antenna-under-test has

to be avoided because it carries common-mode currents that may cause radiation by far stronger than the original radiation of the antenna. The fact that in RFID technology, antennas are not only small but also lossy due to low-cost manufacturing processes, makes the characterization of such antennas particularly difficult.

In [79] a method specific for antennas used in mobile equipment is presented. A small, battery-powered VCO<sup>1</sup> is used to generate a CW<sup>2</sup> signal directly at the antenna. Since antennas in mobile equipment are operated by an RF frontend typically presenting a 50  $\Omega$  impedance, matching issues are not considered in detail. Although maximum gain and efficiency of the antenna can be determined with the method in [79], the directional pattern is left unexplored.

A more advanced method that uses fiber optics instead of a measurement cable is presented in [80]. This is a very promising approach because it allows to determine gain, phase patterns, and also the input impedance. On the downside, the assembly needed at the antenna site is by far too large to apply this method to RFID transponder antennas.

A very interesting approach to measure the input impedance of RFID tag antennas is given in [81]. The impedance is determined from measurements of the antenna in a transverse electromagnetic (TEM) cell. For calibration, reflection measurements are carried out for which the transponder antenna is loaded with different calibration standards and placed in the cell. In a next step, tag antennas that are loaded with transponder chips are measured and from the results the antenna impedance is calculated. However, to my understanding, the results depend on the accuracy of the chip impedance which has to be known or characterized separately.

Input impedance measurements are also shown in [82], where an on-wafer-prober is modified to characterize planar antennas. The authors put the antenna on a styrofoam spacer and use absorbing material to reduce the impact of the on-wafer-prober and the probe-head metal. Still, it is argued that the probe head influences the measurement results.

I propose to characterize gain and input impedance of RFID tag antennas by means of a small, battery-driven oscillator that is mounted directly on the antenna and generates a sinusoidal transmission signal at 864 MHz. The oscillator is equipped with a tunable matching network that allows power matching with the antenna (Section 5.4). With this tunable signal source, the antenna's input impedance can be determined by a source-pull method (Section 5.5).

---

<sup>1</sup>VCO: voltage controlled oscillator

<sup>2</sup>CW: continuous wave

For the directional pattern measurement, the autonomously operating oscillator supplies the tag antenna with RF power. The antenna is thus operated autonomously without the disturbance of a measurement cable. Section 5.2 describes the gain measurement and also shows how to compute the antenna efficiency from the results. The apparatus that allows to automatically rotate the antenna around two axes is discussed in Section 5.3. The method is verified with a test measurement of a half-wavelength dipole presented in Section 5.6. The measured characteristics of the dipole agree very well with the theoretical data.

## 5.2 Directional pattern and antenna efficiency measurement

This section discusses a characterization method that allows proper measurement of directional pattern, gain, and efficiency of transponder antennas.

The fact that transponder antennas have to be low cost often rules out the use of quality materials and a precision manufacturing process like etched copper. In addition to that the antennas are preferred to be small. These constraints have an impact on the antenna efficiency which is often below 30%. Furthermore, the radiation pattern of small antennas approaches that of a Hertzian dipole which means that there is no substantial directivity. When a cable is used to connect such an antenna with measurement equipment, common mode currents will be induced along the cable. These currents will much more seriously corrupt the measurement results of a low directivity antenna than observed with a highly directive antenna. A small, high-quality balun might reduce this problem if the cable extends exactly along the antenna's symmetry plane. Foregoing experiments in an anechoic chamber showed that if this is not the case, input impedance and radiation pattern measurements are not reproducible. Surrounding the cable with absorbing material reduces common mode currents which improves the accuracy of the input impedance measurement. On the other hand the absorbing material drains energy from the field which leads to inaccurate gain and efficiency figures.

Results that reveal the characteristics of the antenna when combined with a transponder chip and placed in a certain environment can thus only be achieved by a measurement that does not require a cable [83, 84]. The gain can therefore best be measured by the use of a small, autonomous calibrated receiver or transmitter that is directly connected to the transponder antenna. With the battery powered oscillator described in Section 5.4 such a calibrated transmitter was made available.

Once a gain measurement is set up, the directional pattern of the antenna can be determined. This is done by rotating the antenna around two axes (azimuth and elevation) with an adequate angle increment and taking a series of gain measurements (see Section 5.3). To calculate the total radiated power, both the horizontally and the vertically polarized field components have to be determined. From these results the radiated power for each polarization is calculated according to

$$P_{\text{Rad},i} = \int_0^{2\pi} \int_0^\pi P_{\text{In}} \frac{G_{\text{Iso},i}(\vartheta, \varphi)}{4\pi} \sin(\vartheta) \, d\vartheta \, d\varphi, \quad (5.1)$$

where  $G_{\text{Iso},i}(\vartheta, \varphi)$  denotes the antenna gain for polarization  $i$  (horizontal or vertical) compared to the isotropic radiator and  $P_{\text{In}}$  denotes the power that is available at the antenna input [85]. The symbols  $\varphi$  and  $\vartheta$  refer to the azimuth and the polar angle coordinate, respectively. Finally, the antenna efficiency can be calculated as

$$\eta = \frac{P_{\text{Rad,Hor}} + P_{\text{Rad,Ver}}}{P_{\text{In}}}. \quad (5.2)$$

### 5.3 Rotation unit

To automate antenna pointing, an apparatus was designed that incorporates an azimuth rotator that is placed on the floor of an anechoic chamber. On top of this rotator a tower made of polystyrol foam is mounted. The height of this tower is adjustable. The transponder antenna is attached to the elevation unit that consists of a stator and a rotor also made from polystyrol foam. Stator and rotor are connected by ball bearings that consist of polyurethane rings and glass balls. Attached to the rotor, there is a disc made from Rohacell that drives the rotor via a perlon cord that is moved by a stepper motor located at the bottom of the tower. This design offers the following advantages:

1. No conducting elements are included in the apparatus except for the ones located at the floor of the chamber which are “hidden” by pyramid absorbers.
2. There are no materials that show significant dielectric constants except for the small glass balls and polyurethane rings that are contained in the bearings.

This preserves the natural propagation of electromagnetic waves like in free space very well and thus enables exploring the radiation behavior of an antenna pointing in any direction. A photograph of the elevation unit that is located at the top of the tower is shown in Figure 5.1.

Please note that for the sake of simplicity of the apparatus, the dipole is mounted horizontally. This implies that the calibrated pickup antenna also has to be aligned horizontally to characterize the dipole’s radiation pattern for vertical polarization.

Consequently, rotating the tower axis modifies the polar angle  $\vartheta$  whereas turning the rotor at the top of the apparatus modifies the azimuth angle of the dipole measurement.

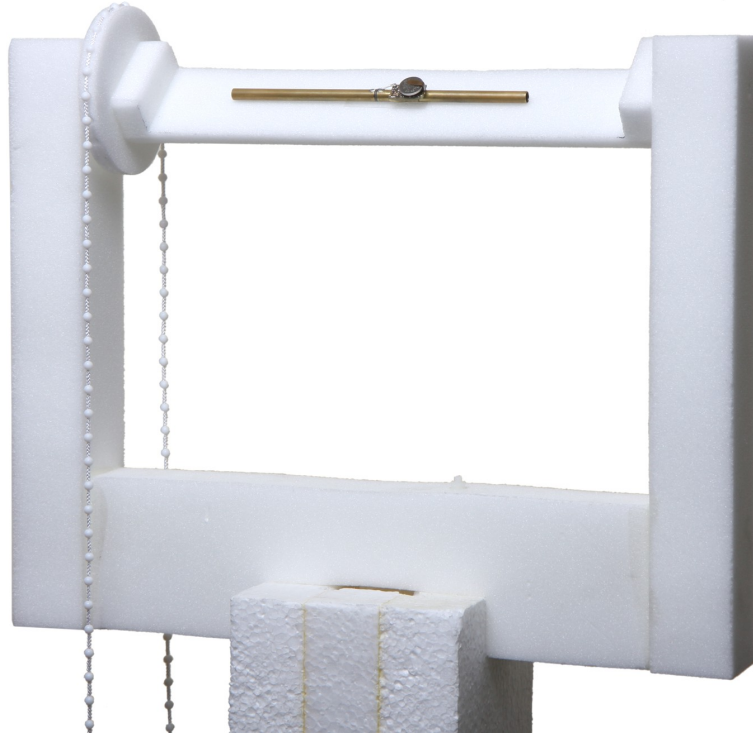


Figure 5.1: Photograph of the rotation unit with the half-wavelength dipole and the test oscillator attached.

## 5.4 Small battery driven oscillator

The accuracy of the measurement mostly depends on the properties of the oscillator that has to provide

- sufficient output power to overcome noise at the receiver,
- stable frequency and power level, regardless of battery status and load situation,
- a matching network that is tunable to the complex conjugate of the antenna impedance,
- sufficient battery life to conduct the measurement procedure, and

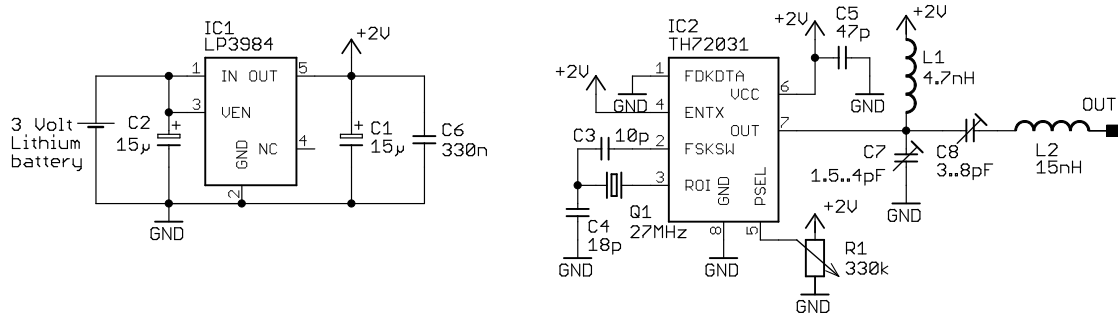


Figure 5.2: Oscillator schematic. The stabilized voltage regulator is seen to the left and the oscillator chip with its components is drawn to the right. C7 and C8 can be tuned to match the source impedance with transponder antennas.

- it has to be small enough to maintain the electrical properties of the antenna-under-test.

The oscillator unit is built around a fully integrated PLL-stabilized oscillator chip TH72031 by Melexis Microelectronic Integrated Systems [86]. The chip contains a crystal oscillator that operates with an external quartz, a PLL unit that transfers the crystal frequency to 864MHz, and a power amplifier that allows to set the output power to four different levels between  $-12$  dBm and 9.5 dBm. The schematic of the oscillator unit is depicted in Figure 5.2.

At the output, the oscillator is equipped with a matching network that transforms the output impedance of the chip ( $Z_{\text{osc pin7}} \approx (15 - 56j) \Omega$ ) to an impedance available at the oscillator's output  $Z_{\text{out}}$ . The matching network consists of two inductors (L1 and L2) and two tunable capacitors (C7 and C8). By tuning the capacitors, the real and imaginary part of the output impedance of the oscillator can be adjusted. A miniature coaxial connector (W.FL series by Hirose Electric Co.,LTD.) allows to connect the oscillator to measurement equipment or to an antenna with a thin coaxial cable. This cable introduces an electrical delay which leads to a transformation of the antenna impedance. For best matching, the output impedance of the oscillator  $Z_{\text{out}}$  is therefore not the complex conjugate of the antenna impedance  $Z_{\text{Ant}}^*$  but rather matched to the transformed version of the antenna impedance  $Z'_{\text{Ant}}$ .

To further improve stability, a linear, low-dropout, low-noise, fixed voltage regulator (LP3984) was inserted to obtain a more stable 2V supply voltage from the 3V lithium button cell (CR1220, 25 mAh). The voltage regulator enables stable operation of the oscillator until the battery voltage drops below 2.0 V. Figure 5.3 depicts the oscillator's frequency  $f$  and output power  $P$  versus time. It is seen that during

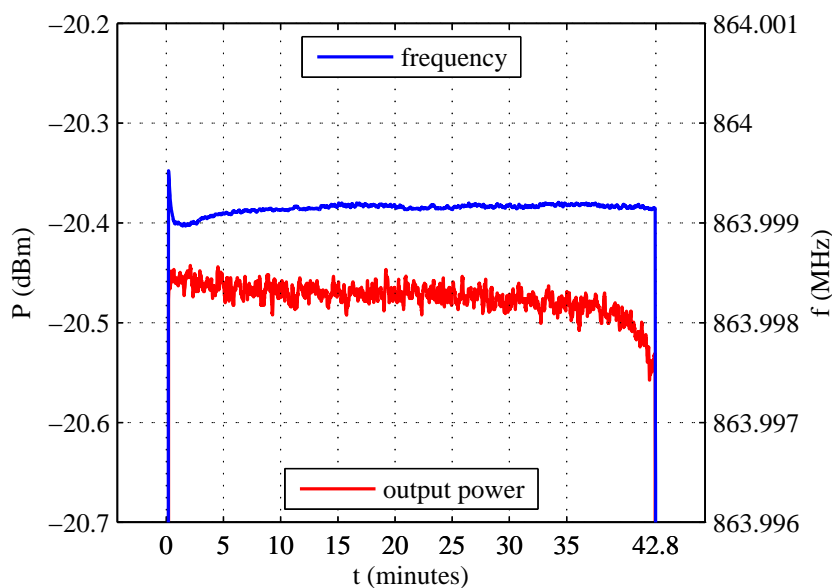


Figure 5.3: Oscillator output power and frequency versus time.

the first minute of operation the frequency varies slightly. This is due to thermal effects in the crystal oscillator and in the voltage regulator. Then, output power and frequency both remain sufficiently constant for approximately 40 minutes—long enough to conduct the antenna measurements. After 40 minutes of operation the voltage of the button cell drops below 2 V thus causing a marginal decay in output power until the oscillator switches off.

Figure 5.4 shows a photograph of the small, battery-driven oscillator. The size of the oscillator is  $18\text{ mm} \times 9\text{ mm} \times 3\text{ mm}$ . In the top left corner of the oscillator the miniature surface-mount coaxial connector can be seen. Also, the thin coaxial cable that can be routed to the antenna-under-test or to measurement equipment is shown. The 3 V lithium cell battery can be inserted between the oscillator chip and the metal clip on the right.



Figure 5.4: Battery powered oscillator with coaxial cable. The size of the unit is  $18\text{ mm} \times 9\text{ mm} \times 3\text{ mm}$ . The 3V Lithium battery can be inserted under the metal clip on the right.

## 5.5 Antenna impedance measurement

For the measurement of the antenna impedance it is essential that the oscillator described in Section 5.4 is placed at the tag antenna in a way that the interaction with the antenna is minimized. This is best achieved by placing the oscillator on the biggest metal area of the antenna. The thin coaxial cable ( $\varnothing = 0.7\text{ mm}$ ) can then be routed along the antenna metal and connected to the feed point of the antenna. The propagation delay and the losses caused by the cable are deembedded after the measurement procedure. With the battery driven oscillator the antenna

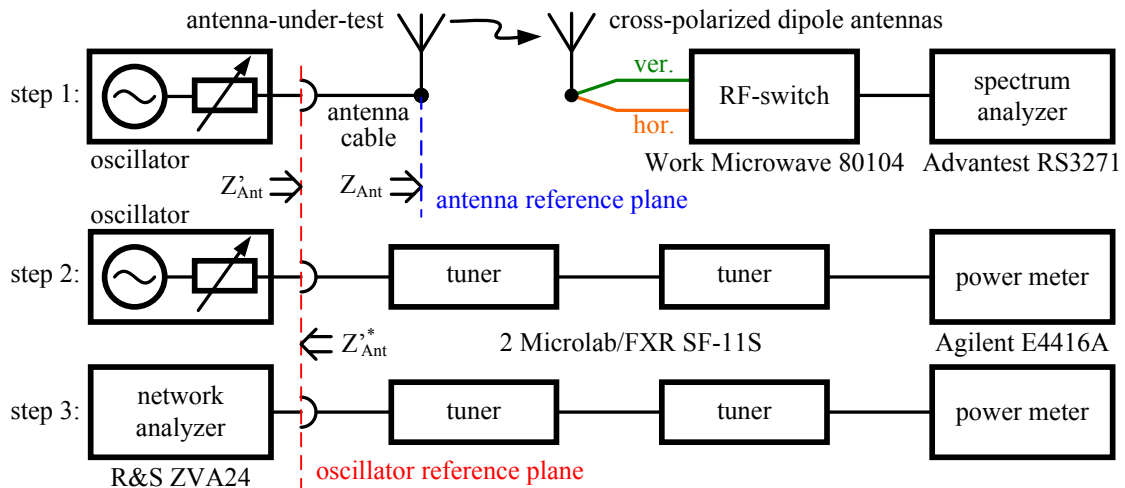


Figure 5.5: Block diagram of the impedance measurement procedure.

impedance can be determined by the following four steps. Figure 5.5 illustrates the measurement procedure.

1. The antenna-under-test with the oscillator attached is mounted in front of two cross-polarized dipole antennas. With the RF-switch the dominant polarization is selected. The power received by the dipole antenna—which is in fact proportional to the power radiated by the device under test—is monitored with a spectrum analyzer. Next, the capacitors C7 and C8 are tuned to maximize the radiated power (source-pull measurement). This is done with a ceramic tuning tool. If the tuning range of the oscillator contains the complex conjugate of the transformed antenna impedance  $Z'_{\text{Ant}}$ , power matching is achieved between oscillator and tag antenna. This means that  $Z'_{\text{Ant}}$  is now provided at the end of the antenna cable or, equivalently speaking, the oscillator provides a source impedance of  $Z'^*_{\text{Ant}}$ .
2. Measurement of the oscillator source impedance can now be done by a load-pull measurement. Therefore, two double slug tuners (SF-11S by Micro-lab/FXR) and a power meter (Agilent E4416A) are connected to the oscillator. The tuners are then set to deliver the maximum power to the power meter. With this, the impedance at the tuner input is equivalent to the transformed antenna impedance  $Z'_{\text{Ant}}$ . Also, the power produced by the oscillator  $P_{\text{out,oscillator}}$  can be determined by considering the losses in the tuners and the cables. This is the power that is delivered to the antenna during the measurement. Later, it is very important for calculating the antenna's efficiency and gain.
3. The input impedance of the tuner  $Z'_{\text{Ant}}$  can now be measured with a vector network analyzer. This load-pull measurement is very accurate because the network analyzer characterizes a passive load. Experiments have shown that direct measurements at the running oscillator by means of a vector network analyzer are inaccurate because the results strongly depend on the test port power.
4. Finally, the antenna cable has to be deembedded to determine the antenna impedance  $Z_{\text{Ant}}$  from the measured impedance  $Z'_{\text{Ant}}$ . This is done with

$$\rho'_{\text{Ant}} = \frac{Z'_{\text{Ant}} - Z_0}{Z'_{\text{Ant}} + Z_0}, \quad \rho_{\text{Ant}} = \rho'_{\text{Ant}} \cdot e^{2\gamma l}, \quad \text{and} \quad Z_{\text{Ant}} = Z_0 \cdot \frac{1 + \rho_{\text{Ant}}}{1 - \rho_{\text{Ant}}} \quad (5.3)$$

where  $\rho_{\text{Ant}}$  and  $\rho'_{\text{Ant}}$  denote the reflection coefficients corresponding to the impedances  $Z_{\text{Ant}}$  and  $Z'_{\text{Ant}}$ ,  $l$  is the cable length and  $\gamma$  is the complex propagation constant of the antenna cable that includes losses and the velocity factor. For the antenna cable a propagation constant of  $\gamma = (0.33 + j26) \frac{1}{\text{m}}$

was determined from a transmission coefficient measurement performed with a vector network analyzer. The reference impedance  $Z_0$  is  $50 \Omega$ .

For testing, the input impedance of a half-wavelength dipole (see Section 5.6) was measured. The result of  $Z_{\text{Dipole}} = (77 - j15) \Omega$  agrees well with the result obtained by simulation in Ansoft HFSS of  $Z_{\text{Dipole, Sim}} = (56 - j15) \Omega$ . Furthermore, the method was successfully used to determine the impedance of the RFID transponder antennas described in Section 3.4.3.

## 5.6 Test measurement

For testing, a half-wavelength dipole made from brass with a bulk conductivity  $\sigma = 15 \cdot 10^6 \text{ S/m}$ , thickness  $d = 6 \text{ mm}$ , length  $l = 156 \text{ mm}$ , nominal input impedance  $Z_{\text{Dipole, Sim}} = (56 - j15) \Omega$ , and center frequency  $f_c = 864 \text{ MHz}$  was measured in an anechoic chamber. To distinguish between horizontal and vertical polarization two cross-polarized dipole antennas were used as pickup antennas. The spectrum analyzer is connected to the pickup antennas' outputs by means of an RF-switch that selects either the horizontal or the vertical polarization. The transmission distance was  $d = 2.88 \text{ m}$  and thus sufficient to be in the far field. The results for the dipole were obtained by conducting the following measurement procedure:

1. Perform the measurement procedure described in Section 5.5 to obtain perfect matching between the oscillator and the dipole-under-test. Furthermore, the available power at the antenna input is determined.
2. Measure the distance  $d$  between the dipole-under-test and the pickup antenna.
3. Connect the oscillator to the dipole-under-test and attach the antenna to the rotation unit.
4. Power up the oscillator and wait for the oscillator signal to be stable (1 minute).
5. Start the automated measurement programm in Matlab. The measurement computer controls the antenna rotation unit, the RF-switch, and the spectrum analyzer and samples a series of power values at the pickup antennas' outputs. The measurements are taken at pre-defined angle increments (e.g.  $\Delta_\varphi = \pi/20$  and  $\Delta_\vartheta = \pi/12$ ).
6. Convert the series of received power levels  $P_{\text{Receive}}$  to the antenna gain  $G_{\text{DUT}}$  according to

$$G_{\text{DUT}} = \frac{P_{\text{Receive}}/G_{\text{Pickup}}}{P_{\text{Out, Oscillator}}} \cdot \left( \frac{4\pi d}{c_0/f} \right)^2. \quad (5.4)$$

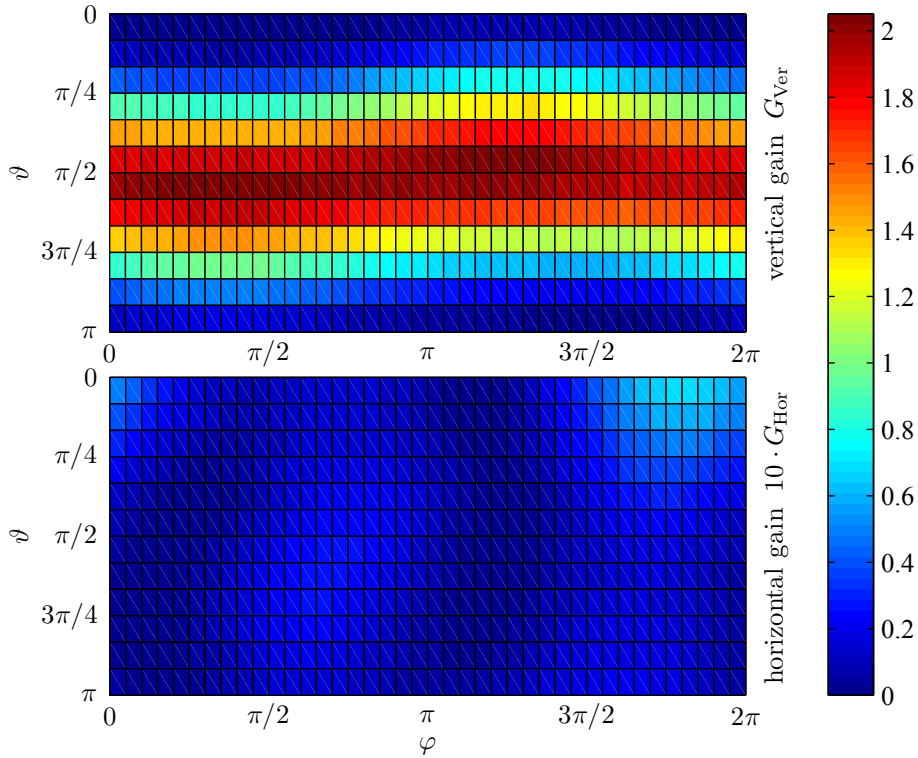


Figure 5.6: Gain pattern of the dipole antenna for horizontal and vertical polarization. The horizontal gain is shown with a magnification of 10.

A pickup antenna with a gain of 6.2 dBi was used. The attenuation of the cables and the RF-switch were determined and considered in  $G_{\text{Pickup,Vor}}$  and  $G_{\text{Pickup,Hor}}$ . From the measured antenna gain for horizontal and vertical polarization versus azimuth and polar angle, the antenna efficiency was calculated. This was done by approximating the integrals with sums in Equation 5.1.

A graphical representation of the antenna gain is given in Figure 5.6. The vertical gain pattern  $G_{\text{Ver}}$  agrees well with the ideal characteristic of a dipole—except for a dependence of the elevation pattern on the azimuth angle  $\varphi$ . In the figure this is identified as a wave-like distortion in the vertical gain pattern. Obviously, the small oscillator attached to the dipole antenna causes a slight tilt of the effective dipole axis by some few degrees. The measured gain for horizontal polarization  $G_{\text{Hor}}$ —that should be zero in theory—results from the tilt of the effective dipole axis as well. Uncertainties caused by imperfect cross polarization capabilities of the pickup antenna or depolarization effects in the chamber seem to be negligible. This is confirmed by the consistent dependence of horizontal and vertical antenna gain on the azimuth angle  $\varphi$ . Please note that for the sake of better perception, the horizontal gain is shown with a *magnification of 10* in Figure 5.6.

Table 5.1 shows the results obtained from the measurement and the corresponding theoretical values (linear scale). It can be seen that the measurement results agree with the theoretical results for an ideal dipole by approximately one decibel. This is a typical accuracy for an antenna gain measurement with reasonable effort.

The systematic errors in this gain measurement are mainly caused by the absolute accuracy of the spectrum analyzer and erroneous attenuation factors of the measurement cables connecting the pickup antenna with the polarization-switch and the spectrum analyzer. Although, the attenuation factors of the cables have been determined by measurement with a network analyzer, the validity of these numbers after running the long cables to the test site is questionable. These issues are typical for gain measurements that basically rely on a measurement of absolute radiant flux density and on Equation 5.4.

To overcome these measurement errors a relative gain measurement that directly compares the device-under-test with a reference antenna by exchanging the antennas in the rotation unit was favored. This measurement setup is illustrated in Figure 5.7. With that procedure the absolute accuracy of the spectrum analyzer and the cable losses cancel during the computation of gain. Nevertheless, horizontal and vertical polarization have to be balanced by a comparative measurement.

For calibration of the relative gain measurement setup, the dipole antenna that was characterized in the earlier measurement is used as a reference antenna. From simulations also considering the losses in the conductors it is seen that this antenna can be considered as an ideal half-wavelength dipole with a gain of 2.15 dBi and an efficiency of 100 %<sup>3</sup>. A dedicated battery powered oscillator similar to the one described in Section 5.4 was permanently attached to the antenna. This unit (Figure 5.8) provides a highly stable reference and allows reproducible measurements on tag antenna prototypes. The calibration of the measurement setup is done by characterizing the reference dipole unit and extracting the parameters of the setup

---

<sup>3</sup>In fact, also with very extensive simulations of the sole dipole, efficiency was still well above 99%.

Table 5.1: Dipole antenna measurement results.

antenna parameter	value	theoretical value
efficiency	133 %	100 %
peak gain	2.05	1.64
cross polarization ratio	102.5	$\infty$

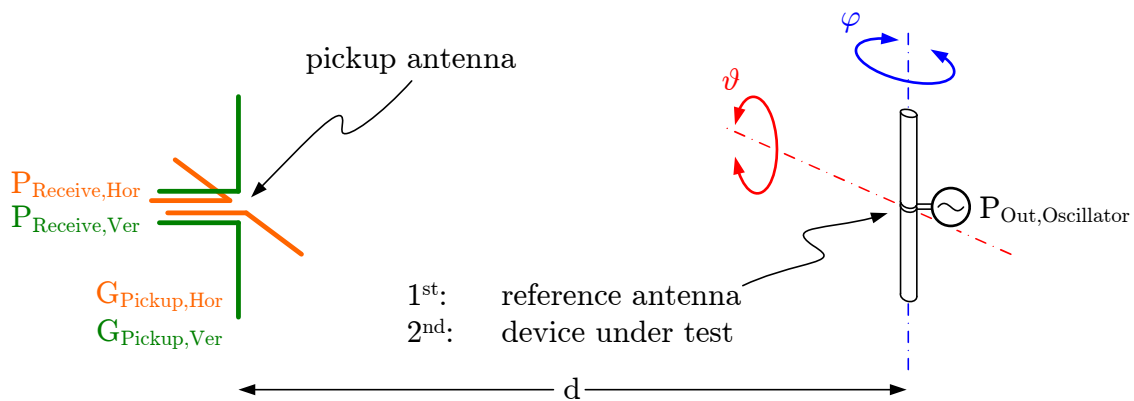


Figure 5.7: Measurement setup for the comparative gain measurement.



Figure 5.8: Half-wavelength reference dipole with the battery powered oscillator (actual size).

from the results. Also balancing the received level of horizontal and vertical polarization can be done with this reference antenna by simply taking two measurements with the dipole aligned horizontally and vertically. The accuracy of the horizontal and vertical polarization with respect to each other is thus in the order of the cross polarization ratio of the reference dipole.

## 5.7 Summary

This work presents a method that allows the characterization of input impedance and gain of small antennas. The critical factors in measuring such autonomously operating antennas without the use of a measurement cable are addressed and a solution approach comprising a small, battery-powered oscillator is presented. The tunable matching network that is contained in the oscillator is a good way to determine the antenna input impedance by a source-pull measurement. Consequently, the perfect matching that is achieved between oscillator and antenna allows accurate gain measurements. A unit that rotates the antenna in both azimuth and elevation allows to obtain a series of gain figures from which the antenna efficiency can be calculated. The verification measurement results for a half-wavelength dipole agree well with the theoretical data. For an even more accurate characterization of transponder antennas the half-wavelength dipole with a dedicated oscillator that is

permanently attached to it is used as a precision reference antenna. Measurements that were carried out within the last two years and in different anechoic chambers were reproducible with an accuracy of some tenth of a dB.

# 6 Impedance measurement method for transponder chips

In this Appendix a method is presented to perform accurate measurements on passive RFID transponder chips in the UHF band. The chip samples were extracted from commercially available RFID tag inlays. I determine the minimum operating power necessary to get a response from the transponder chip. Furthermore, I measure the chip input impedance in both, the reflecting and the absorbing state as a function of input power. Measurement results of four transponder chips are presented and good agreement with values claimed in the manufacturer's data sheets is found. At the end of the chapter conclusions are drawn for the optimum antenna design and for the link budget.

## Original publications related to this chapter

L. W. Mayer and A. L. Scholtz, "Sensitivity and impedance measurements on UHF RFID transponder chips," in *Proc. The Second International EURASIP Workshop on RFID Technology*, (Budapest, Hungary), Jul. 2008.

## 6.1 Motivation

The main tasks in designing passive RFID transponders that operate in the UHF band are

- the development of a transponder chip that uses a rectifier to turn an RF signal into the supply voltage for the built-in logic, and
- the design of an appropriate antenna that is matched to the chip and can cope with the environment that is given by the application.

The typical input impedance of passive state-of-the-art UHF transponder chips is highly reactive (e.g.  $Z_{\text{Chip}} \approx (28 - 180j) \Omega$ ) which is a result from technological aspects and efficient RF-rectifier design. In a conventional impedance measurement, the chip is directly connected to the  $50 \Omega$  system of a VNA (vector network analyzer) [87]. As a result the VSWR (voltage standing wave ratio) at the chip input is by far larger than 10:1 which leads to inaccurate results for the input impedance.

Besides the input impedance, the power accepted by the transponder chip is of high interest, first and foremost to obtain the minimum operating power. In a conventional test setup, the accepted power could in principle be calculated from the VNA's source power and the reflection coefficient determined by the VNA. But, foregoing measurements showed that, at high VSWR, any inaccuracy of the measured reflection coefficient has a particularly strong impact on the accepted power determined in this way.

It is common practice that modulated backscattering by the transponder chip is achieved by changing its input impedance. Depending on the modulation scheme and the data rate used in the transmission, a switching between two impedance states is done with a rate up to 640 kHz. This makes separate measurement of the corresponding input impedances particularly difficult.

Finally, causing the chip to respond requires a carrier that is modulated with a command sequence—a feature which, to the knowledge of the author, is not provided by any VNA available on the market.

To attain accurate results for both power and impedance, that are useful for the antenna designer on the one hand and for the chip designer on the other hand, I developed a new measurement method. In Section 6.2 this pre-matched impedance test setup is described that allows to operate and characterize transponder chips as if they were directly connected to an antenna. Impedance tuners are used to transform the port impedance of a VNA to a desired antenna impedance. A set of custom built impedance standards is used to calibrate the setup and a dedicated test fixture holds the transponder chip during characterization (Section 6.3). An external signal source provides a carrier modulated with a command sequence that causes the transponder chip to respond. The sequence which is compliant to the EPCglobal Gen2 UHF RFID Protocol Standard [4] is described in Section 6.4. With an exemplary measurement presented in Section 6.5, it is shown how the input impedance of a transponder chip is obtained. This is done at a carrier frequency of 866 MHz which is within the frequency band dedicated to RFID systems in Europe. Section 6.6 elaborates on the relation between chip input impedance and operating power. The delta gamma value of the transponder chip, which is often given in data sheets, and the strength of the signal reradiated by the transponder are analyzed in Section 6.7. At the end of this chapter, in Section 6.8, a comparison of some

transponder chips is presented. In Section 6.10 conclusions are drawn for the radio link budget and for the optimum antenna design which are considered useful for chip and antenna designers.

## 6.2 Chip test setup

This section describes the test setup and measurement procedure that was developed to characterize and compare the tag chips.

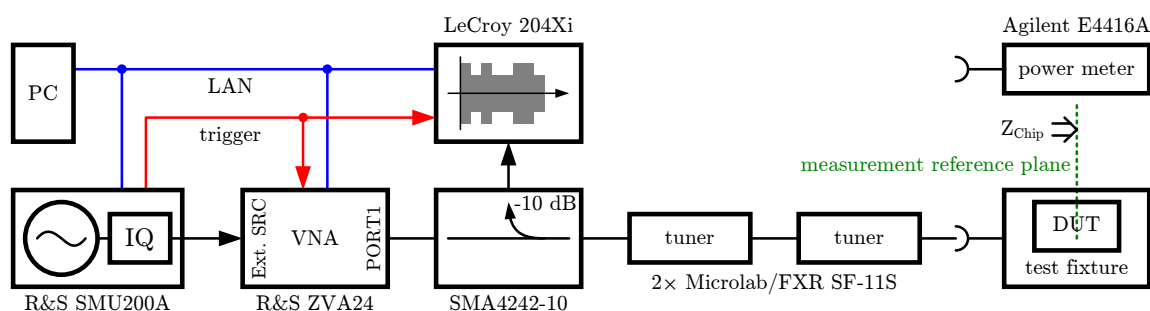


Figure 6.1: Block diagram of the measurement setup used to characterize the transponder chips.

The measurement setup depicted in Figure 6.1 consists of the following components:

- The **tag chip** mounted in the test fixture (DUT).
- The **vector signal generator** (R&S SMU200A) that provides a signal that is modulated with the wake-up sequence. Output power and timing parameters are controlled by the measurement computer. The carrier frequency of the signal is 866 MHz.
- The **vector network analyzer** (R&S ZVA24) determines the impedance of the transponder chip. The wake-up sequence is provided by using the signal generator as an external source for the VNA. After the command, a series of impedance measurements is triggered to measure the chip impedance in both, the absorbing and the reflecting state. The real and the imaginary part of the impedance can be shown versus time.
- Two **impedance tuners** (Microlab/FXR SF-11S) provide static pre-matching [88] between the  $50\ \Omega$  output of the VNA and the tag chip. This means that if the chip is in absorbing mode (equivalently speaking: if the chip does not try to reflect power) all available power is provided to the

rectifier and no power is returned<sup>1</sup>. Firstly, this allows direct adjustment of the power accepted by the chip, and secondly, the pre-matching transforms the transponder chip impedance into the  $50\ \Omega$  system impedance. This enables a more accurate impedance measurement due to lower VSWR at the VNA input. Moreover—since the tuners provide the complex conjugate chip impedance  $Z_{\text{Chip1}}^*$  which is in fact the optimum antenna impedance—the measurement is equivalent to one with an antenna that is perfectly matched to the chip. The calibration of the VNA is done after pre-matching with the impedance tuners. Pre-matching is adjusted at the minimum operating power.

- The **directional coupler** (Narda SMA4242-10) separates the power returned by the tag chip from the source power. Firstly, this is necessary to find the optimum setting of the impedance tuners by minimizing the returned power. Secondly, the returned signal can be displayed on the
- **oscilloscope** (LeCroy Waverunner 204Xi) which is connected to the output of the directional coupler. A backscattered signal from the tag chip can thus be clearly identified.
- A **computer** is used to interface the oscilloscope, the VNA and the vector signal generator. This allows to control the experiments by the use of Matlab scripts and helps to find and compare characteristics of the transponder chips, to perform parameter sweeps, and to visualize results.
- The **power meter** (Agilent E4416A) to calibrate the available power at the chip input. This is done by replacing the DUT with the probe, adjusting the impedance tuners to match, and read the power  $P_{\text{Available}}$ . Since the tuner's insertion loss is practically independent on the tuner's setting,  $P_{\text{Available}}$  is equivalent to the available power at the chip input in a subsequent chip measurement.

### 6.3 Chip test fixture

For characterization, a test fixture was designed that allows precisely reproducible measurements of input impedance and backscattering behavior. For calibration of the VNA, three dedicated test fixtures were used as calibration standards. The match- and short-standards were equipped with a  $49.9\ \Omega \pm 1\%$  and a  $0\ \Omega$  resistor, respectively, while the open-standard was left empty. Using the  $49.9\ \Omega$  resistor as a calibration standard is not optimal for calibrating the test setup. More

---

<sup>1</sup>Strictly speaking this only holds for the fundamental frequency. Due to the fact that the chip rectifier is a nonlinear load, some power will be returned at harmonic frequencies.

accurate calibration in a pre-matched setup is achieved when a match-standard, that minimizes reflections at the load is used. For the measurements performed here, a match-standard with an impedance close to that of the transponder chips (e.g.  $Z_{\text{Match}} = (28 - 180j) \Omega$ ) would have been favored. Some such standards were created using surface mount resistors and capacitors. In a series of experiments where one chip was characterized in the test setup that was calibrated with each of the different match-standards built, it was found that the measurement results were highly dispersive. This inaccuracy was traced back to production tolerances of the lumped circuit elements—especially of the capacitors. The idea of generating better match-standards was so dismissed.

The parameters of the three standards used during the calibration process were verified by measurement [89, 90]. Due to the relatively low frequency of 866 MHz and the small dimensions of the calibration standards, the parameters of the kit emerged very closely to the expected values in terms of impedance and electrical offset. The author is aware that a more accurate measurement of the chips' input impedances would have been possible with a TRL<sup>2</sup> calibration. But, with the TRL calibration, the reference impedance for the reflection measurement is equivalent to the transmission line impedance leading to the chip. Thus, a tunable pre-matched test setup where a complex reference impedance is used can hardly be applied and consequently, the investigation of neither the reflected signal like shown in Section 6.5, nor the minimum operating power like shown in Section 6.6 can be accomplished. It is obvious that some accuracy of the chip impedance measurement was compromised, but in return this setup allows to accurately determine the absolute available power and to record the switching between the input impedance states.

For characterization, the chip with a small rest of its connection to the antenna was cut out of the RFID transponder inlay. The antenna connections were exposed, cleaned, and then glued to the test fixture with electrically conducting adhesive (Loctite 3880). A photograph of the calibration kit and of a test fixture holding a transponder chip that was extracted from a UHF tag is shown in Figure 6.2.

---

<sup>2</sup>TRL (through-reflect-line) calibration represents a family of calibration techniques that measure two transmission standards and one reflection standard to determine the 2-port 12-term error coefficients.

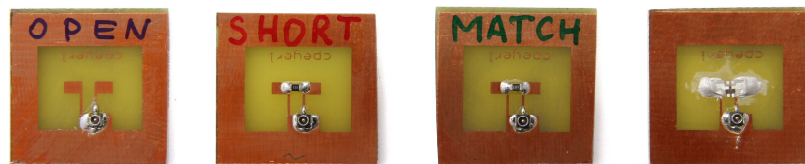


Figure 6.2: Photograph of the calibration kit and the test fixture used for the measurement of chips extracted from RFID tags (actual size). The measurement cable is connected via a small surface mounted coaxial connector.

## 6.4 Wake-up sequence

Waking up the transponder chips—according to the EPCglobal Gen2 Standard—was done using an inventory command. The inventory command sequence was generated in Matlab and sent to a vector signal generator (R&S SMU200A) as IQ baseband samples. This allows to change the sequence quickly and to perform parametric sweeps.

The envelope of the wake-up signal is shown in Figure 6.3, a list of the parameters with their meaning, standard compliant value, and chosen value is given in Table 6.1. The inventory command (0x200010) sent to the chip requests an answer using the FM0 modulation scheme which provides the highest possible data rate.

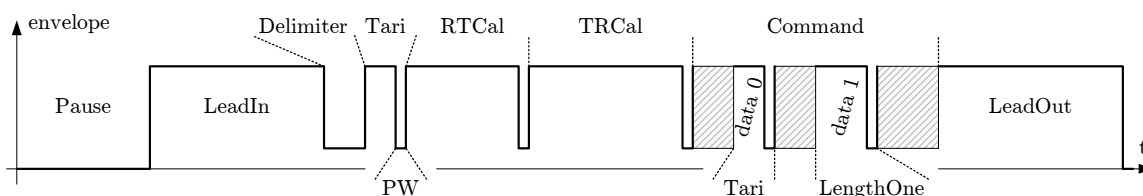


Figure 6.3: Envelope of the wake-up sequence used to cause the transponder chip to respond.

Table 6.1: Parameters of the wake-up sequence.

parameter	meaning	range in standard	value used
Pause	power switched off	-	4 ms
LeadIn	power on before command	$\leq 2$ ms	2 ms
Delimiter	start of frame	$12.5 \mu\text{s} \pm 5\%$	$12.5 \mu\text{s}$
Tari	duration of a data 0 symbol	$6.25 \mu\text{s} .. 25 \mu\text{s}$	$25 \mu\text{s}$
PW	pulse width	$(0.265 .. 0.525)$ Tari	$0.265$ Tari
RTCal	R $\Rightarrow$ T calibration	$(2.5 .. 3)$ Tari	$2.75$ Tari
TRCal	T $\Rightarrow$ R calibration	$(1.1 .. 3)$ RTCal	$2$ RTCal
LengthOne	duration of a data 1 symbol	$(1.5 .. 2)$ Tari	$1.75$ Tari
Command	binary command code	dep. on modulation	0x200010
LeadOut	power on after command	-	1 ms
ModDepth	modulation depth	90 %	90 %

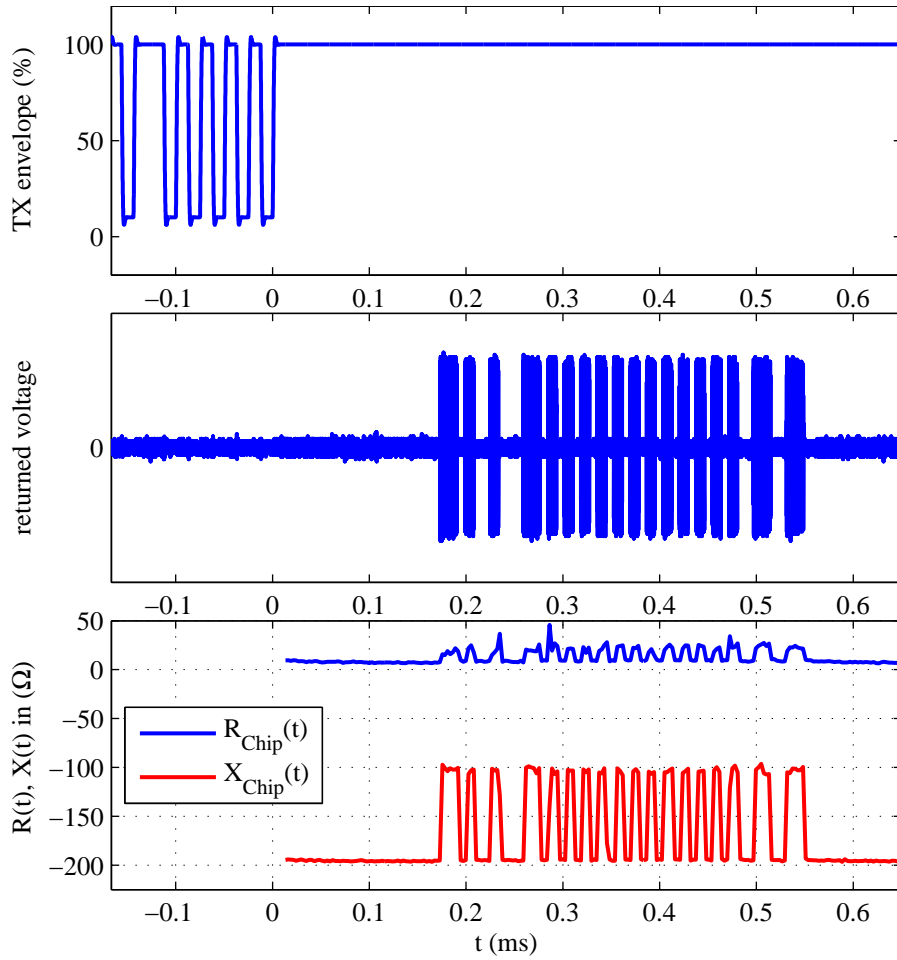


Figure 6.4: Signals during measurement of chip A operated at minimum operating power level ( $-6$  dBm).

Top: Envelope of the signal sent to the transponder chip. The end of the inventory command can be seen on the left at  $t = 0$ .

Middle: Returned voltage at the transponder chip measured with the oscilloscope. The mismatch caused by modulation of the chip's input impedance generates a reflected signal.

Bottom: Chip input impedance versus time. During response, the impedance of the chip is switched between the two states  $Z_{\text{Chip1}}$  and  $Z_{\text{Chip2}}$ .

## 6.5 Impedance measurement

In this section I present measurement results of four different transponder chips. The four chips that were characterized are denoted by the letters A to D. Figure 6.4 shows representative signals sampled during characterization of chip A. An 866 MHz carrier signal with an envelope power of  $-6$  dBm was applied to the chip input. This carrier signal was modulated with the wake-up sequence. In the top graph of Figure 6.4, the envelope of the signal sent to the chip is plotted. At  $t = 0$ , the inventory command ends and the chip starts processing the received data. Since the modulator in the chip is off, the input impedance of the rectifier loaded with the chip's logic can be measured. I refer to this impedance as the absorbing impedance  $Z_{\text{Chip1}}$ . While in this state, no power is reflected at the chip input. The reason for this is, that the tuners were set to provide the complex conjugate chip input impedance  $Z_{\text{Chip1}}^*$ . In fact, the tuner's output can be seen as an antenna which is perfectly matched to the chip's absorbing impedance.

In the center graph of Figure 6.4, the reflected wave is plotted. While the chip is still processing the data—thus presenting  $Z_{\text{Chip1}}$ , the reflected signal is close to zero. When the chip responds to the inventory command, it changes its input behavior by—for example—switching on a shunt transistor. This destroys the matching condition and causes a strong reflected signal. The pattern of this signal is controlled by the internal logic of the transponder chip.

From  $t = 0$  on, the VNA takes a series of measurements to determine the chip's input impedance versus time. The result can be seen in the bottom drawing of Figure 6.4. At  $t = 0.17$  ms the input impedance changes to a new value. I will refer to this impedance as the reflecting impedance  $Z_{\text{Chip2}}$ . From the measured values  $Z_{\text{Chip1}} = (8.3 - 195.2j) \Omega$  and  $Z_{\text{Chip2}} = (22.3 - 103.8j) \Omega$ , it can be inferred that a shunt transistor that is in parallel to a capacitor is switched on and off during modulation.

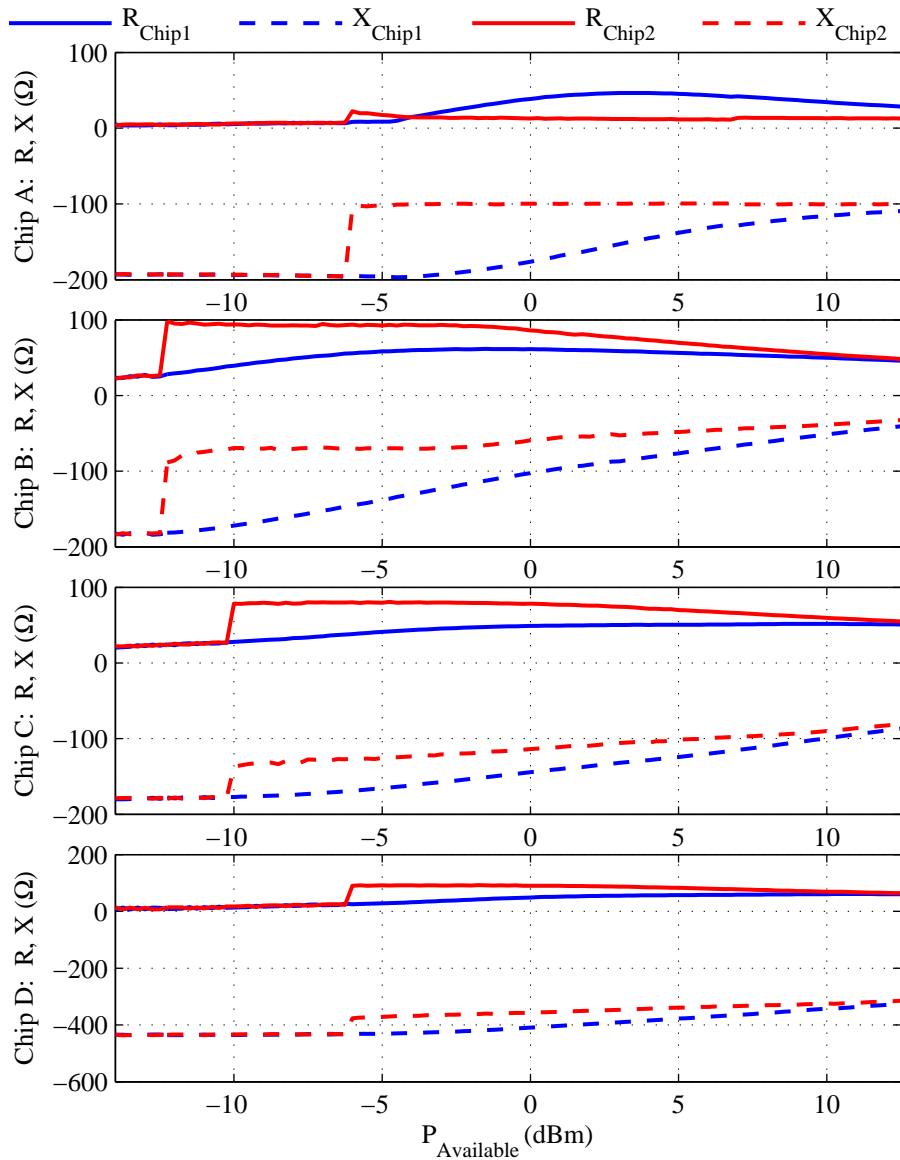


Figure 6.5: Measured real and imaginary parts of absorbing impedance  $Z_{\text{Chip1}}$  and reflecting impedance  $Z_{\text{Chip2}}$  of the characterized transponder chips versus power.

## 6.6 Power sweep

A power sweep was performed to determine the operating range of the transponder chips. Therefore, for every power step where a response was detected, the

input impedances  $Z_{\text{Chip1}}$  and  $Z_{\text{Chip2}}$  were measured. Figure 6.5 shows the results for the tested chips. Looking at the sweep for chip A, the minimum operating power—or equivalently speaking the sensitivity—is  $P_{\text{Min}} = -6$  dBm. The impedance  $Z_{\text{Chip1}}$  measured at  $P_{\text{Min}}$  can be used to determine the optimum antenna impedance for best power matching ( $Z_{\text{Ant,Pwr}} = Z_{\text{Chip1}}^*$ ). With increasing power the input impedances change quite significantly. At low power this is because of the nonlinear characteristics of the rectifier. At higher power levels, the absorbing impedance  $Z_{\text{Chip1}}$  converges to the reflecting impedance  $Z_{\text{Chip2}}$ . The reason for this is that the shunt transistor is deliberately turned on, even if the chip is in absorbing mode. This is done to regulate the internal supply voltage of the chip’s logic circuitry. Please note that the setting of the tuners remains unchanged during the power sweep. This is very realistic because an antenna connected to the transponder chip would also provide a constant impedance regardless of the available power.

## 6.7 Efficiency of backscattering

The efficiency of backscattering is determined by the reradiated signal when the transponder chip switches between the absorbing and the reflecting mode. A mathematical formulation of the backscattered signal strength as a function of  $Z_{\text{Chip1}}$ ,  $Z_{\text{Chip2}}$ , and  $Z_{\text{Ant}}$  was given in Section 2.3. Table 6.2 summarizes the chip impedance values measured at each chip’s minimum operating power  $P_{\text{Min}}$ . Furthermore, the antenna impedance  $Z_{\text{Ant,Mod}}$  that maximizes the reradiated power (Equation 2.11) is given. With this antenna impedance, the transponder chips provide their maximum modulation efficiency  $\eta_{\text{Mod,Max}}$  (Equation 2.14). On the other hand  $Z_{\text{Ant,Mod}}$  does not provide perfect power matching between antenna and chip. The penalty for choosing  $Z_{\text{Ant,Mod}}$  instead of  $Z_{\text{Chip1}}^*$  is expressed as the matching loss factor  $r_{\text{Mismatch}}$  (Equation 2.13). Particularly, from the numbers obtained for chip A, it is seen that high modulation efficiency comes at the cost of power matching. In fact, chip A requires by 3.6 dB more available antenna power than its  $P_{\text{Min}}$ . It can be followed from the results in Table 6.2, that for the characterized chips there are quite big differences in the achievable modulation efficiency.

It is a widely held belief that reradiated power is directly related to the delta gamma value of a transponder chip. The delta gamma value is defined by  $\Delta\Gamma = |\Gamma_{\text{Chip1}} - \Gamma_{\text{Chip2}}|$  where  $\Gamma_{\text{Chip1}}$  and  $\Gamma_{\text{Chip2}}$  denote the complex reflection coefficients corresponding to  $Z_{\text{Chip1}}$  and  $Z_{\text{Chip2}}$ , respectively.  $\Delta\Gamma$  is a measure for the distance between the reflecting and the absorbing impedance measured in a Smith chart. In the following, it is shown that high delta gamma values do not necessarily result in a stronger reradiated signal. The reradiated power can rather be determined

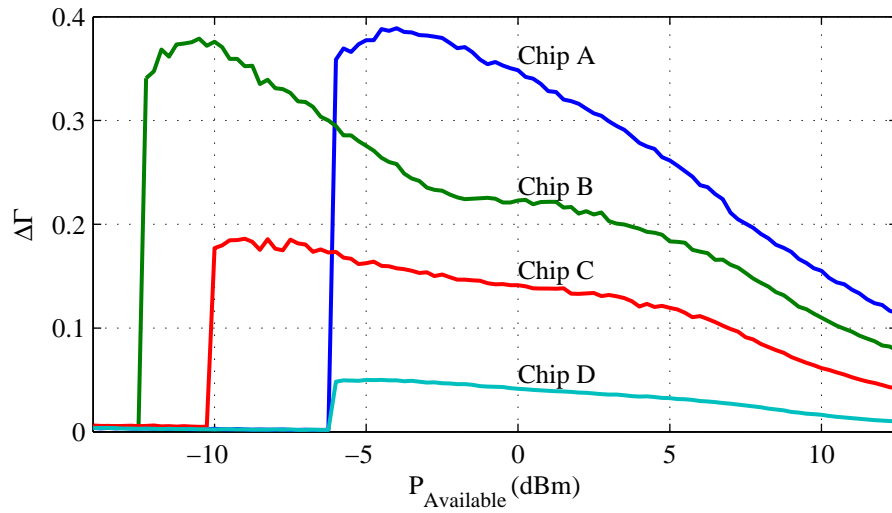
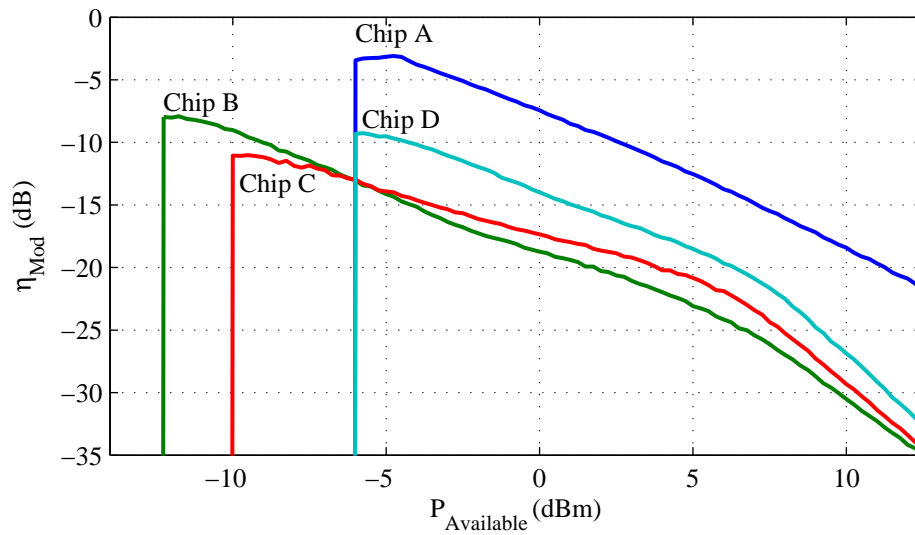
Table 6.2: Input impedances  $Z_{\text{Chip1}}$  and  $Z_{\text{Chip2}}$ , return-link optimized antenna impedance  $Z_{\text{Ant,Mod}}$ , maximum modulation efficiency  $\eta_{\text{Mod,Max}}$ , and matching loss factor  $r_{\text{Mismatch}}$  of the characterized transponder chips.

chip	$Z_{\text{Chip1}}$	$Z_{\text{Chip2}}$	$Z_{\text{Ant,Mod}}$	$\eta_{\text{Mod,Max}}$	$r_{\text{Mismatch}}$
A	$(8 - 195j) \Omega$	$(22 - 104j) \Omega$	$(43 + 170j) \Omega$	-3.4 dB	-3.6 dB
B	$(28 - 181j) \Omega$	$(98 - 89j) \Omega$	$(65 + 161j) \Omega$	-8.0 dB	-1.0 dB
C	$(28 - 177j) \Omega$	$(78 - 137j) \Omega$	$(50 + 167j) \Omega$	-11.1 dB	-0.4 dB
D	$(25 - 432j) \Omega$	$(90 - 377j) \Omega$	$(53 + 420j) \Omega$	-9.3 dB	-0.7 dB
e.g. Sec. 2.4	$(28 - 179j) \Omega$	$(88 - 113j) \Omega$	$(57 + 163j) \Omega$	-9.2 dB	-0.7 dB

by Equation 2.10. However the delta gamma value is often found in data sheets and will be used here to merely explain the input characteristics of transponder chips.

As a consequence from the measurement results of  $Z_{\text{Chip1}}$  and  $Z_{\text{Chip2}}$  shown in Figure 6.5, the delta gamma values converge to zero for high power levels. Figure 6.6 shows the delta gamma values of chip A to chip D versus power. It is interesting to note that for chip A, the delta gamma value starts from  $\Delta\Gamma_{\text{Min}} = 0.36$  at  $P_{\text{Available}} = -6$  dBm and peaks at  $\Delta\Gamma_{\text{Max}} = 0.39$  at  $P_{\text{available}} = -4$  dBm. Similar behavior can also be seen for chip B. I suppose that this is due to the internal supply voltage which is not sufficient to exceed the threshold voltage of the shunt transistor at low power levels. The slight decrease in the real part of the reflecting impedance  $\text{Re}(Z_{\text{Chip2}})$  at low power seen in Figure 6.5 is likely caused by an increasingly conducting shunt transistor as well and confirms this assumption.

Figure 6.7 shows the modulation efficiency obtained for the tested transponder chips versus power. For each chip, the antenna impedance  $Z_{\text{Opt,Mod}}$  (Equation 2.11) that maximizes the reradiated signal was calculated. Therefore, the chip impedance values  $Z_{\text{Chip1}}$  and  $Z_{\text{Chip2}}$  measured at  $P_{\text{Min}}$  were used. It can be seen in Figure 6.7 that chip A provides best modulation efficiency of  $\eta_{\text{Mod,Max}} = -8.4$  dB. It should be noted that chip D—which shows the lowest delta gamma value—performs quite well when considering the reradiated power. This plot of the modulation efficiency is very useful to rate and compare the performance of transponder chips. It shows the minimum operating power level and the strength of the reradiated signal. In a return-link limited system, for instance, Chip A would be advantageous because its high modulation efficiency provides a very strong signal at the receiver. In a forward-link limited system one would rather go for chip B which has highest sensitivity ( $P_{\text{Min}} = -12.25$  dBm).

Figure 6.6: Delta gamma  $\Delta\Gamma$  versus power.Figure 6.7: Modulation efficiency  $\eta_{\text{Mod}}$  versus available power.

## 6.8 Comparison of the results with manufacturer's data sheets

In this section a comparison of the four different transponder chips that were available to the author is given. Only one chip of each kind was characterized. The results are thus influenced by production tolerances. Table 6.3 summarizes minimum operating power, input impedances, and delta gamma values. The results for the input impedance  $Z_{\text{Chip1}}$  of chip B and chip C agree well with the values claimed in the manufacturer's data sheet. For chip A and chip D no data sheets were available.

Table 6.3: Comparison of the transponder chips. The index *Min* relates to the minimal power where a response from the chip is still detected. *DS* denotes the value claimed in the data sheet.  $\Delta\Gamma_{\text{Max}}$  relates to the maximum delta gamma value measured.

chip	$P_{\text{Min}}$	$P_{\text{Min,DS}}$	$Z_{\text{Chip1,Min}}$	$Z_{\text{Chip1,Min,DS}}$	$\Delta\Gamma_{\text{Min}}$	$\Delta\Gamma_{\text{Max}}$
A	-6.00 dBm	-	$(8 - 195j) \Omega$	-	0.36	0.39
B	-12.25 dBm	-14.00 dBm	$(28 - 181j) \Omega$	$(26 - 204j) \Omega$	0.34	0.38
C	-10.00 dBm	-9.00 dBm	$(28 - 177j) \Omega$	$(23 - 161j) \Omega$	0.18	0.19
D	-6.00 dBm	-	$(25 - 432j) \Omega$	-	0.05	0.05

Table 6.4: Peak envelope power levels used for the five transponder chip variants during the delimiter sweep.

tag chip	envelope power level
chip 1	-5.6 dBm
chip 2	-5.3 dBm
chip 3	-5.1 dBm
chip 4	-4.3 dBm
chip 5	-3.0 dBm

## 6.9 Parameter sweeps

With this measurement method some aspects of the standard conformity and reliability of transponder chips can be tested. One of these measurements was a parameter sweep over the delimiter length. The chips tested were some manufactured design variants supplied by Infineon Technologies Austria AG. For every delimiter length the transponder chips were hit with an inventory command 50 times. For each try the returned voltage was scanned for a response. With this, a reliability plot was generated. Figure 6.8 shows the result of the parameter sweep for delimiter values between  $10\ \mu\text{s}$  and  $14\ \mu\text{s}$ . The measurement was carried out at a frequency of  $f = 866\ \text{MHz}$ . For each prototype, the minimum envelope power that causes a response was determined separately. For the measurement, this power was then raised by half a dB to avoid failure because of temperature drift. Table 6.4 summarizes the power levels used for characterizing the chips. These peak envelope power levels were measured at the test fixture input.

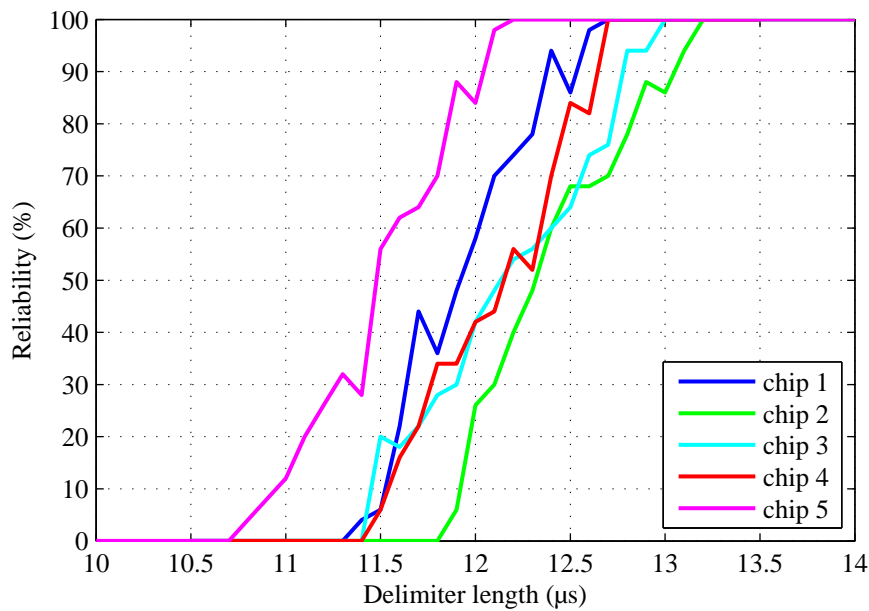


Figure 6.8: Reliability plot for a parameter sweep over the delimiter length for some transponder chip prototypes. Chip 5 reliably answers when hit with a standard compliant inventory command with a delimiter length of  $12.5\ \mu\text{s}$ .

## 6.10 Summary

A measurement method was developed that allows to accurately determine minimum operating power and input impedance of transponder chips. For testing, I characterized and compared some chips that were extracted from commercially available tag inlays. The obtained quantities are in good agreement with the manufacturer's data sheets.

From the measurement results, it is seen that there are quite big differences between the transponder chips. Minimum operating power ranges between  $-6$  dBm and  $-12.25$  dBm. Maximum values for the modulation efficiency range from  $-11.1$  dB to  $-3.4$  dB, which makes an offset of approximately 7.7 dB in a link budget. It is found that some of the characterized chips can bring significant improvement for forward-link limited systems, while others are better used in return-link limited systems. Among the four tested samples, there is no chip that outperforms all others in both sensitivity and modulation efficiency.

Furthermore, the transponder chips show quite different input impedance values and definitely require separate antenna designs. I suppose that the differences between the tag chips are mostly due to technological advances in chip manufacturing and optimization of integrated rectifier circuits during the last years.

## 7 Conclusion

At the time of writing, commercially available RFID systems did neither make use of the state of knowledge about antennas and propagation nor did they apply the techniques in advanced radio frequency frontend design or digital signal processing that have been used for more than a decade in mobile communications. In this work I applied my expertise in antenna design and radio propagation to the current challenges of RFID systems and present findings that allow advantage to be taken of the above mentioned techniques.

The interaction between a transponder chip and a transponder antenna is analyzed by a merely theoretical approach. By using the fundamental theorem of antenna scattering, an optimum antenna impedance is derived that maximizes the signal power reradiated by the tag. By a numerical example, it is shown that the transponder designer can choose between power matching for a forward-link limited system or maximum reradiated power for a return-link limited system. Although the trade-off is not particularly pronounced for today's transponder chips, it will have significant influence in the future, where chip input circuitry will be improved. The findings are also applied to compare some commercially available transponder chips. It is found that some of the tested chips will enhance the performance of forward-link limited systems, while others are better used in return-link limited systems. A separate chapter describes the method that was specifically developed to determine the input characteristics of transponder chips.

The art of transponder antenna design is advanced by a new dual-band transponder antenna that allows operation in both the HF and the UHF band. Since the propagation characteristics in these two bands are very different, a substantial improvement in reliability is expected from a dual-band RFID system that utilizes this antenna. Difficulties emerged during the characterization of gain and input impedance of the produced prototypes. Measurement accuracy was impaired by induced currents along the antenna measurement cable. These errors are particularly pronounced when characterizing electrically-small and low-directive antennas. Additionally, the highly reactive input impedance necessary for optimal interaction between the transponder antenna and the transponder chip complicates power matching essential for an antenna efficiency measurement. To solve these problems a new measurement procedure was designed that utilizes a small, highly-stable, battery-powered, and impedance-tunable oscillator directly mounted to the antenna. With

this signal source a measurement cable is avoided which allows the transponder antenna to operate autonomously. A verification measurement of a dipole showed that the measurement accuracy is better than 1 dB. Measurements done on some dual-band antenna variants helped optimize the antenna structure and revealed the performance penalty caused by the dual-band design. The method is also appropriate to determine changes in the directional pattern, efficiency, and input impedance of an antenna that is subject to a proximity effect.

For UHF interrogator devices a new antenna was invented that solves the long-standing problem of receiver blocking. The antenna features two separate ports, one for transmitting and one for receiving circularly polarized waves. The key feature of the antenna is a very high separation between the transmitted and the received signal—a property which can alternatively be obtained by costly RF front-end hardware only. With adaptive tuning of a directional coupler integrated into the antenna, the carrier signal leaking into the receiver is significantly reduced. The antenna also cancels received signals caused by reflecting objects in space. Measurements showed that the transmit to receive separation is well above 52 dB in a time variant scenario where transponders pass the antenna on a conveyor belt. The antenna only introduces losses of approximately 1 dB while transmitting and receiving. It is also possible to fit a low-noise amplifier directly at the receive output of the antenna. This improves the receivers noise figure in comparison to conventional systems, where a low-noise amplifier can only be applied after the carrier suppression circuitry.

**Additional note of the author** Since the power required to operate transponder chips was rapidly decreased during recent years, it is obvious that future UHF RFID systems tend to be return-link limited. I therefore consider the derivation of the optimum antenna impedance for maximum backscattered power the most important contribution of this work. However, adjustment of the antenna for a particular chip is a first step, but an ongoing task is to formulate optimization criteria for the transponder chip impedances itself. Chip designers can then develop modulation circuitry that further increase the power backscattered by RFID transponders. Here, performance can be improved at relatively low costs.

# Bibliography

- [1] *Identification Cards - Contactless Integrated Circuit(s) Cards - Vicinity Cards - Part 1: Physical Characteristics*, ISO/IEC Std. 15693-2:2006, 2000.
- [2] *Information Technology AIDC Techniques - RFID for Item Management - Air Interface, Part 3 - Parameters for Air Interface Communications at 13.56 MHz*, ISO/IEC Std. 18000-3:2008, 2002.
- [3] *Information Technology - Radio Frequency Identification (RFID) for Item Management - Part 6: Parameters for Air Interface Communications at 860-930 MHz*, ISO/IEC Std. 18000-6:2004, 2002.
- [4] *EPC Radio-Frequency Identity Protocols Class-1 Generation-2 UHF RFID Protocol for Communications at 860 MHz - 960 MHz Version 1.2.0*, EPCglobal, Mar. 2007.
- [5] *Information Technology - Radio Frequency Identification for Item Management - Part 6: Parameters for Air Interface Communications at 860 MHz to 960 MHz AMENDMENT 1: Extension with Type C and Update of Types A and B*, ISO/IEC 18000-6:2004 AMD 1:2006, 2002.
- [6] V. G. Welsby, *The Theory and Design of Inductance Coils*. John Wiley and Sons, Inc., 1960.
- [7] F. W. Grover, *Inductance Calculations Working Formulas and Tables*. Dover Publications, Inc., New York, 1946.
- [8] —, “The calculation of the mutual inductance of circular filaments in any desired positions,” *Proceedings of the IRE*, pp. 620–629, Oct. 1944.
- [9] R. Escovar, S. Ortiz, and R. Suaya, “An improved long distance treatment for mutual inductance,” *IEEE Trans. Computer-Aided Design*, vol. 24, no. 5, pp. 783–793, May 2005.
- [10] —, “Mutual inductance between intentional inductors: closed form expressions,” in *Proc. Circuits and Systems*, pp. 2448–2452, Sep. 2006.
- [11] S. Hackl, C. Lanschutzer, P. Raggam, and W. L. Randeu, “A novel method for determining the mutual inductance for 13.56 MHz RFID systems,” in *Communication Systems, Networks and Digital Signal Processing*, pp. 297–300, Aug. 2008.
- [12] Microchip Technology Inc., *Antenna circuit design for RFID applications*, 2003.
- [13] S. C. Q. Chen and V. Thomas, “Optimization of inductive RFID technology,” in *Proc. IEEE International Symposium on Electronics and the Environment*, pp. 82–87, Jul. 2001.
- [14] K. Finkensteller, *RFID handbook*, 2nd ed. John Wiley & Sons, 2003.
- [15] C. Floerkemeier and M. Lampe, “Issues with RFID usage in ubiquitous computing applications,” *Lecture Notes in Computer Science*, vol. 3001/2004, pp. 188–193, 2004.

- [16] H. Hertz, “Die Kräfte elektrischer Schwingungen behandelt nach der Maxwellschen Theorie,” *Annalen der Physik und Chemie*, vol. 36, pp. 1–22, 1889.
- [17] H. A. Wheeler, “Fundamental limitations of small antennas,” *Proceedings of the IRE*, vol. 35, no. 12, pp. 1479–1484, Dec. 1947.
- [18] A. A. M. Saleh and R. A. Valenzuela, “A statistical model for indoor multipath propagation,” *IEEE J. Select. Areas Commun.*, vol. SAC-5, no. 2, pp. 128–137, Feb. 1987.
- [19] T. S. Rappaport and C. D. McGillem, “UHF fading in factories,” *IEEE J. Select. Areas Commun.*, vol. 7, no. 1, pp. 40–48, Jan. 1989.
- [20] L. W. Mayer, M. Wrulich, and S. Caban, “Measurements and channel modelling for short range indoor UHF applications,” in *Proc. The First European Conference on Antennas and Propagation*, Nice, France, Oct. 2006. [Online]. Available: [http://publik.tuwien.ac.at/files/pub-et\\_11470.pdf](http://publik.tuwien.ac.at/files/pub-et_11470.pdf)
- [21] A. Paulraj, R. Nabar, and D. Gore, *Introduction to Space-Time Wireless Communications*. Cambridge University Press, 2006.
- [22] D. M. Dobkin and S. M. Weigand, “Environmental effects on RFID tag antennas,” in *Proc. IEEE MTT-S International Microwave Symposium Digest*, Jun. 2005.
- [23] R. H. Clarke, D. Twede, J. R. Tazelaar, and K. K. Boyer, “Radio frequency identification (RFID) performance: the effect of tag orientation and package contents,” *Packaging Technology and Science*, vol. 19, pp. 45–54, 2006, John Wiley & Sons, Ltd.
- [24] G. Marrocco, “The art of UHF RFID antenna design: impedance-matching and size-reduction techniques,” *IEEE Antennas Propagat. Mag.*, vol. 50, no. 1, Jan. 2008.
- [25] —, “Gain-optimized self-resonant meander line antennas for RFID applications,” *IEEE Antennas and Wireless Propagation Letters*, vol. 2, pp. 302–305, Feb. 2003.
- [26] U. Mühlmann and H. Witschnig, ““hard to read tags”: an application specific experimental study in passive UHF RFID systems,” *Elektrotechnik & Informationstechnik*, vol. 124, no. 11, pp. 391–396, Nov. 2007.
- [27] R. Fletcher, U. P. Marti, and R. Redemski, “Study of UHF RFID signal propagation through complex media,” in *Proc. IEEE Antennas and Propagation Society International Symposium*, pp. 747–750 vol. 1B, Dec. 2005.
- [28] S. R. Aroor and D. D. Deavours, “Evaluation of the state of passive UHF RFID: An experimental approach,” *IEEE Systems Journal*, vol. 1, no. 2, pp. 168–176, Nov. 2007.
- [29] L. Sydänheimo, L. Ukkonen, and M. Kivikoski, “Effects of size and shape of metallic objects on performance of passive radio frequency identification,” *The International Journal of Advanced Manufacturing Technology*, vol. 30, no. 9-10, Oct. 2005.
- [30] J. D. Griffin, G. D. Durgin, A. Haldi, and B. Kippelen, “RF tag antenna performance on various materials using radio link budgets,” *Antennas and Wireless Propagation Letters, IEEE*, vol. 5, no. 1, pp. 247–250, Dec. 2006.
- [31] P. R. Foster and R. A. Burberry, “Antenna problems in RFID systems,” in *Proc. IEE Colloquium on RFID Technology*, pp. 3/1–3/5, 1999.

- 
- [32] S. Aroor and D. D. Deavours, "A dual-resonant microstrip-based UHF RFID cargo tag," in *IEEE MTT-S International Microwave Symposium Digest*, pp. 579 – 582, Jun. 2008.
- [33] H. W. Son, G. Y. Choi, and C. S. Pyo, "Design of wideband RFID tag antenna for metallic surfaces," *Electronics Letters*, vol. 42, no. 5, pp. 263–265, Mar. 2006.
- [34] H. W. Son, J. Yeo, G. Y. Choi, and C. S. Pyo, "A low-cost, wideband antenna for passive RFID tags mountable on metallic surfaces," in *Proc. IEEE Antennas and Propagation Society International Symposium*, pp. 1019 – 1022, Jul. 2006.
- [35] S. Ramo and J. R. Whinnery, *Fields and Waves in Modern Radio*, 2nd ed. John Wiley & Sons Inc., 1953.
- [36] S. Ramo, J. R. Whinnery, and T. van Duzer, *Fields and Waves in Communication Electronics*. John Wiley and Sons Inc., 1967.
- [37] R. C. Hansen, "Relationships between antennas as scatterers and as radiators," *Proceedings of the IEEE*, vol. 77, no. 5, pp. 659–662, May 1989.
- [38] W. Kahn and H. Kurss, "Minimum-scattering antennas," *IEEE Trans. Antennas Propagat.*, vol. 13, no. 5, pp. 671–675, Sep. 1965.
- [39] J. Aharoni, *Antennae - An Introduction to their Theory*. Oxford at the Clarendon Press, 1946.
- [40] R. W. P. King and C. W. Harrison Jr., "The receiving antenna," *Proc. IRE*, vol. 32, pp. 18–34, Jan. 1944.
- [41] A. F. Stevenson, "Relations between the transmitting and receiving properties of antennas," *Quart. Appl. Math.*, vol. 5, pp. 140–148, Jan. 1948.
- [42] R. E. Collin, "Limitations of the thevenin and norton equivalent circuits for a receiving antenna," *IEEE Antennas Propagat. Mag.*, vol. 45, no. 2, pp. 119–124, Apr. 2003.
- [43] J. B. Andersen and R. G. Vaughan, "Transmitting, receiving, and scattering properties of antennas," *IEEE Antennas Propagat. Mag.*, vol. 45, no. 4, pp. 93–89, Aug. 2003.
- [44] D. Pozar, "Scattered and absorbed powers in receiving antennas," *IEEE Antennas Propagat. Mag.*, vol. 46, no. 1, pp. 144 – 145, Feb. 2004.
- [45] A. W. Love, "Equivalent circuit for aperture antennas," *Electronics Letters*, vol. 23, pp. 708–710, Jun. 1987.
- [46] J. Van Bladel, "On the equivalent circuit of a receiving antenna," *IEEE Antennas Propagat. Mag.*, vol. 44, no. 1, pp. 164–165, Feb. 2002.
- [47] A. W. Love, "Comment on the equivalent circuit of a receiving antenna," *IEEE Antennas Propagat. Mag.*, vol. 44, no. 5, pp. 124–125, Oct. 2002.
- [48] —, "Correction - comment on the equivalent circuit of a receiving antenna," *IEEE Antennas Propagat. Mag.*, vol. 44, no. 6, p. 146, Dec. 2002.
- [49] W. Geyi, "Derivation of equivalent circuits for receiving antenna," *IEEE Trans. Antennas Propagat.*, vol. 52, no. 6, pp. 1620–1623, Jun. 2004.

- [50] B. Rembold, "Optimum modulation efficiency and sideband backscatter power response of RFID-tags," *Frequenz - Journal of RF-Engineering and Telecommunications*, vol. 63, no. 1-2, pp. 9–13, Jan. 2009.
- [51] P. V. Nikitin and K. V. S. Rao, "Performance limitations of passive UHF RFID systems," in *Proc. Antennas and Propagation Society International Symposium*, pp. 1011 – 1014, Jul. 2006.
- [52] A. Missoni, C. Klaf, and G. Holweg, "Dual frequency comprehensive transponder chip with inverse load modulation," in *Proc. The First International EURASIP Workshop on RFID Technology*, pp. 5–8, Sep. 2007.
- [53] V. I. Slyusar, "60 years of electrically small antennas theory," in *Proc. 6th International Conference on Antenna Theory and Techniques*, pp. 116–118, Sep. 2007.
- [54] S. R. Best, "A discussion on electrically small antennas surrounded by lossy dispersive materials," in *Proc. The First European Conference on Antennas and Propagation*, pp. 1–7, Nov. 2006.
- [55] ———, "A discussion on power factor, quality factor and efficiency of small antennas," in *Proc. IEEE Antennas and Propagation International Symposium*, pp. 2269–2272, Jun. 2007.
- [56] *Identification cards – Physical characteristics*, ISO/IEC 7810:2003.
- [57] *Information technology – Identification cards – Financial transaction cards*, ISO/IEC 7813:2006.
- [58] K. Li, C. H. Cheng, T. Matsui, and M. Izutsu, "Coplanar patch antennas: principle, simulation and experiment," in *Proc. Antennas and Propagation Society International Symposium*, pp. 402–405, Jul. 2001.
- [59] C. Decroze, G. Villemaud, F. Torres, B. Jecko, B. Zielinska, J. Grebmeier, G. Picard, and S. Petihomme, "Integrated coplanar antennas for short range link at 868 MHz," in *Proc. Antennas and Propagation Society International Symposium*, pp. 30–33, Jun. 2002.
- [60] Ansoft, a subsidiary of ANSYS Inc., "HFSS v11 3D Full-wave electromagnetic field simulation data sheet," 2009.
- [61] Nippon Steel Chemical Co.,Ltd, *Espanex MB18-25-18CE laminat specification sheet*, Electronic Materials R&D Lab., Sep. 2003.
- [62] Atmel Corporation, *ATA5590 Tag Antenna Matching - Application Note*, rev. 4843a-rfid-02/05 ed., Feb. 2005.
- [63] K. S. Leong, M. Leng, and P. H. Cole, "Dual-frequency antenna design for RFID application," in *Proc. International Technical Conference on Circuits/Systems, Computers and Communications*, Jul. 2006.
- [64] L. W. Mayer and A. L. Scholtz, "Gain and input impedance measurement for UHF transponder antennas," in *Proc. International Symposium on Antennas and Propagation*, Taipei, Taiwan, Oct. 2008. [Online]. Available: [http://publik.tuwien.ac.at/files/PubDat\\_167141.pdf](http://publik.tuwien.ac.at/files/PubDat_167141.pdf)
- [65] L. W. Mayer, "Dual-band antenna," U.S. patent E0196.0139, filed May 7th, 2007.
- [66] K. P. Ray and G. Kumar, "Tuneable and dual-band circular microstrip antenna with stubs," *IEEE Trans. Antennas Propagat.*, vol. 48, no. 7, pp. 1036–1039, Jul. 2000.

- [67] I. Chiba, K. Kihira, R. Yonezawa, and T. Numazaki, "Beam-space circular smart antenna fed by hybrid circuits," in *Proc. Antennas and Propagation Society International Symposium*, pp. 224–227, Jul. 2001.
- [68] X. M. Qing and Y. W. M. Chia, "Circularly polarised circular ring slot antenna fed by stripline hybrid coupler," *Electronic Letters*, vol. 35, no. 25, pp. 2154–2155, Dec. 1999.
- [69] R. Greeff, D. K. Ovard, and D. Khatri, "Right hand and left hand circular polarized RFID backscatter antenna," US 6,255,993, Jul. 3rd, 2001.
- [70] H.-T. Chen, T.-W. Chiou, and K.-L. Wong, "Broadband dual-polarized patch antennas with hybrid feeds for 1800 MHz band operation," in *Proc. Antennas and Propagation Society International Symposium*, pp. 102–105, Jul. 2001.
- [71] R. Langwieser, G. Lasser, C. Angerer, M. Rupp, and A. L. Scholtz, "A modular UHF reader frontend for a flexible RFID testbed," in *Proc. The Second International EURASIP Workshop on RFID Technology*, Jul. 2008.
- [72] I. Tareef Al-Mahdawi, "Adaptive coherent RFID reader carrier cancellation," WO 2006/088583 A2, published Aug. 24th, 2006.
- [73] E. A. Fardin, A. S. Holland, and K. Ghorbani, "Electronically tunable lumped element 90° hybrid coupler," *Electronics Letters*, vol. 42, no. 6, pp. 353–355, Mar. 2006.
- [74] F. Ferrero, C. Luxey, G. Jacquemod, R. Staraj, and V. Fusco, "A reconfigurable hybrid coupler circuit for agile polarisation antenna," in *Proc. The First European Conference on Antennas and Propagation*, Nov. 2006.
- [75] S. V. Parekh, "Simple formulae for circular-polarization axial-ratio calculations," *IEEE Antennas Propagat. Mag.*, vol. 33, pp. 30–32, Feb. 1991.
- [76] K. Hirasawa and M. Haneishi, *Analysis, design, and measurement of small and low-profile antennas*. 685 Canton Street Norwood, MA 02062: Artech House, Inc., 1992.
- [77] A. K. Skrivervik and J.-F. Zürcher, "Recent advances in PCS antenna design and measurement," *AUTOMATIKA - Journal for Control, Measurement, Electronics, Computing and Communications*, vol. 43, no. 1–2, Oct. 2002.
- [78] L. W. Mayer and A. L. Scholtz, "Efficiency measurement method for UHF transponder antennas," in *Proc. The First International EURASIP Workshop on RFID Technology*, pp. 17–20, Vienna, Austria, Sep. 2007. [Online]. Available: [http://publik.tuwien.ac.at/files/pub-et\\_12659.pdf](http://publik.tuwien.ac.at/files/pub-et_12659.pdf)
- [79] S. A. K. and J.-F. Zürcher, "PCS antenna measurement," in *Proc. Antennas and Propagation Society International Symposium*, vol. 3, pp. 702–705, Jun. 2002.
- [80] T. Fukasawa, K. Shimomura, and M. Ohtsuka, "Accurate measurement method using fiber-optics for an antenna on a portable telephone," *IEEE Topical Conference on Wireless Communication Technology*, pp. 138–139, Oct. 2003.
- [81] L. Mats, J. T. Cain, and M. H. Mickle, "The in-situ technique for measuring input impedance and connection effects of RFID tag," *IEEE Trans. Autom. Sci. Eng.*, 2006, to be published.
- [82] M. Camp, R. Herschmann, T. Zelder, and H. Eul, "Determination of the input impedance of RFID transponder antennas with novel measurement procedure using a modified on-wafer-prober," *Advances in Radio Science*, vol. 5, pp. 115–118, 2007.

## Bibliography

---

- [83] P. Kabacik, A. Byndas, R. Hossa, and M. Bialkowski, "A measurement system for determining radiation efficiency of a small antenna," in *Proc. The First European Conference on Antennas and Propagation*. European Space Agency, Nov. 2006.
- [84] D. J. Gray, "3D antenna measurement system - low gain antenna measurements and CTIA OTA testing," in *Proc. The First European Conference on Antennas and Propagation*. European Space Agency, Nov. 2006.
- [85] H. Arai, *Measurement of Mobile Antenna Systems*. 685 Canton Street, Norwood, MA 02062: Artech House, Inc., 2001.
- [86] Melexis Microelectronic Inegrated Systems, "TH72031 868/915 MHz FSK transmitter data sheet," Jun. 2007.
- [87] Agilent Technologies, Inc., "Designing and calibrating RF fixtures for surface-mount devices," *Device Test Seminar*, 1996.
- [88] U. Pisani, A. Ferrero, and G. L. Madonna, "Experimental characterization of nonlinear active microwave devices," *Review Of Radio Science*, pp. 3-22, 2001.
- [89] Agilent Technologies, Inc., "In-fixture measurements using vector network analyzers," 1999, application note AN 1287-9.
- [90] K. H. Wong, "Characterization of calibration standards by physical measurements," *ARFTG Conference Digest-Spring, 39th*, vol. 21, pp. 53-62, Jun. 1992.